Chemical Science

ROYAL SOCIETY OF CHEMISTRY

REVIEW

View Article Online
View Journal | View Issue

Cite this: *Chem. Sci.*, 2024, **15**, 7870

Advances and challenges in the electrochemical reduction of carbon dioxide

Jingyi Han, Xue Bai, Xiaoqin Xu, Xue Bai, Anaer Husile, Siying Zhang, Luoluo Qi and Jingqi Guan *

The electrocatalytic carbon dioxide reduction reaction (ECO_2RR) is a promising way to realize the transformation of waste into valuable material, which can not only meet the environmental goal of reducing carbon emissions, but also obtain clean energy and valuable industrial products simultaneously. Herein, we first introduce the complex CO_2RR mechanisms based on the number of carbons in the product. Since the coupling of C–C bonds is unanimously recognized as the key mechanism step in the ECO_2RR for the generation of high-value products, the structural–activity relationship of electrocatalysts is systematically reviewed. Next, we comprehensively classify the latest developments, both experimental and theoretical, in different categories of cutting-edge electrocatalysts and provide theoretical insights on various aspects. Finally, challenges are discussed from the perspectives of both materials and devices to inspire researchers to promote the industrial application of the ECO_2RR at the earliest.

Received 22nd March 2024
Accepted 30th April 2024

DOI: 10.1039/d4sc01931h

rsc.li/chemical-science

1. Introduction

In the late 2023, the 28th United Nations Climate Change Conference (COP28) conducted the first "global carbon inventory" of the world's efforts to address climate change.[1] The parties unanimously decided to accelerate the pace of reducing greenhouse gas emissions by 2030,[2] calling on governments to advance the effective implementation of carbon reduction actions to achieve the ultimate goal of the Paris Agreement as soon as possible,[3] *i.e.*, in addition to natural autonomous pathways such as bioenergy with carbon capture and storage (BECCS), industrial technologies of carbon capture, utilization and storage (CCUS) are to be eagerly promoted alternatively.[4] With the depletion of traditional fossil fuels, the energy crisis has become an extreme urgency.[5]

As an ideal solution, the electrocatalytic carbon dioxide reduction reaction (ECO_2RR) can not only end the artificial carbon cycle, but also convert renewable power such as solar energy and wind energy into beneficial chemical energy products, including clean fuels and industrial raw materials to achieve a virtuous cycle of turning waste into treasure as a whole.[6–9] However, as depicted in Fig. 1, to date, the related research in the field of ECO_2RRs is still in the emerging stage, which is far from mature compared with other electrochemical technologies such as hydrogen production through the electrolysis of water, and the prerequisite for its practical application is a robust catalyst with high electrochemical activity and high selectivity toward the target product.[10–13] Noteworthily, the complexity of the reaction mechanism of the CO_2RR should not be underestimated, and a large number of studies have confirmed that the C–C coupling step is crucial for the advancement of the ECO_2RR and has a high degree of structural sensitivity.[14–17] Therefore, the in-depth exploration of the influence of the electronic structure of materials on the ECO_2RR catalytic performance has always been the main direction of researchers.

In this review, the reaction mechanisms of the ECO_2RR are first classified based on the number of carbon atoms in the products. On this basis, we thoroughly discuss the profound insights gained on the structure–activity relationship, and the most cutting-edge catalysts reported in recent years have been comprehensively reviewed according to the detailed categories, including atomically-dispersed catalysts, alloys, metal–organic frameworks (MOFs) and covalent organic frameworks (COFs). In terms of theoretical calculations, authoritative opinions are representatively classified. Finally, we analyze the remaining challenges from both the material and device perspectives, with a view to inspire researchers to help pave a new stage in the field of ECO_2RR.

2. ECO_2RR mechanisms

In the process of carbon dioxide reduction, due to the extremely high stability of C=O chemical bonds and the competition of hydrogen evolution reaction (HER), the carbon dioxide reduction process faces major challenges, which seriously hinders the effective implementation.[18–20] Therefore, it is urgent to design

Institute of Physical Chemistry, College of Chemistry, Jilin University, Changchun 130021, PR China. E-mail: guanjq@jlu.edu.cn

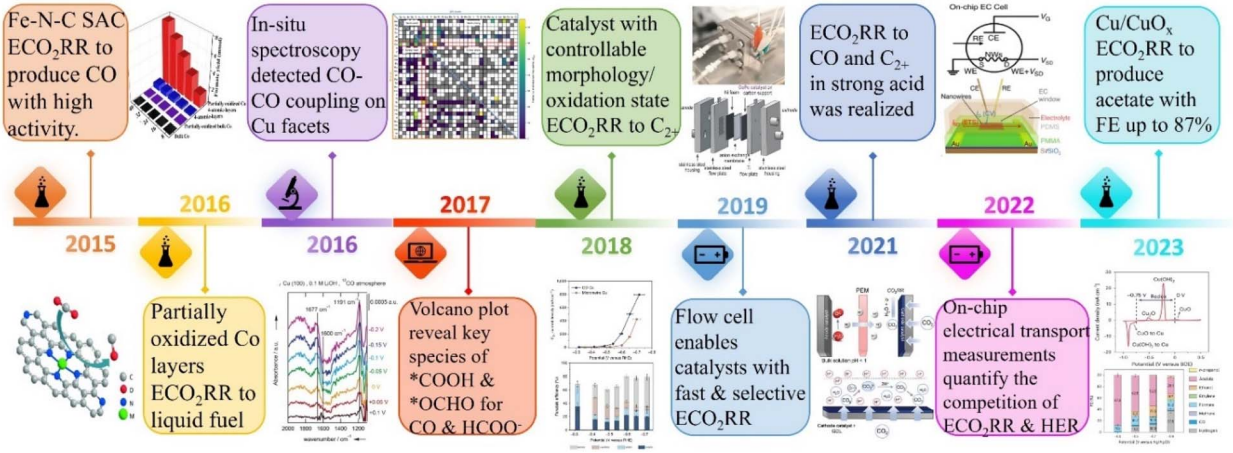

Fig. 1 Timeline of the major developments in the ECO_2RR.

an efficient catalyst to overcome the high activation energy barrier. However, although there are more and more experimental and theoretical studies on various catalysts, the available catalysts need to have a large overpotential for specific products, and their selectivity is usually very low. On different catalysts under different conditions, different products will be produced, such as CO, formate, methane and ethanol.[21] In addition, the electrochemical CO_2RR process involves multi-electron transfer processes, and the product is very complex, making the subsequent product separation and purification processes very difficult. Therefore, it is important to understand the reaction mechanism and reaction intermediates, which is related to the design and modification of catalysts.[22] Table 1 lists the half-reactions that may occur on the cathode surface during the electrochemical reduction of CO_2 and their equilibrium potentials relative to the standard hydrogen electrode (SHE) in electrolytes at pH 7.[19]

Theoretical calculations and modeling can provide information such as binding energy, free energy and activation energy of the intermediates, which is helpful to evaluate the feasibility of each reaction step of the synthesized catalyst and screen out the key intermediates conducive to the reaction.[23]

Table 1 The possible half-reactions on the surface of the cathode during the electrochemical reduction of CO_2 and their equilibrium potential relative to SHE in the electrolyte at pH 7

CO_2 reduction half reaction	The equilibrium potential relative to SHE at pH 7
$CO_2 + 2H^+ + 2e^- \rightarrow HCOOH + H_2O$	$E^0_{redox} = -0.610$ V
$CO_2 + 2H^+ + 2e^- \rightarrow CO + H_2O$	$E^0_{redox} = -0.530$ V
$2CO_2 + 2H^+ + 2e^- \rightarrow H_2C_2O_4$	$E^0_{redox} = -0.913$ V
$CO_2 + 4H^+ + 4e^- \rightarrow HCHO + H_2O$	$E^0_{redox} = -0.480$ V
$CO_2 + 6H^+ + 6e^- \rightarrow CH_3OH + H_2O$	$E^0_{redox} = -0.380$ V
$CO_2 + 8H^+ + 8e^- \rightarrow CH_4 + 2H_2O$	$E^0_{redox} = -0.240$ V
$2CO_2 + 12H^+ + 12e^- \rightarrow C_2H_4 + 4H_2O$	$E^0_{redox} = -0.349$ V
$2CO_2 + 12H^+ + 12e^- \rightarrow C_2H_5OH + 3H_2O$	$E^0_{redox} = -0.329$ V
$2CO_2 + 14H^+ + 14e^- \rightarrow C_2H_6 + 4H_2O$	$E^0_{redox} = -0.270$ V
$3CO_2 + 18H^+ + 18e^- \rightarrow C_3H_7OH + H_2O$	$E^0_{redox} = -0.310$ V
$2H^+ + 2e^- \rightarrow H_2$	$E^0_{redox} = -0.42$ V

Electrochemical reduction method is one of the key means to determine the reaction intermediates. Pure metals such as Al, Fe, Ni, Pt and Ti can reduce CO_2 to CO, but the HER rate during the reduction process is much higher than the reduction rate of CO_2, while Ag, Au and Zn will produce CO with high current efficiency.[24] Formate is the main product of the catalytic reduction on metals such as Hg, In and Sn.[25] Cu-based catalysts can reduce CO_2 to hydrocarbons and alcohols. Fig. 2 shows the mechanism of CO_2RR on metal electrocatalysts.[26] This section introduces the main mechanisms of electroreduction of CO_2 to $HCOOH/HCOO^-$, CO, HCHO, CH_3OH, CH_4, C_2H_4, CH_3CH_2OH and $CH_3CH_2CH_2OH$.

2.1. Reduction of CO_2 to C_1 products

The products of CO_2 reduction to C_1 include $HCOOH/HCOO^-$, CO, HCHO, CH_3OH and CH_4.[27–31] The formation of $HCOOH/HCOO^-$ can be divided into three steps. First, CO_2 molecules are inserted into the metal–hydrogen bond and then combined with one or two oxygen atoms to the metal electrode, followed by further protonation to form formate (Fig. 3a).[32] Second, the surface hydroxyl group reacts with CO_2 to form a carbonate intermediate, thereby forming $HCOO^-$ (Fig. 3b).[33] Finally, $*CO_2^-$ radicals react with adjacent water molecules to form formate/formate salts (Fig. 3c).[34] The reduction of CO_2 to CO is carried out by forming *COOH intermediates. The *COOH intermediate is formed by the proton coupling of $*COO^-$, electron transfer or single electron transfer, and then protonation. Further, proton-coupled electrons are transferred to the adsorbed *COOH intermediate, resulting in dissociation to form CO (Fig. 3d). Hansen *et al.* found that *COOH was reduced to *CO, but it was inhibited by the first step of weak COOH binding.[35] The formation of HCHO, CH_3OH and CH_4 is carried out by the transfer of 4, 6 and 8 electrons, respectively. The initial *CO is converted to *CHO, $*CH_2O$ and $*CH_3O$ by hydrogenation, and $*CH_3O$ is further hydride oxygenated to CH_4,[36] which can also be produced by the multi-step hydrogenation of *COH. $*CH_2O$ is desorbed to form HCHO, and $*CH_3O$ is hydrogenated to CH_3OH (Fig. 3e).[37]

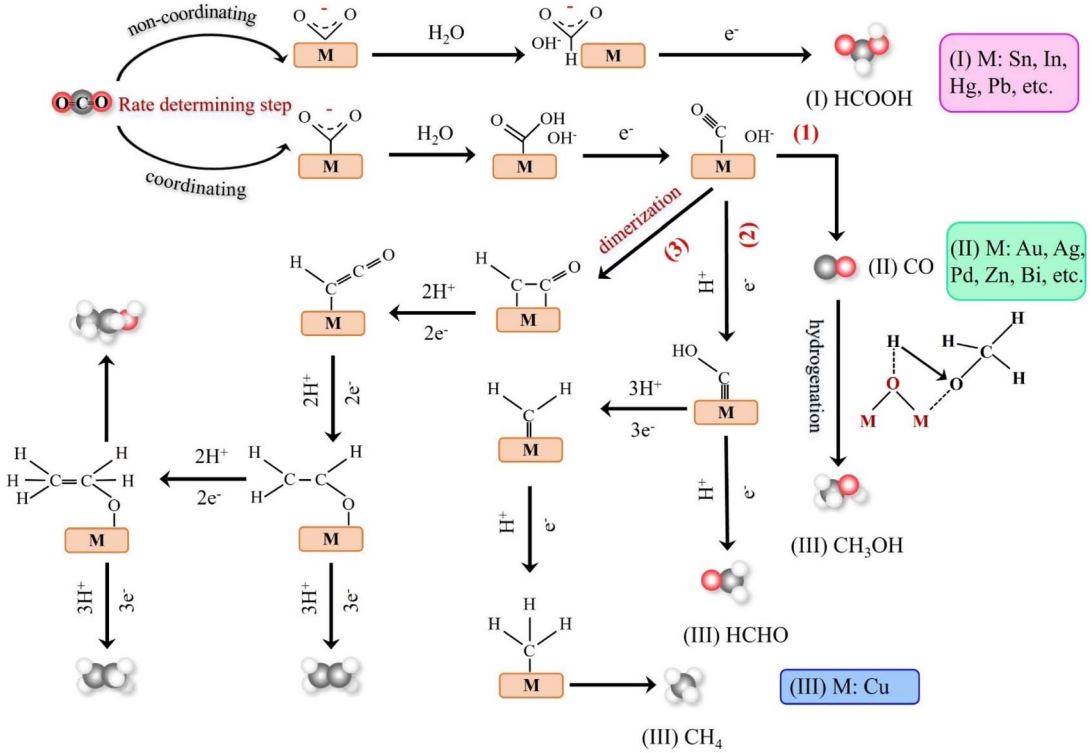

Fig. 2 Schematic mechanism of various metal electrocatalysts for the CO_2RR.

2.2. Reduction of CO_2 to C_2 products

C_2 products mainly include C_2H_4, CH_3CHO and CH_3CH_2OH.[38–40] At low negative potentials, the formation of C_2 products is a complex process with multiple reaction pathways. Nie *et al.* proposed that the formation of C_2H_4 is the result of the coupling of two $*CH_2$ intermediates or the insertion of CO in the Fischer–Tropsch-like step.[41] Another pathway is that the *CO intermediate is dimerized to form the $*C_2O_2$ intermediate, which is then transformed into *COCHO by electron transfer and finally hydride oxygenated to form C_2H_4.[42] The formation of CH_3CH_2OH has the same reaction intermediate as C_2H_4. Researchers proposed that *CHO dimerization is the main pathway of ethanol on Cu (100) at low potentials.[43] The intermediate of vinyl alcohol can be further reduced to C_2H_4 or CH_3CHO and C_2H_5OH (Fig. 4).

2.3. Reduction of CO_2 to C_3 products

The reduction of CO_2 to C_3 long-chain products (such as propanol) has always been a difficult problem to overcome.[44] When CO_2 is reduced to propanol, the following steps may be carried out. The adsorbed C_2 intermediate undergoes a C–C coupling reaction with adjacent C_1 intermediate, followed by proton or electron transfer to produce propionaldehyde, which is finally reduced to propanol (Fig. 5).[45] Although C_{2+} products are eagerly awaited due to their peak economic value, the generation of C_{2+} by ECO_2RR remains challenging at this stage. Table 2 lists the formation rates and FEs obtained so far for different C_{2+} products to provide a more comprehensive overview.

3. Structure–activity relationships

The electronic structure of the catalyst is key to optimizing the catalytic processes that fundamentally dominate their various electrocatalytic properties, including activity, selectivity, and stability.[62–65] Therefore, the structure–performance relationship of the catalyst as the core of electrocatalysis is of great significance. However, the factors affecting the electronic state of the catalytic center are complicated. The combination of active metal elements, defect site engineering and coordination environment optimization between adjacent atoms have been developed as the main means to effectively regulate the electronic structure.[66–68] The in-depth understanding about the structure–performance relationship not only broadens the way for the rational development of new catalytic materials with more potential and pertinence but also provides a strong theoretical guidance for revealing the mechanism of electrocatalytic reactions. Furthermore, theoretical modulation of electrocatalysts can effectively adjust the local hindrance and electronic structure to manipulate the entire workflow of carbon dioxide in the electroreduction process, including local migration, adsorption, activation, hydrogenation, and desorption of the products, thus providing great possibilities and versatility for the realization of carbon dioxide electroreduction. Therefore, reasonable theoretical modulation strategy is the key to improve the catalyst performance. Electrocatalytic reactions generally occur at the interface or surface of the catalyst, and differences in the catalyst structure can affect the strength between the catalyst surface and the adsorbate. At the same

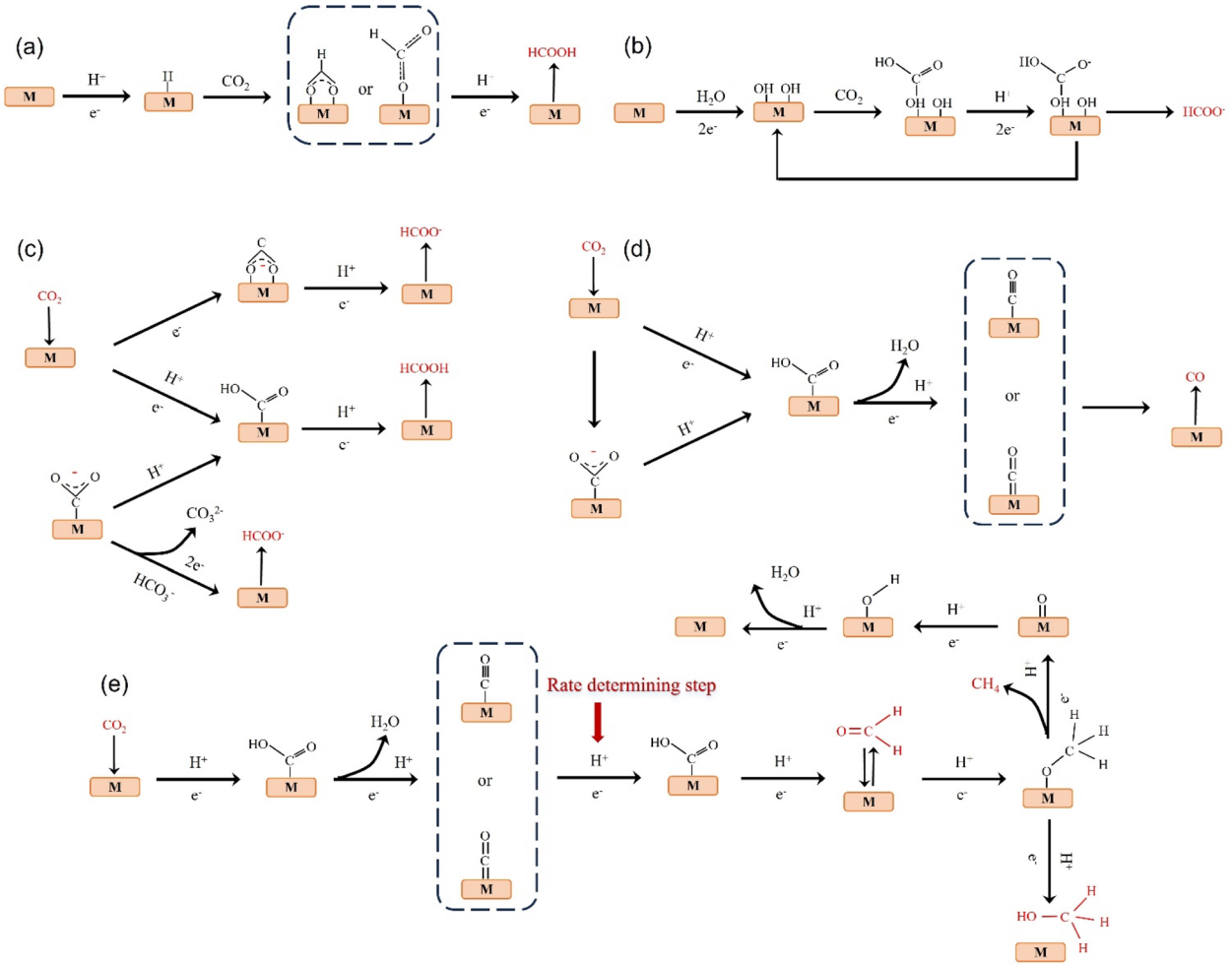

Fig. 3 (a) Monodentate or bidentate intermediate route for HCOOH formation. (b) Surface-bound carbonate intermediate route for the formation of HCOOH/formate. (c) $*CO_2^-$ radical intermediate route for the formation of formate. (d) Possible reaction pathway of CO_2 reduction to CO. (e) Possible reaction pathways for the reduction of CO_2 to HCHO, CH_3OH and CH_4.

time, the catalyst geometry or electronic structure engineering all produce synergistic effects, influencing the catalytic activity, stability, and selectivity. In addition, changes in the electronic structure of catalysts can directly affect the spin change and change the way catalysts bind to the adsorbent, leading to a decrease in the reaction energy and ultimately an increase in the catalytic activity.[69–72] Therefore, we also combine theoretical modulation to conduct a more profound and comprehensive analysis of the structure activity relationship of ECO_2RR catalysts.

3.1. Metal centers

Metal sites play an important role as the main foundation for adsorbing CO_2 and activating it into different products.[73–76] Since various metal elements have their distinct state of electron clouds in different shell orbitals, they congenitally have significant differences in the CO_2RR electrocatalytic activity, including current density, stability, and even the types and selectivity of generated products. To date, researchers have researched single-atom catalysts (SACs) covering most of the transition metal elements like Mo, Fe, Co, Ni, Cu, and Zn, precious metal elements like Au, Ag, Pt, and Ir, and p-block elements like Bi, Sn, and Sb to explore their intrinsic CO_2RR electrocatalytic properties (Fig. 6).[77] As far as single metal elements are concerned, it commonly possesses the ability to convert CO_2 into CO (g), especially transition metals. Notably, certain metals can reduce CO_2 to produce different products simultaneously.[78] For example, in addition to CO, Co-SACs and Sn-SACs can yield second liquid product CH_3OH and HCOOH, respectively.[79] However, the determinants of product selectivity remain unclear. The well-designed Zn-N_4-C structure can generate CH_4 with high economic value.[80] This Zn SAC exhibited remarkable CO_2RR activity with high faradaic efficiency of 85% toward CH_4 and can maintain this level up to 35 hours. Density functional theory (DFT) calculations revealed that the Zn site follows a unique CO_2RR mechanism, where the initial activation of CO_2 is more inclined to the O-binding intermediate *OCHO rather than the C-binding intermediate *COOH, which is conducive to the hydrogenation of CO_2 to CH_4. It has been reported that Co, Cu, Mo, In, Sn and Sb can rarely reduce

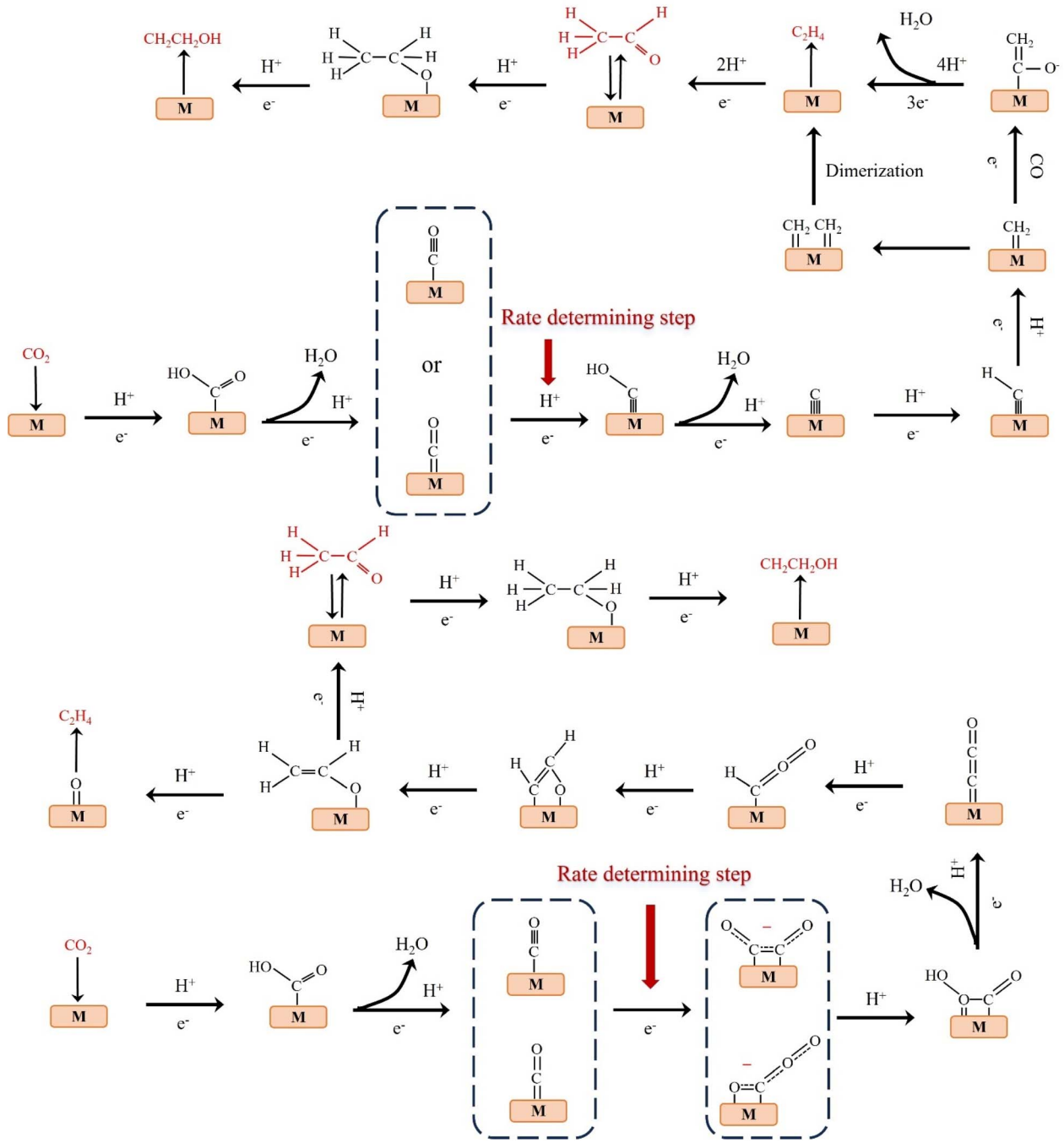

Fig. 4 Possible reaction paths for electrocatalytic CO_2 reduction to produce C_2H_4, CH_3CHO, and C_2H_5OH.

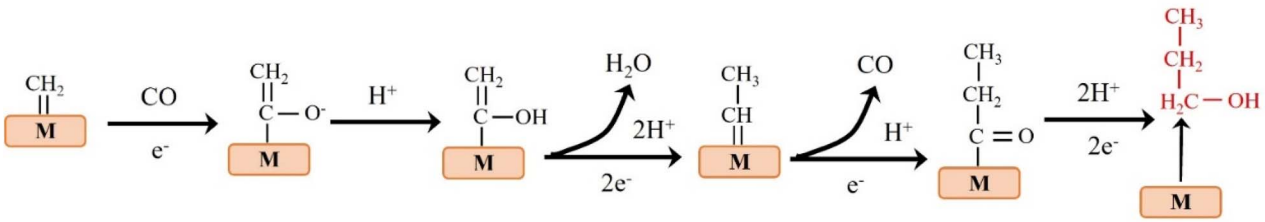

Fig. 5 Possible reaction pathway for electrocatalytic CO_2 reduction to C_3H_7OH.

Table 2 Summary of advanced catalysts for ECO_2R to C_{2+} products

Catalyst	FE of C_{2+} products (%)	Formation rate of C_{2+} $r_{C_{2+}}$ (mmol cm^{-2} h^{-1})	Geometric area normalized $j_{C_{2+}}$ (mA cm^{-2})	Electrolyte	Ref.
Cu/Pd-1%	66.2	1.45	463.2	1 M KOH	46
CuO NS	85.6	0.74	237	1 M KOH	47
CuAg-wire-6%	85.1	0.8	264.5	1 M KOH	48
dCu_2O/Ag2.3%	82.1	2.06	656.8	1 M KOH	49
$Li_{2-x}CuO_2$	90.6	0.65	200	1 M KOH	50
Cu_3N_x	81.7	0.99	307	1 M KOH	51
$Cu(OH)_2$-D	86.8	0.65	217	1 M KOH	52
Cu–CuI	71	1.13	381	1 M KOH	53
Nanoporous Cu	62	1.25	411	1 M KOH	54
CuPb-0.7/C	73.6	1.01	294.4	1 M KOH	55
CuO NS	58.6	1.32	410.2	1 M $KHCO_3$	56
Ag–Cu/GDY	55.1	—	24.98	1 M $KHCO_3$	57
N-doped graphene quantum dots	47.75	—	~90	1 M KOH	58
N-functionalized GO	45.3	—	~1.3	0.1 M $KHCO_3$	59
N-functionalized GO	45	—	~50	1 M KOH	60
SnO_2 nanoparticles	10.4	—	150	1 M $KHCO_3$	61

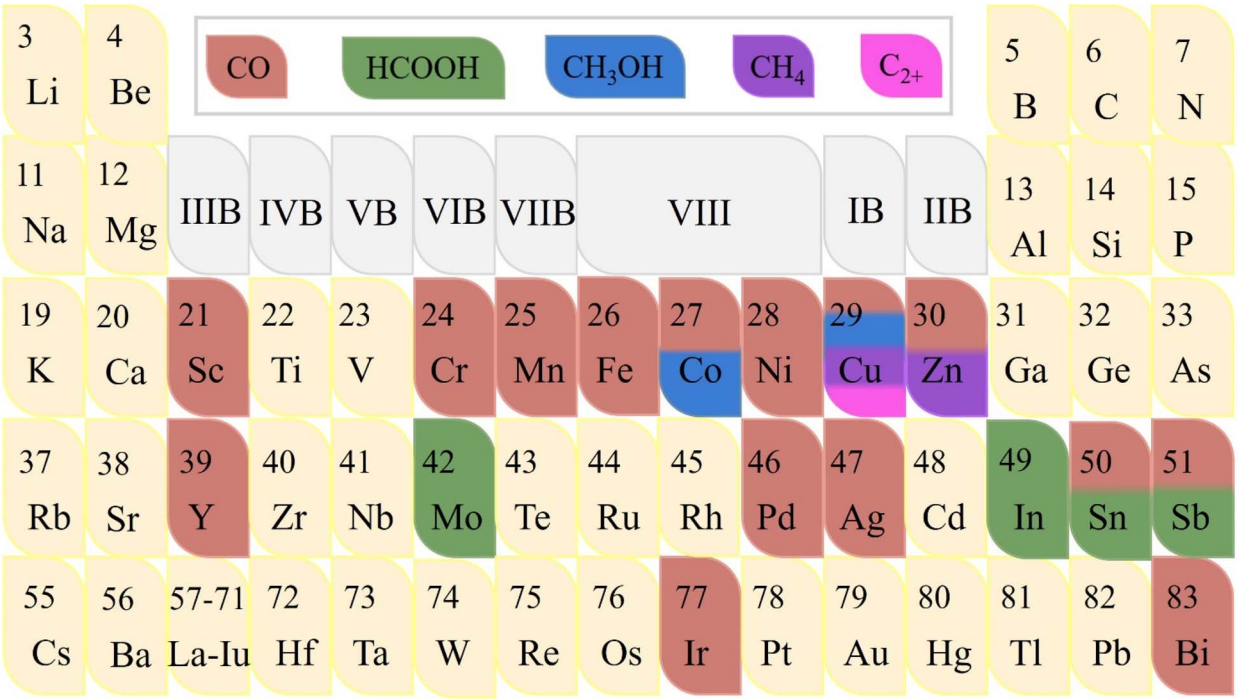

Fig. 6 The known product distribution of the reported elements for the ECO_2RR.

CO_2 to liquid C1 products including HCOOH and CH_3OH.[81] For example, atomically-dispersed Bi sites follow another reaction mechanism in which the energy barrier advantage of forming *COOH intermediate is obvious, making the Bi center have higher activity and selectivity for converting CO_2 into HCOOH.[82] Another element used to produce HCOOH is In, which also follows a similar reaction pathway.[83] Interestingly, for the N-C structure, high concentrations of In atoms have been verified to be more inclined to generate HCOOH, while highly dispersed In sites have the ability to accelerate the formation of CO. Unlike In, the selectivity of HCOOH at atomic Sb sites differs slightly from that of pure metal, while the activity advantage of the former is significant.[84] Theoretical calculations revealed that the intermediate species formed on the Sb-N_4 structure favors forming HCOO* rather than COOH*, thus providing a pathway to generate formate with $FE_{formate}$ up to 94% at −0.8 V *vs.* RHE. In particular, due to the dense electron distribution with rich energy of the d and f orbitals in the inner layer, Cu has a strong effect of localization and exchange interaction, thus exhibiting remarkable ability of reducing CO_2 to C_2, C_3 and even more carbon products.[85] Interestingly, the type and yield of products on the same metal-based material are closely related

to the morphology. For instance, Irabien *et al.* systematically focused on the effect of particle size in the range of 25–80 nm on the conversion efficiency and selectivity of continuous ECO_2RR on Cu-based nanoparticles.[20] They found that when the particle size was reduced to 25 nm, the ethylene yield and Faraday efficiency with high economic value reached the peak, which were 1148 μmol m^{-2} s^{-1} and 92.8%, respectively. Simultaneously, the competitive HER was weakened, which strongly verified the inextricable relationship between the material morphology like particle size and the electrocatalytic activity of ECO_2RR.

Building on single metal sites, introducing additional metal sites to construct heteronuclear active centers can combine the property advantages of various metals.[86] Multinuclear electrocatalysts have a variety of active centers including top and bridging sites, thus providing more diversified adsorption modes for CO_2 and intermediates.[87] Moreover, the coordination between various metal atoms and adjacent ligands is rather flexible, and the d-band center can be regulated through the interaction of electron orbitals, thereby optimizing the adsorption energy of the intermediate species so that it possesses properties particular for SACs to effectively break their inevitable linear scale barrier.[88] The asymmetric multinuclear active centers not only have a significantly enhanced charge density gradient but also locally generate torque, which is conducive to the efficient overlap of atomic orbitals when activating active linear molecules, resulting in the leap of the overall electrocatalytic CO_2RR performance and showing more potential for practical applications. For example, due to the superior intrinsic activity of Ni and Fe at high and low potentials, respectively, Ren *et al.* designed a Ni/Fe-N-C bimetallic material, which can maintain a high selectivity of CO at a wide potential span from − 0.4 V to −1 V, and a high FE_{CO} of 98% can be obtained at −0.7 V.[89] Gong *et al.* screened Zn and Co elements,[90] in which the Co site is beneficial for the formation of *COOH, while the Zn site is beneficial for the desorption of *COOH. The bimetallic site of Zn/Co-N-C can simultaneously reduce the energy barrier of both the processes to greatly promote the conversion of CO_2 to CO.

3.2. Vacancy defects

Vacancies not only have unique electronic properties but also generate a fresh coordination structure to cooperatively optimize the electronic and band structure of the active center to upgrade the chemical properties.[91] Furthermore, vacancy defects provide additional adsorption and active sites for reactive species and moderate the free energy of CO_2 activation and product desorption. Additionally, the defect sites play a crucial role in the electrochemical performance and stability. Due to their high controllable preparation characteristics, vacancy defect engineering is widely used in geometric/electronic structure modulation. In general, vacancies applied in CO_2RR can be classified into cationic and anionic vacancies.[92] Due to the relatively low energy required to generate anionic vacancies such as O, S, and N, they have been extensively explored combined with theoretical calculations.[93–95] For example, a Cu–Sn diatom-site electrocatalyst stabilized by double oxygen vacancies on CeO_{2-x} was constructed by Chen *et al.* Theoretical calculations emphasized the importance of the synergistic effect of copper and tin in lowering the activation energy and promoting the formation of the intermediate $^*OCHO$, thus explaining its high formate selectivity (Fig. 7a and b).[96] Besides, a sacrificial protection strategy to stabilize the interfacial crystalline CuO by embedding active amorphous SnO_2 (c-CuO/a-SnO_2) was reported by Guo *et al.* DFT calculations demonstrated that the loss of oxygen in the heterostructure mainly originates from amorphous SnO_2, avoiding the reduction of c-CuO. Meanwhile, the production of O_v in c-SnO_2 leads to off-domain s-orbital electrons around the tin atom, which provides additional electrons in higher orbitals than the unoccupied d-orbitals of Cu_{2+} (Fig. 7c and d). Therefore, a-SnO_2 can effectively retain Cu_{2+} as a reservoir for oxygen species, thus avoiding oxygen loss from c-CuO, greatly improving the electrocatalytic activity, selectivity, and stability.[97]

The cation vacancies of various metal atoms that act as shallow transport acceptors outperform in catalytic processes, which can effectively tune the band structure, thus giving them unexpected properties without creating new intermediate species.[98] For instance, Lu *et al.* synthesized Ni-N_3-V single-atom catalysts with vacancy defects at the Ni site. DFT calculations showed that the presence of vacancy defects in Ni-N_3-V SACs could significantly improve their electrocatalytic activity for CO_2 reduction (Fig. 7e and f).[99] Besides, Xie *et al.* synthesized dynamically reconstructed tri-copper vacancy aggregates confined in copper nanowires. Theoretical calculations showed that triple copper vacancies lead to charge transfer from the surroundings to locations near the vacancies, increasing their local charge density. The charge density difference between the two $^*CO$ on the triple-copper vacancy copper sheet and the pristine copper sheet shows that the different charge distributions of different copper atoms near the defect clusters lead to different charge distributions of the bonded neighboring $^*CO$, which alleviate the electrostatic repulsion and promote the C–C coupling (Fig. 7g). As a result, the triple copper vacancy binding enriches and redistributes the local negative charge, enhances the adsorption of $^*CO$ intermediates, and lowers the energy barrier for CO–CO coupling, thereby increasing the C_{2+} yield.[100] Furthermore, Hu *et al.* designed a Se vacancy-containing bimetallic electrocatalyst denoted as $CuInSe_2$. The Se vacancies facilitate electron delocalization, promote electron redistribution, slightly adjust the energy band structure, and optimize the CO_2RR pathway of the bimetallic selenium compound. As a result, the Se-deficient $CuInSe_2$ possessed a highly selective CO generation ability in aqueous solution, and the V-$CuInSe_2$ cathode exhibited satisfactory performance in zinc–CO_2 batteries in water. The CO Faraday efficiency was as high as 91%. In addition, water-based zinc–CO_2 cells based on V-$CuInSe_2$ cathodes reached a discharge voltage of ≈0.55 V and had a good lifetime.[62] Although many achievements have been made at the theoretical level, the studies on cation vacancy defects are still limited and need to be further enriched.[101]

3.2.1. Anionic vacancies. Among various types of vacancies, oxygen vacancy (V_O) is the most prevalent due to its low

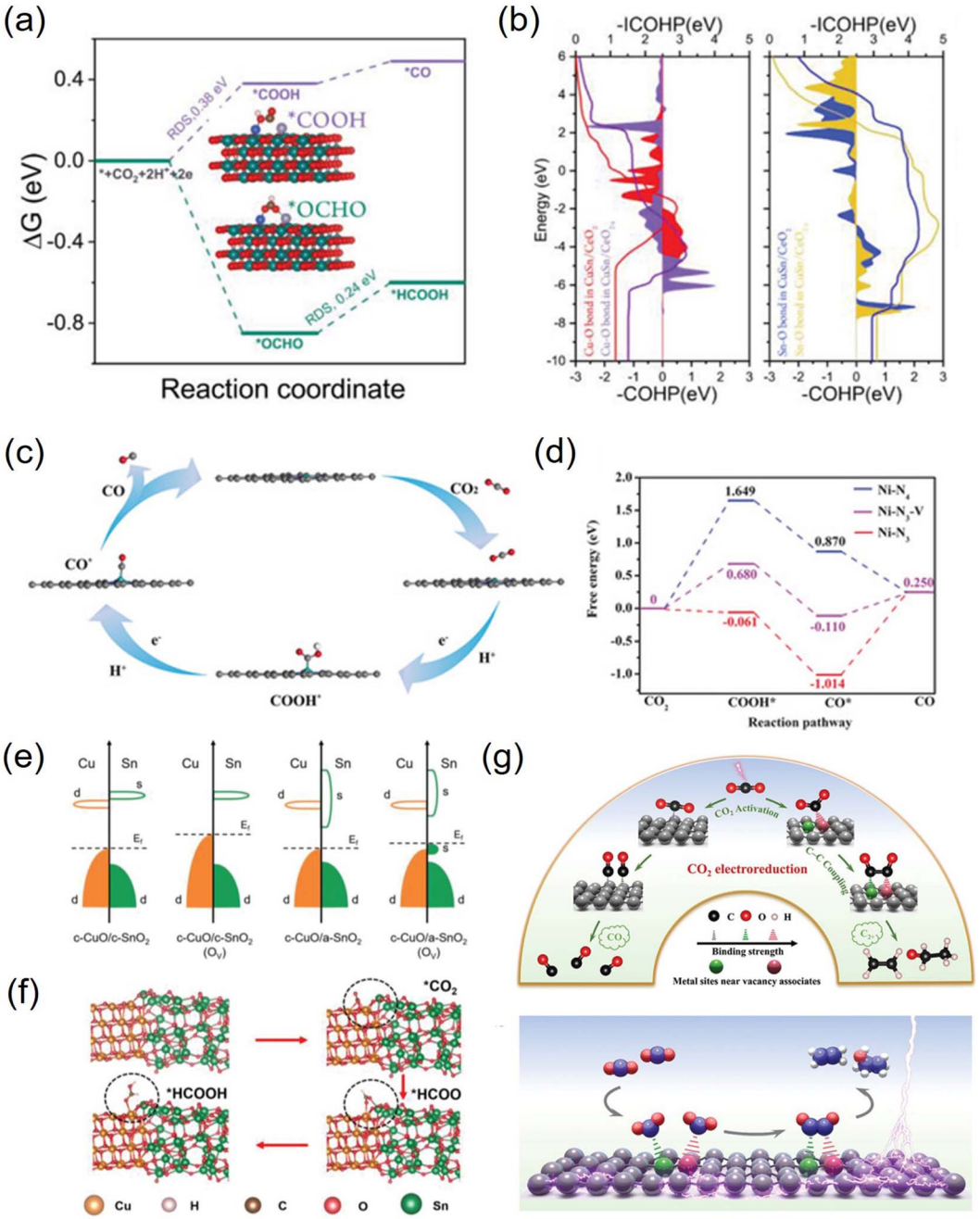

Fig. 7 (a) Free energy profiles of the CO_2RR on CuSn/CeO_{2-x}. (b) The COHP and ICOHP of Cu–O and Sn–O bonds in CuSn/CeO_2 and CuSn/CeO_{2-x}. (c) Band structures before and after the formation of O_v for c-CuO/c-SnO_2 and c-CuO/a-SnO_2. (d) The typical adsorption process of formate on c-CuO/a-SnO_2. (e) The proposed reaction paths of Ni-N_3-V for CO_2 electroreduction to CO. (f) Calculated free-energy diagram for the conversion of CO_2 to CO. (g) Facilitating CO_2 electroreduction to C_{2+} production through reconstructed Cu vacancy associates. (a and b) Reproduced with permission.[96] Copyright 2023, Wiley-VCH Verlag. (c and d) Reproduced with permission.[97] Copyright 2023, Wiley-Blackwell. (e and f) Reproduced with permission.[99] Copyright 2019, John Wiley and Sons Ltd. (g) Reproduced with permission.[100] Copyright 2024, Wiley-Blackwell.

formation energy barrier.[102] Since the O atoms of CO_2 can populate the V_O, efficient trapping of CO_2 molecules can be achieved. Through the chemisorption, the C=O bond is stretched to activate the CO_2 molecule, and the energy barrier of the intermediate species is stabilized to a low value.[103] For example, Gao *et al.* prepared an atomic-layered CO_3O_4 material and deliberately created oxygen vacancies on the surface to conduct targeted investigation on its role, revealing that the V_O-rich material surpasses the contrast sample without V_O in all the catalytic properties (Fig. 8a–e).[104] The current density of the former is double that of the latter; the FE_{HCOOH} is drastically increased from 67.3% to 87.6%, and it

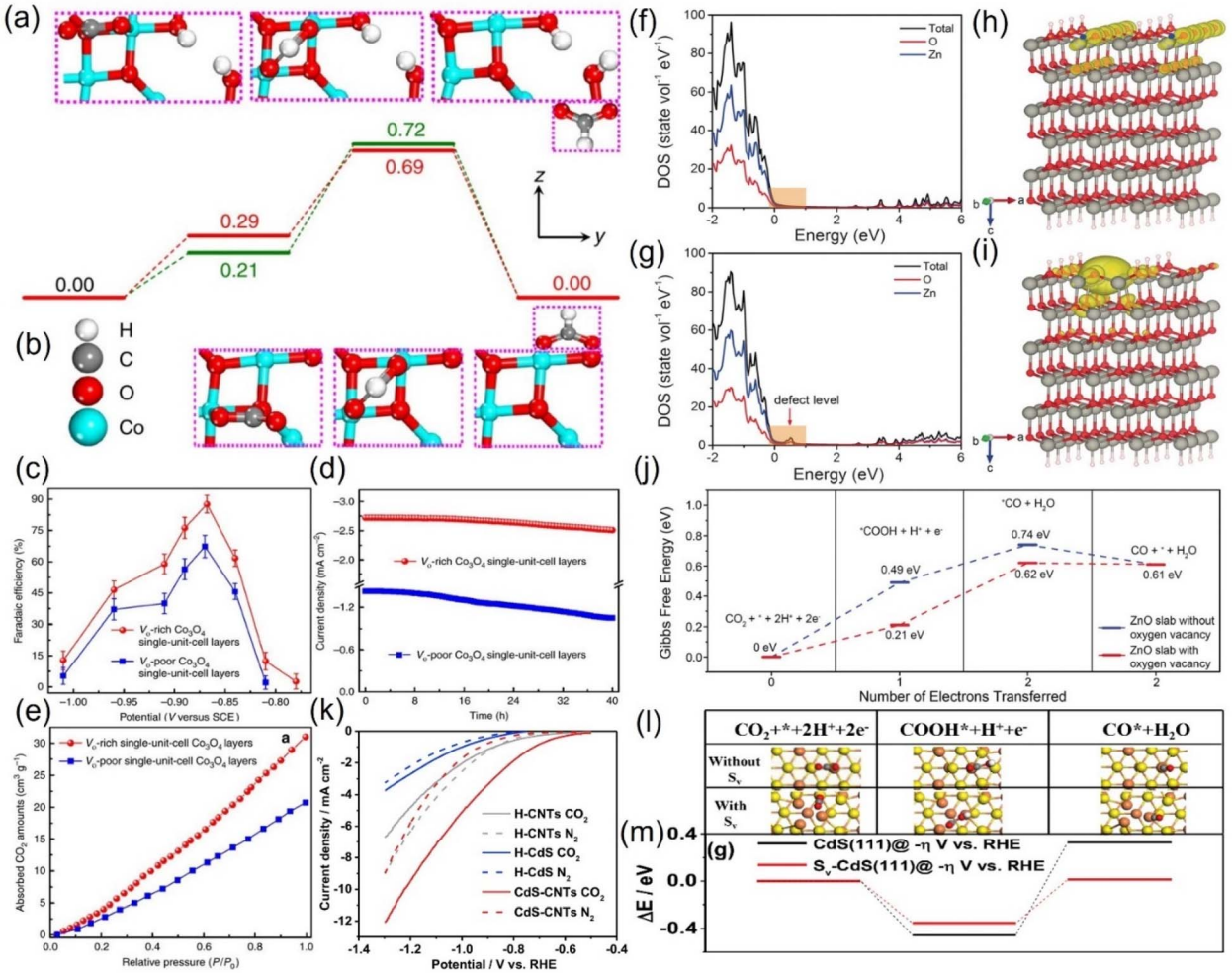

Fig. 8 Gibbs free energy diagrams of (a) V_O-rich and (b) V_O-poor single-unit-cell Co_3O_4 layers. (c) FE_{HCOOH} at different applied potentials. (d) Chronoamperometry tests and (e) CO_2 adsorption isotherms of VO-rich/poor single-unit-cell Co_3O_4 layers. (f and g) DOS. (h and i) Charge density distribution and (j) Gibbs free energy diagrams of (f and h) ZnO slab and (g and i) ZnO slab with oxygen vacancy. (k) LSV curves. (l) Models of different intermediates and (m) DFT calculation results of corresponding intermediates during CO_2RR on CdS without/with S-vacancy (S_v). (a–e) Reproduced with permission.[104] Copyright 2017, Springer Nature. (f–j) Reproduced with permission.[105] Copyright 2018, John Wiley and Sons Ltd. (k–m) Reproduced with permission.[107] Copyright 2020, Royal Society of Chemistry.

can sustain the high FE_{HCOOH} for up to 40 hours (Fig. 8c and d). Revealed by the CO_2 adsorption isotherm, the remarkable upgradation can be attributed to the abundant CO_2 adsorption sites additionally provided by the V_O (Fig. 8e). Combined with DFT calculations, they found that V_O has the effect of stabilizing $HCOO^-$ radicals, reducing the energy barrier to initiate the rate-limiting step (the electron transfer from HCO_3^-) from 0.51 eV to 0.4 eV (Fig. 8a and b). Zeng *et al.* introduced V_O on the surface of ZnO nanosheets *via* H_2 plasma etching, and the current density (16.1 mA cm^{-2}) and FE_{CO} (83%) of the obtained V_O-ZnO nanosheets were 5 and 1.9 times higher than that of untreated ZnO, respectively, which could operate enduringly without deactivation.[105] Combined with the calculation results, they concluded that V_O increases the number of charges near the valence band of ZnO, improves the capture capacity of CO_2, and switches the rate-determining step to the desired surface reaction (Fig. 8f–j).

Besides oxygen vacancies, other anion vacancies have been discovered.[106] For example, Li and colleagues synthesized CdS with ample S vacancies (V_S) by pyrolyzing the mixtures of cadmium chloride and thiourea with serial ratios.[107] At the optimal V_S concentration, the current density of V_S-CdS at 1 V *vs.* RHE can be as high as 20.5 mA cm^{-2}, and the FE_{CO} can reach 95% with an error less than 0.5% (Fig. 8k). In contrast, the activity of the compared traditional CdS is much lower, indicating that the V_S is the main contributor to the performance improvement. The V_S was theoretically revealed to be more prone to adsorb the key intermediate species *COOH, essentially reducing the difficulty of CO generation (Fig. 8l and m).

3.2.2. Cationic vacancies. Cation vacancies profoundly modify the electronic structure and surface properties of catalysts by regulating the removal of metal cations, thereby altering the reaction pathway or reducing the reaction energy barrier, making them more prone to CO_2RR.[108] Particularly, since

oxygen in the environment destroys the anion hole to induce its loss of efficacy, cations that circumvent this adverse situation appear to be preferable.[66] However, the application of cationic vacancies in electrocatalysis has been rarely reported so far. Since their formation barriers are more unfavorable than those of anionic vacancies, their controllable preparation is more complicated and challenging. To overcome these obstacles, researchers have creatively developed novel strategies to accurately construct cationic vacancies. Using strong acid or alkali to targetedly etch metal sites effectively induces the formation of atomic cationic vacancies (Fig. 9a).[101] Due to the strong acid/base solubility of Zn, Mo, Al and Mn atoms, this method is well suited to weed them out. For layered materials, small molecular organics have been developed to effectively assist in the removal of metal atoms, followed by high-temperature annealing or ultrasonic treatment to produce the desired vacancies. For instance, Qu *et al.* successfully fabricated N-doped Ti_3C_2 MXene nanosheets with abundant Ti vacancies (V_{Ti}) through NH_3-assisted etch-pyrolysis method (Fig. 9b).[109] It showed extraordinary electrocatalytic CO_2RR activity even in untreated seawater with FE_{CO} and j_{CO} (the current density corresponding to the CO), achieving a high level of 92% and 16.2 mA cm^{-2}, respectively, as well as durability over 40 hours, which is comparable to the top level in precious metal-based catalysts. DFT calculation results revealed that V_{Ti} had the expected modification effect on the metal site, greatly reducing the formation energy barrier of critical *COOH intermediates and optimized the desorption energy barrier of *CO to lower the desorption threshold of the product CO, thus significantly improving the efficiency of the CO_2-to-CO pathway (Fig. 9c–f). In addition, plasma etching is being sought as a new technology.[110] Specifically, it can be conceptually summarized as a two-step procedure: (1) chemical reactions occur through the interaction of the feed gas with the plasma to produce new species. (2) These generated reactants interact with the substrate surface to remove specific materials.[111] It has the following multiple advantages: (1) there is low time consumption and it can maintain the dryness and cleanliness during the operation. (2)

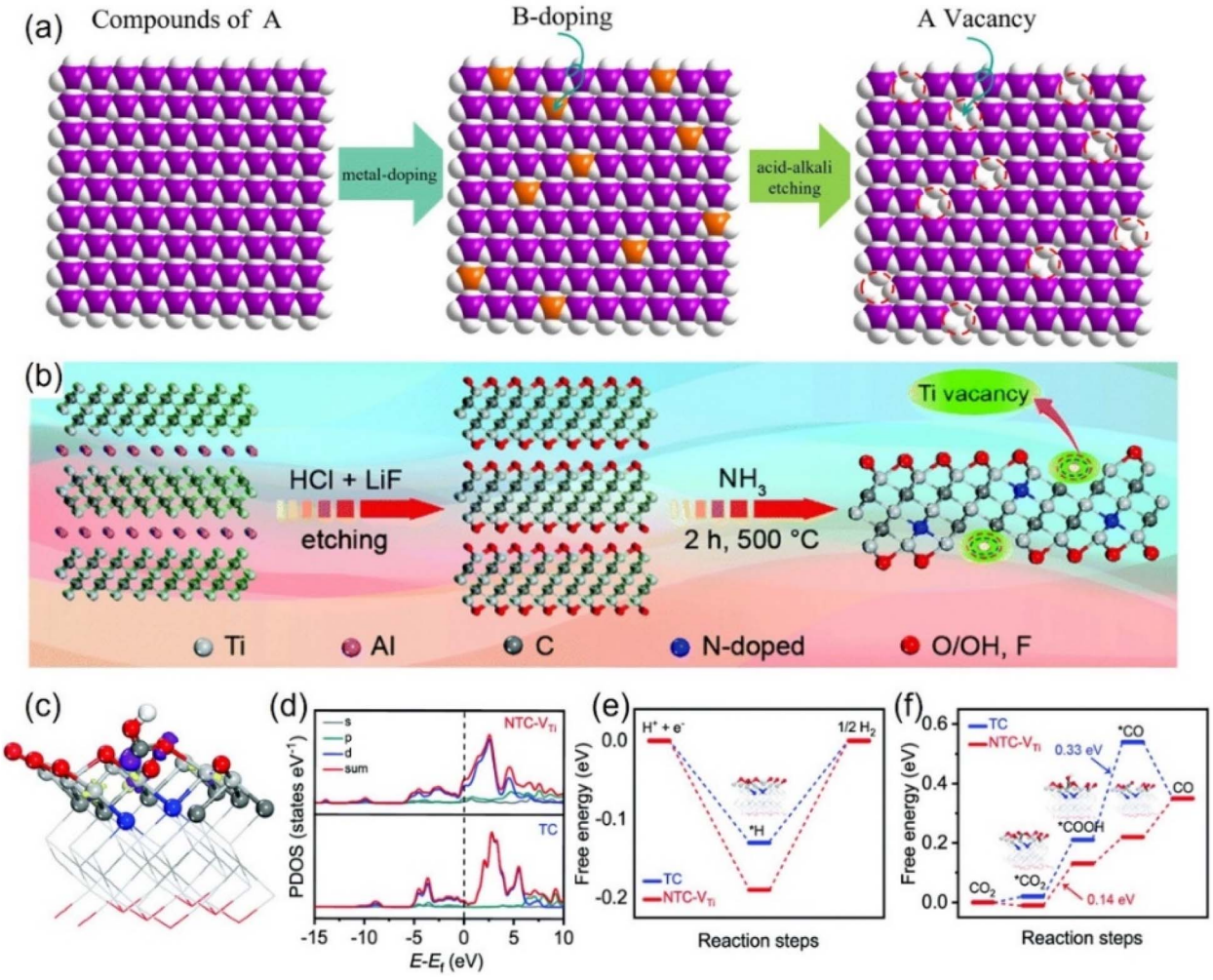

Fig. 9 Schematic diagrams of preparing vacancies through (a) strong acid alkali for targeted-etching and (b) NH_3-assisted etch-pyrolysis. (c) Electron density model (purple: electron accumulation; yellow: electron depletion). (d) Calculated DOS diagrams of *COOH adsorbed on NTC-V_{Ti}. Free energy diagrams of (e) the HER and (f) CO_2RR. (a) Reproduced with permission.[101] Copyright 2023, the Royal Society of Chemistry. (b–f) Reproduced with permission.[109] Copyright 2020, the Royal Society of Chemistry.

The multi-functional characteristics make it possible to prepare the target vacancy defects with high precision on almost any material surface. (3) The etching rate can be well controlled. (4) The selectivity of implementing target atoms is high.[112] Furthermore, some niche preparation methods such as chemical reduction, electrochemical stripping and hydrothermal heat treatment routes have also been reported.[113–115]

3.3. Strain effect

The Sabatier principle points out that the difficulty of combining the key reaction species and active sites has a direct and profound effect on the reaction rate, and a moderate binding energy barrier will significantly increase the yield and selectivity of the target product.[116] In addition, through theoretical modeling, the location of the d-band center has a significant impact on the adsorption strength of species, *i.e.*, the decrease in the d-band center position will weaken the adsorption between the active site and the intermediate species, and *vice versa*.[117]

Strain engineering is a highly suitable means to regulate the central position of the d-band, and a variety of CO_2RR active metals have intense strain response. Furthermore, the strain effect has the unique advantage of breaking through the linear scaling barrier, which will break the original equilibrium space queue between catalyst atoms and cause it to deviate. This will directly fluctuate the binding energy barrier of the key intermediate, which is conducive to the adsorption and activation of CO_2 and the desorption of products and greatly reduces the overall reaction difficulty.[118] These advantages make strain engineering an urgent optimization strategy to be developed. For example, changing the thickness of the Cu sheet on the upper layer of Pt resulted in significant differences in the cell parameters of Cu (3.61 Å) and Pt (3.92 Å), which directly led to the geometric tensile strain of the surface lattice, thus obtaining a more reactive surface with dramatically enhanced the adsorption intensity of the *CO species, even profoundly altering the optimal reactive pathway.[119] Similarly, Wang *et al.* prepared Ag@Cu NPs with Ag as the core coated with Cu shells with a series of thicknesses by controlling the heating time in the synthesis method of polyol reduction. Ag@Cu-20 with a moderate thickness of Cu layer obtained by heating for 20 min shows the highest selectivity to ethylene, which is much better than that of the corresponding SACs (Fig. 10a).[120] This can be attributed to the surface lattice tensile strain effect, which optimizes the surface activity of the

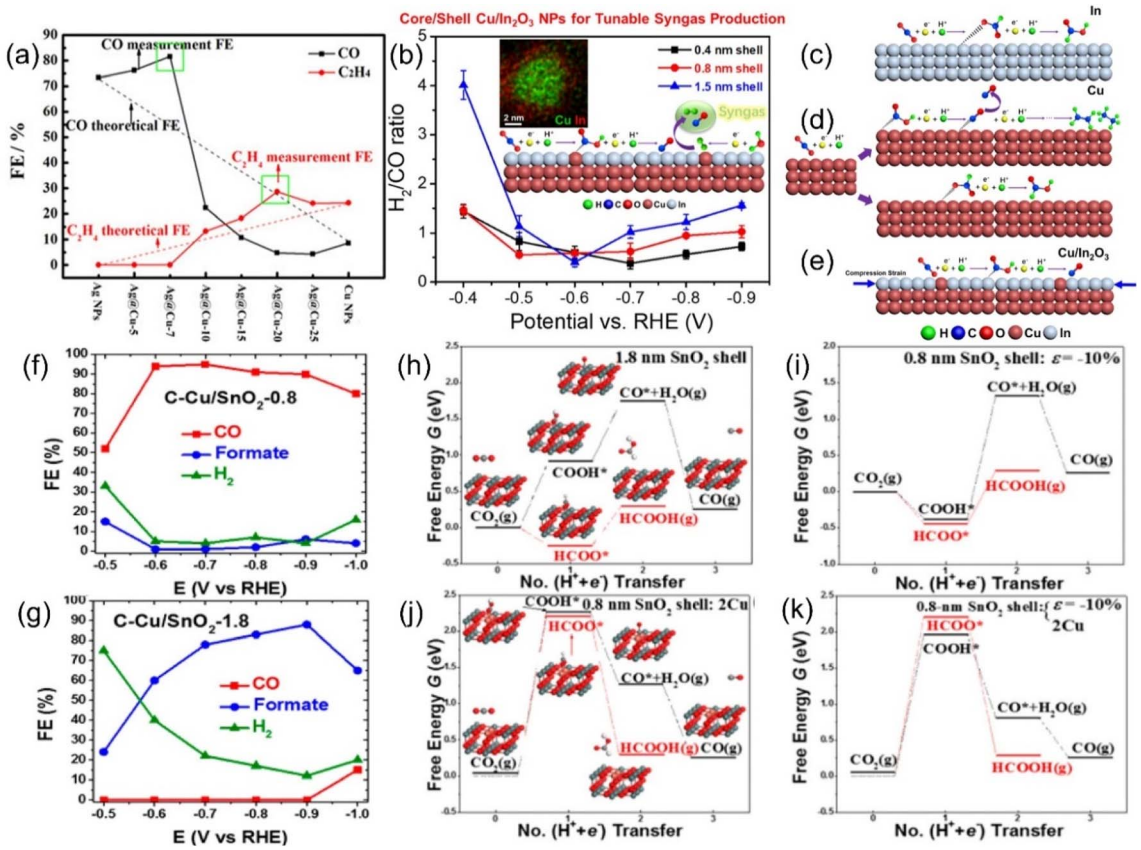

Fig. 10 Theoretical linear "dilution effects" and test values of FEs of CO (black) and C_2H_4 (red). (b) H_2/CO ratios generated by C–Cu/In_2O_3 catalysts. Schematic diagrams of the possible ECO_2RR pathways on (c) In foil, (d) Cu NPs and (e) Cu/In_2O_3 NPs. FEs of various products for the ECO_2RR of (f) C–Cu/SnO_2-0.8 and (g) C–Cu/SnO_2-1.8. Free energy diagrams of two ECO_2RR pathways on SnO_2 shells of different thickness with 10% uniaxial compression of (h) 1.8 nm and (i) 0.8 nm; and 0.8 nm SnO_2 shells with (j) both surface Cu atoms and (k) 10% uniaxial compression. (a) Reproduced with permission.[120] Copyright 2017, American Chemical Society. (b–e) Reproduced with permission.[121] Copyright 2018, American Chemical Society. (f–k) Reproduced with permission.[122] Copyright 2017, American Chemical Society.

material to hydrocarbons and the adsorption strength of *CO. Unfortunately, as the shell thickens, the tensile strain decreases due to its short-range properties, resulting in a decrease in the Faraday efficiency of C_2H_4 after the peak. In another similar core–shell system of Cu coated with In_2O_3, both the current density and the Faraday efficiency of the by-product H_2 and the target product CO can be adjusted by tuning the shell thickness (Fig. 10b).[121] It has been reported that the synergistic effect of compressive strain and Cu doping effect promotes the formation of *COOH rather than the HCOO* intermediate, thus boosting the precipitation of CO (Fig. 10c–e). Interestingly, Sun *et al.* reported another Cu-based material wrapped by SnO_2. When the thickness of SnO_2 is 1.8 nm, the material is more inclined to exhibit the activity of Sn with the higher selectivity of HCOOH, while when it becomes thinner than 0.8 nm, the FE_{CO} overwhelmingly reaches 93% (Fig. 10f and g).[122] Combined with various characterization and theoretical calculation results, this unique phenomenon is attributed to the lattice mismatch between SnO_2 and Cu, resulting in a large compressive strain of up to 10% in the shell (Fig. 10h–k).

Furthermore, the electrocatalytic reduction of carbon dioxide to multi-carbon products involves complex multiple proton and C–C coupled electron transfers, which are not only determined by the intrinsic reactivity of the catalyst but are also related to the spin state of the electrons. Yao *et al.* observed the electrocatalytic activity of spin-enhanced carbon dioxide reduction over oxide-derived copper (OD-Cu) catalysts (Fig. 11a). Due to the magnetic nature of the Cu site, the Faraday efficiency of CO_2RR could be increased by 15% using the OD-Cu catalyst. In addition, the stray field of copper polarizes the electron spins transferred from the neighboring copper, facilitating the conversion of the C–C coupling reaction on the Cu–Cu site to C_2 products (*e.g.*, ethane), thereby reducing the generation overpotential of the C_2 products.[123] Metal-nonmetal hybridized diatomic catalysts were designed and synthesized by An *et al.* Combining spin-polarized DFT and hydrogen electrode computational models, the hybridized M–B diatomic centers are superior to single and double M centers in driving CO_2RR, especially C–C coupling. The electronic spin state of the metal may be particularly important in regulating the selectivity of CO_2RR and the C–C coupling

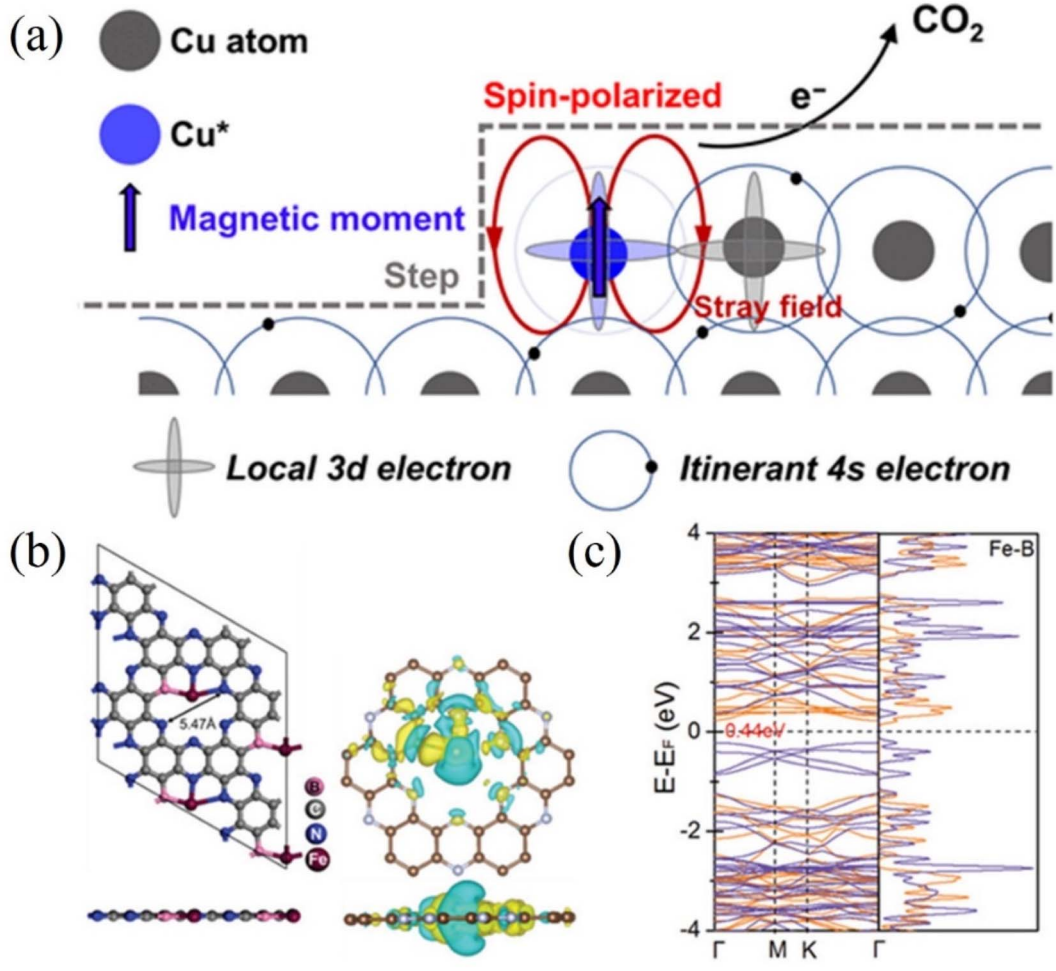

Fig. 11 (a) Spin-related catalysis for the CO_2RR in the OD-Cu catalyst. (b) Optimized structure of Fe@B-C_2N along with the iso-surface of charge density difference. Yellow: charge accumulation; cyan: charge depletion. (c) DFT-calculated electronic band structure and density of states of Fe@B-C_2N near the Fermi level using the HSE06 functional. (a) Reproduced with permission.[123] Copyright 2023, Chinese Chemical Society. (b and c) Reproduced with permission.[124] Copyright 2021, Wiley-VCH Verlag.

potential. Under ambient conditions, the high spin moments of the M–B diatomic site M favor the promotion of C–C coupling and protonation in CO_2RR (Fig. 11b and c). The enhanced spin state of the metal led the authors to predict Fe@B-C_2N as an active catalyst for the conversion of CO_2RR to C_{2+}.[124] Chen *et al.* investigated the effect of oxidation states of Fe ions with different spins in FeN_4C on the electrochemical mechanism of CO_2 conversion to CO/HCOOH. Potential energy analysis revealed that among the two oxidation states with different spins, the rate-limiting step of CO/HCOOH generation catalyzed by intermediate-spin $Fe^{II}N_4C_M$ has lower potential barriers (0.72/0.52 eV). In addition, the overpotentials (−0.03/0.29 V) on $Fe^{II}N_4C_M$ for *CO/*HCOOH generation are also significantly lower than that of other cases. Both confirm that Fe^{2+} ions with intermediate spins in FeN_4C are favorable for the conversion of CO_2 to CO/HCOOH.[125]

3.4. Coordination environment

The coordination environment composed of metal active sites as the core and adjacent bonding atoms is considered to be the universal knob for regulating the electrocatalytic performance. The spatial site of these atoms will create a variety of three-dimensional structures that have a fatal impact on the interaction strength between the CO_2 molecules/intermediate species and the reaction site. Moreover, the lattice distortion and charge transfer between the atoms in the coordination environment directly affect the geometry and electronic structure of the active site, thus endowing the material with a wide range of catalytic properties and even fundamentally changes the reaction pathway of electrocatalytic CO_2RR.[126] Therefore, the in-depth analysis of the coordination environment to clarify the key factors affecting its configuration and the essential way in which it impacts the catalytic process is of great significance, which is helpful to promote the precise regulation of the coordination environment and open up the way for the rational design of a new generation of high-performance industrial grade catalysts.

3.4.1. Basic N-doping M-N-C structure. Among the various coordination atoms, N has the highest probability of appearance, with abundant storage and high selectivity of doping sources. In addition, the doped N atoms fill the overall electron cloud density of the coordination environment to reinforce the active metal site and give them more flexible redox capacity.[127] Therefore, a series of isolated M-N-C coordination structures have been fully studied as the most classical configurations. As far as the current technology is concerned, the controllability of the coordination number of the active metal sites can be achieved by regulating the pyrolysis temperature, but the overall repeatability of the bonding motifs is still not achieved. Fig. 12 shows all possible M-N-C combinations that have been verified, including different coordination numbers and N-atom formations. However, so far, there is no consistent conclusion between theory and experiment as to which configuration has the best electrocatalytic activity for CO_2RR.[66]

At the theoretical level, DFT calculations predicted that the Ni-N-C_3 configuration has the best electroactivity of CO_2RR.[128] Compared with the Ni-C_4 structure, the introduction of an N atom increases the overall charge capacity, enhancing the reduction ability of CO_2 molecules, optimizing the binding energy of CO*, and thus reducing the desorption difficulty of

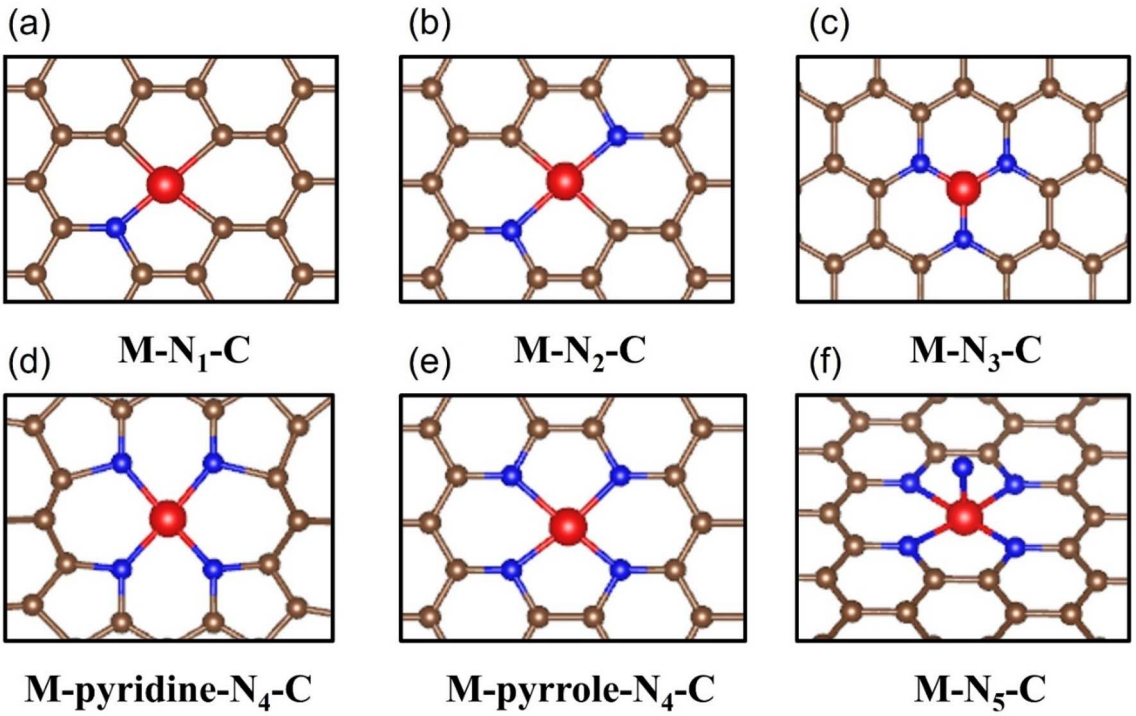

Fig. 12 Schematic diagrams of all reported M-N-C configuration types including (a) M-N_1-C, (b) M-N_2-C, (c) M-N_3-C, (d) M-pyridine-N_4-C, (e) M-pyrrole-N_4-C and (f) M-N_5-C.

CO. However, Ni-N_4 has a lower work function in the charge-neutral state, which makes it more difficult to replenish its charge to the same Fermi level. In another calculation model, when selecting different rate-determining steps, the structure with the highest catalytic potential for CO_2RR was determined to be highly coordinated M-N_4/N_5.[129] For example, Luo *et al.* selected grand canonical potential kinetics (GCP-K) as the basic algorithm for theoretical prediction to obtain the result of Ni-N_4 exhibiting the best catalytic performance (Fig. 13a).[130] This conclusion has also been verified from the experimental results that under −1.05 V *vs.* RHE, such a structure can convert CO_2 to CO with nearly 100% selectivity, and j_{CO} is as high as 40 mA cm^{-2}, which is superior to low coordination configuration with 2N or 3N. The coordination environment of other metals also follows a similar rule. For instance, Li *et al.* reported that the FE_{CO} and j_{CO} in the Co-N_4 configuration in the wider potential range from −0.5 V to −1.0 V *vs.* RHE always occupy one place in the group of Co-N_{4-x} configurations.[131] As shown in Fig. 13d and e, the same M-N_4 configuration while using diverse N-containing ligands will result in differences in the final coordination motifs with vastly different intrinsic activity. For example, when pyrrolic N is used as the ligand, Fe^{3+} is bonded ultra-firmly to achieve the rapid adsorption of CO_2, while in the case of pyridinic N, the catalytic performance is exactly the opposite and the electron cloud of Fe^{3+} is regulated more actively, causing it to be more inclined to absorb electrons and be reduced to Fe^{2+} (Fig. 13b–f).[132]

The experimental evaluation reveals that M-N_x has better electrocatalytic CO_2RR ability than M-N_4 because the former has a higher Gibbs free energy for side reaction, leading to HER with

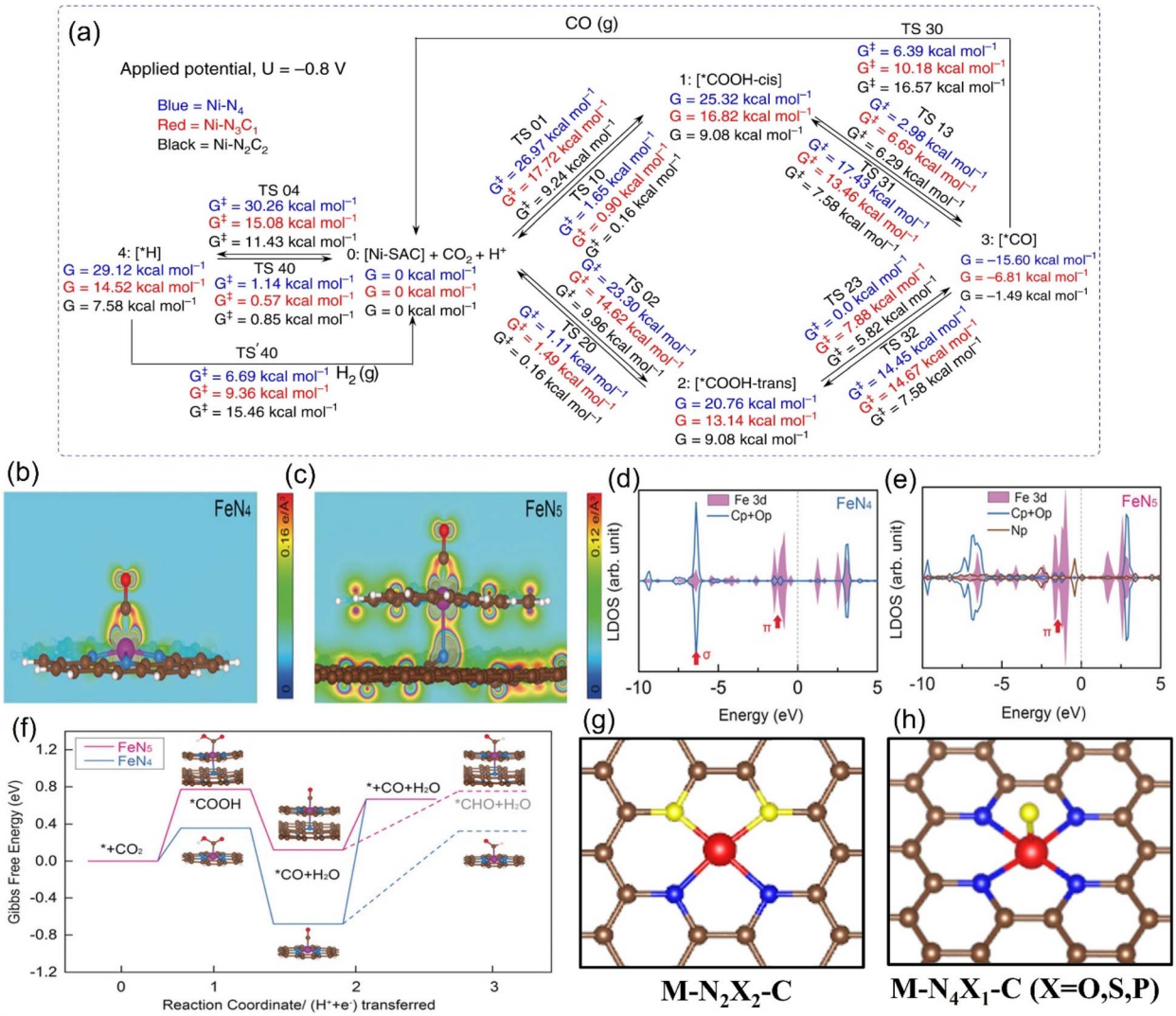

Fig. 13 (a) Schematic representation of calculated free energies with GCP-K as the basic algorithm. Partial charge density of (b) the O-C-Fe-N plane adsorbing CO within the energy range from −1.56 to −0.82 eV for FeN_4 model and (c) the O-C-Fe-N-pyrrolic N plane adsorbing CO within the energy range from −3.31 to −0.99 eV for the FeN_5 model. (d and e) Calculated DOS diagrams of the (d) FeN_4 model and (e) FeN_5 model adsorbing CO and (f) free energy diagram for the ECO_2RR to CO. Schematic diagrams of (g) N-heteroatom co-doped M-N_2X_2-C configuration and (h) axially-coordinated M-N_4X_1-C configuration. (a) Reproduced with permission.[130] Copyright 2020, Springer Nature. (b–f) Reproduced with permission.[132] Copyright 2019, John Wiley and Sons Ltd.

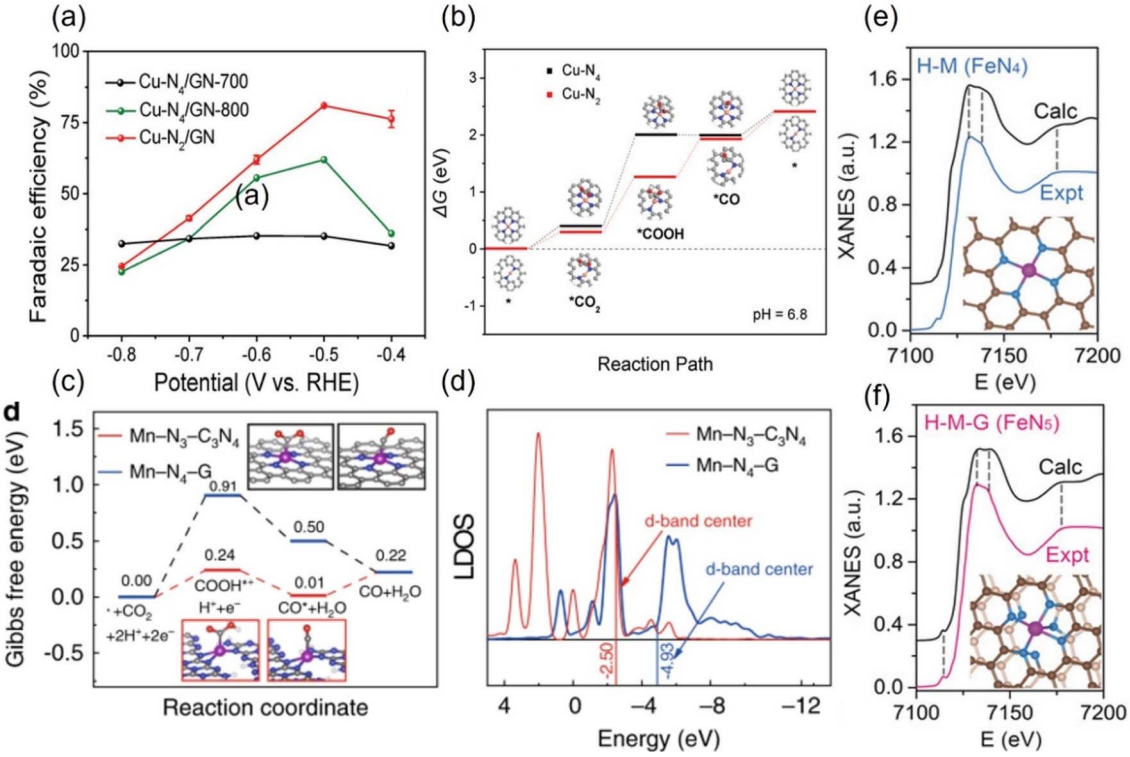

Fig. 14 (a) FE_{CO} diagrams and (b) calculated free energy diagrams for the ECO_2RR of Cu in Cu-N_4 and Cu-N_2. (c) Calculated free energy diagrams for the ECO_2RR and (d) calculated DOS diagrams of Mn in Mn-N_3-C_3N_4 and Mn-N_4-G. Comparison of the experimental with the calculated XANES data of (e) FeN_4 and (f) FeN_5. (a, and b) Reproduced with permission.[135] Copyright 2019, Wiley-VCH Verlag. (c and d) Reproduced with permission.[137] Copyright 2020, Springer Nature. (e and f) Reproduced with permission.[132] Copyright 2019, John Wiley and Sons Ltd.

less probability, while the formation energy barrier of the active *COOH species is lower.[133] For example, in a series of N-coordinated configurations of Co metal atoms (Co-N_2-C, Co-N_3-C, and Co-N_4-C), Co-N_2-C has prominent CO_2RR activity, with a TOF value of up to 18 200 h^{-1}.[134] Similarly, the catalytic performance of Cu-N_2 with FE_{CO} is up to 81%, better than that of Cu-N_4 configuration when applying a small potential of −0.5 V *vs.* RHE (Fig. 14a).[135] As explained by the difference in the geometric structure of different coordination modes, the chemical bond coordinated by double N atoms is not as long as that of four N atoms, which makes the electron transfer of metal sites and adsorbed intermediates faster, thus accelerating the activation of key *CO_2 species (Fig. 14b). In addition, some metals show the advantage of catalyzing CO_2RR in the three-N coordination environment. For example, the rate-limiting step of Ni-N_3, the process of activating CO_2 to a *COOH intermediate, has an easier barrier to cross than that of Ni-N_4.[136] Combined with various *in situ* characterizations, the electrons in the metal center of the Mn-N_3-C_3N_4 coordination structure constructed on three-dimensional carbon nanotubes will rearrange after adsorbing CO_2 molecules, resulting in an increase in the oxidation state.[137] After a round of CO_2RR cycle, the oxidation state will be reduced back to the initial state, which verifies the efficient CO_2RR on this configuration. The FE_{CO} and the corresponding current density can reach 98.8% and 14 mA cm^{-2} at a low bias of 0.44 V *vs.* RHE, respectively. The local density of states analysis demonstrates that the d-band center of Mn-N_3-C_3N_4 is closer to the Fermi level than that of the Mn-N_4 configuration supported on two-dimensional graphene, which greatly reduces the difficulty of CO_2 capture and activation (Fig. 14c and d). Interestingly, on the basis of the planar configuration of M-N_4, the structure of M-N_5 formed by bonding an additional N atom in the axial direction has been developed (Fig. 14f).[132] For example, the oxidation state of the typical Fe-N_5 group obtained by the synchrotron X-ray absorption spectroscopy (XAS) is significantly higher than that of the common Fe-N_4, thus effectively promoting the process of catalyzing CO_2RR.[132] This conclusion has been reasonably explained *via* theoretical calculations, *i.e.*, the d-electron transfer between the Fe site and the additional N atom is more active, which weakens the bonding energy of the former and the *CO species and makes it easier for CO to detach from the output (Fig. 14e and f). It is concluded that even small differences in the coordination environment can have an unpredictable and crucial effect on the electrocatalytic activity of CO_2RR.

3.4.2. Heteroatom-doping M-NX-C structure. The types of M-NX-C structures formed by introducing other coordination elements on the basis of M-N-C are more variable, and the space to be developed is broader. At present, there is still a lack of targeted research in this field, but the coordination of heterogeneous atoms has been recognized as a feasible means to break the symmetry of the overall electron distribution and

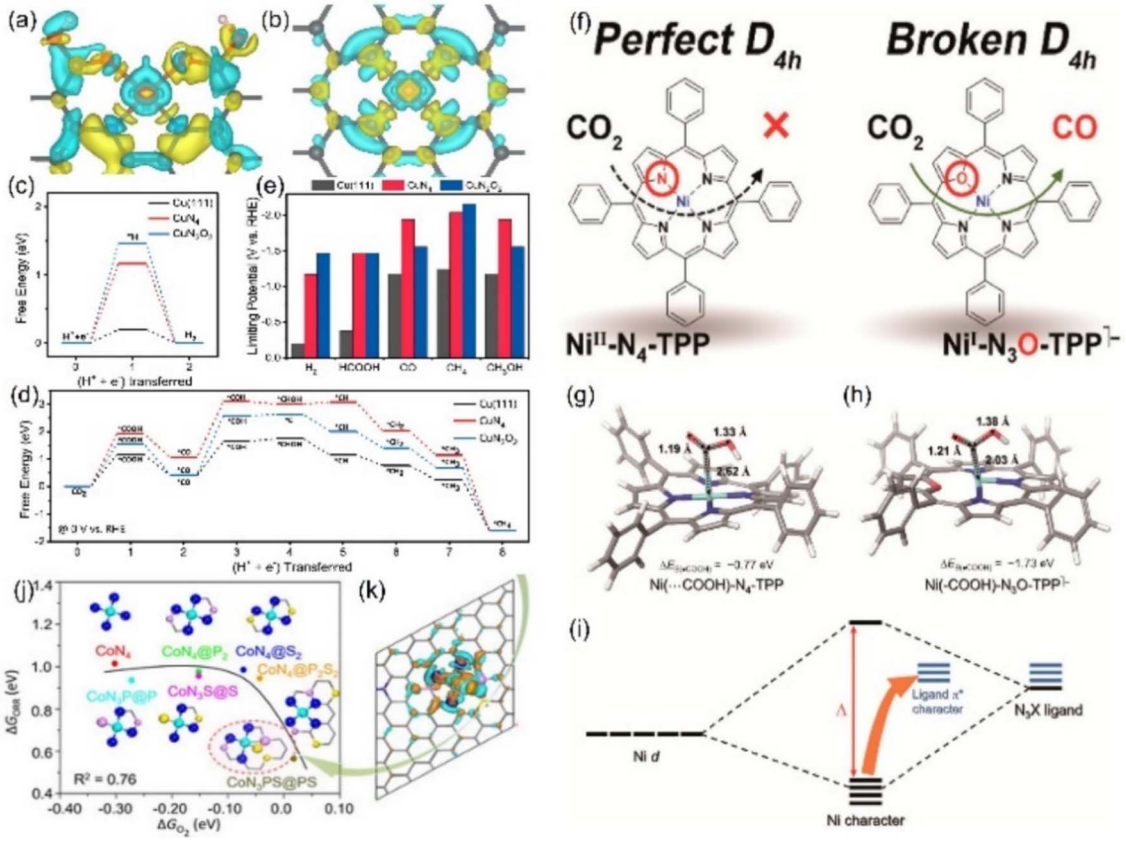

Fig. 15 Charge densities of (a) CuN_2O_2 and (b) CuN_4 (yellow: increase in the number of electrons; blue: the depletion zone). Free energy diagram of (c) the HER and (d) ECO_2RR to CH_4 and (e) summary of the limiting potentials of various products. (f) Schematic diagrams of Ni-N_4-TPP and Ni-N_3O-TPP. DFT-optimized structures of adsorbing *COOH in (g) Ni-N_4-TPP and (h) Ni-N_3O-TPP. (i) Schematic diagram of the molecular orbital. (j) The linear relationship for the overpotential as a function of the O_2^* adsorption energy and (k) charge density difference of the Co site of CoN_3PS. (a–e) Reproduced with permission.[139] Copyright 2021, Springer Nature. (f–i) Reproduced with permission.[140] Copyright 2021, American Chemical Society. (j and k) Reproduced with permission.[142] Copyright 2020, John Wiley and Sons Ltd.

unlock unfamiliar CO_2RR pathways and even the product types.[138] For instance, Cai *et al.* established a coordination environment for Cu-N_2O_2 using the chelating assistance of organic ligands.[139] Due to the strong covalent interaction between the Cu^{2+} center and the adjacent O atoms, the electrons of the whole group can be favorably redistributed, and the binding energy of the 2p orbital of the active Cu site is reduced, which enables its conversion from Cu^{2+} to Cu^+ or Cu^0 with lower oxidation states. The lower positive charge density makes the binding energy barrier of Cu-N_2O_2 to the key *H of the side reaction HER increase compared with the Cu-N_4 configuration, while decreasing it for all the CO_2RR intermediate species (Fig. 15a–e). In addition, Kim *et al.* ingeniously obtained a well-defined Ni-N_3O configuration by directly destroying the symmetric structure of tetraphenylporphyrin (N_4-TPP), denoted as Ni-N_3O-TPP (Fig. 15f).[140] Theoretical calculations reveal that the polarization effect of O doping reduces the chemical valence state of the Ni center, thereby obtaining an ideal bonding strength with the key *COOH species compared with Ni-N_4 configuration synthesized through a similar method (Ni-N_4-TPP) (Fig. 15g–i). In another report with the similar idea, S atom replaces the two diagonal pyrrole N atoms in the porphyrin framework, resulting in a steep increase in the electron transport capacity of the Fe site compared to the traditional Fe-N_4 configuration.[141] In addition, the electronic state density of the active site has been optimized by additional co-doping P and S atoms on the basis of N coordination in making the active Co sites bonded with atoms of three elements (CoN_3PS), and its ORR electrocatalytic activity can be compared to the cutting-edge level of precious metals (Fig. 15j and k).[142]

Other elements except N can also be axially doped to construct the same coordination configuration as M-N_5, as discussed in the previous section (Fig. 11h). For example, Han's team reported the Cd-N_4S_1 structure that exhibits completely different CO_2RR catalytic properties in comparison with the Cd-N_5 configuration.[143] Although both the axial S and N atom play a significant role in activity optimization, the S atom reduces the Gibbus free energy threshold of the rate-limiting step due to its extremely high spin density state with charge delocalization effect (Fig. 16a–c). In addition to the fact that the Cd atom is instinctively inclined to form this configuration due to its large radius, the beneficial effect of the fifth axial heteroatom also acts on other metals. For instance, Xin *et al.* chose organic diphenyl sulfide as the S source to axially incorporate the fifth S

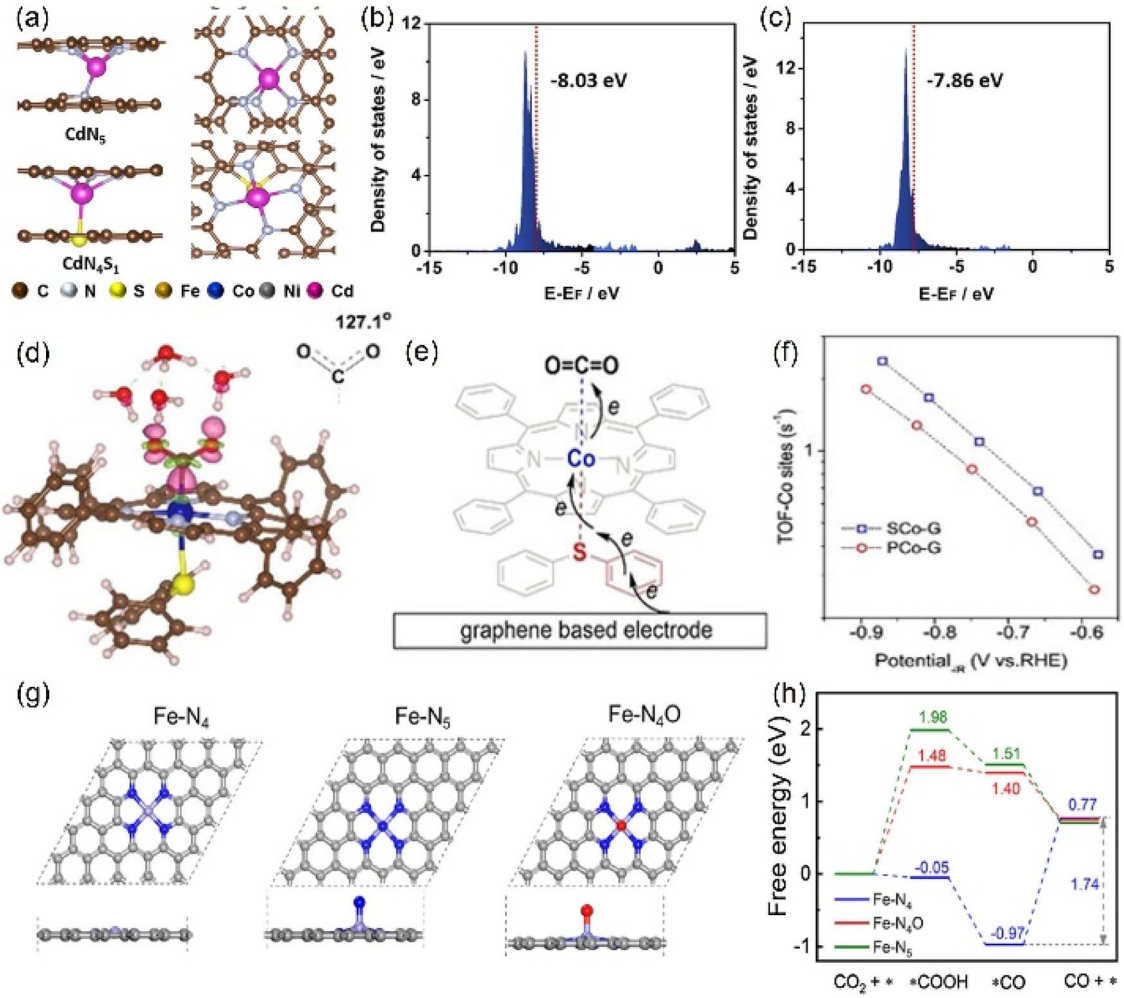

Fig. 16 (a) The side and top structures and (b) the partial density of states of Cd site of CdN_4S_1 and CdN_5 configurations (red line: the d-band center). (d) Charge density difference diagram exhibiting CO_2 activation on the Co atom in Co-N_4S_1. (e) Schematic diagram of the possible electron transfer pathways of the CO_2 activation from graphene, Co-N_4S_1 to CO_2. (g) The side and top structures and (h) Gibbs free energy diagram of the ECO_2RR to CO of Fe-N_4, Fe-N_5 and Fe-N_4O configurations. (a–c) Reproduced with permission.[143] Copyright 2021, John Wiley and Sons Ltd. (d–f) Reproduced with permission.[144] Copyright 2020, John Wiley and Sons Ltd. (g and h) Reproduced with permission.[145] Copyright 2020, Elsevier.

atom to enhance the electron transfer capacity (Fig. 16d and e). The TOF value of Co-N_4S_1 (2.4 s^{-1}) at −0.87 V is 1.5 times that of Co-N_4 (Fig. 16f).[144] In addition, when O is used as the axial ligand of the Fe center, it exhibits excellent stability at low potentials. This can be attributed to the fact that the adsorption energy of *CO species on the Fe-N_4O configuration is much lower than that of Fe-N_4 or Fe-N_5, which makes the precipitation process smoother (Fig. 16g and h).[145] More and more related studies have shown that it is infinitely possible to design different types of coordination environments to develop new areas of electrocatalytic CO_2RR. More in-depth research in this direction will be dominant in the future.

4. Categories of catalysts for ECO_2RR

Thanks to the indefatigable efforts of researchers, great achievements have been achieved in recent decades in improving the activity of ECO_2RR catalysts. Herein, the most advanced and capable ECO_2RR catalysts are representatively classified as atomically-dispersed catalysts, alloys, MOFs and COFs, providing a comprehensive overview of their inherent characteristics and achievements in electrocatalytic performance. Herein, we present more intuitive summaries and comparisons of the cutting-edge ECO_2RR catalysts in Table 3 in combination with structure–activity optimization strategies to provide researchers with the most frontier research level and design inspiration.

4.1. Atomically-dispersed catalysts

Atomically-dispersed metal catalysts (ADMCs) are known to have the highest atomic utilization among common catalytic systems. Compared with bulk metal structures, ADMCs exhibit new or optimized electrocatalytic properties due to their unique geometric, electronic properties, and uniform active sites,

having been widely used in electrocatalytic CO_2RR. However, owing to high cohesion energy and large surface tension, dispersed metal atoms tend to agglomerate and lose their catalytic activity.[199] The strong fixation of the conductive carrier is essential for maximizing the activity and stability of ADMCs.

4.1.1. SACs for ECO$_2$RR to generate CO. Single-atom catalysts (SACs) are the first atomically-dispersed catalysts to be proposed and studied widely. Theoretical calculations have shown that most metal atoms, including s, d, ds, and p regions, have electrocatalytic CO_2RR activity toward the product, mainly CO. However, the electrocatalytic activity needs to be improved, such as CO selectivity and catalytic stability. On carbon-based materials, metal atoms are mainly connected with the substrate through heteroatoms (N, O, S, P, *etc.*) to form stable SACs.[200] Changing the types and coordination environment of center metal atoms can improve the electrocatalytic CO_2 reduction activity.

Due to the non-delocalization characteristic of the 3s orbital, CO is less adsorbed on Mg than other transition metals (Fe, Co, *etc.*), which is beneficial for the high selectivity of CO.[201] According to the simulation of CO generation path, the energy barrier of CO desorption on Mg-C_3N_4 was only 0.13 eV (Fig. 17a–c). The electron transfer number of Mg-C_3N_4 to CO is 0.1 e, which is much smaller than the corresponding Fe-C_3N_4 and Co-C_3N_4 (Fig. 17d–f). However, the FE_{CO} can reach 90% at large applied voltages. In addition, the SA Ca has almost no CO_2RR activity due to the large activation barrier.

Zhao *et al.* synthesized Ni SAs/N-C by the calcination of Ni-MOF, in which the uniformly dispersed Ni-N_3C_1 is the active center of electrocatalysis.[202] When the voltage is −0.89 V, the FE of CO_2 reduction to CO reaches a maximum of 71.9%. Further, a SAC named Ni-N_3-C, where Ni is bonded to three N atoms and has a carbon defect site at an adjacent site, prepared by a two-step process of high-temperature annealing and ion exchange, showed enhanced CO selectivity.[203] The obvious unsaturated coordination greatly accelerated the rate-determining step (RDS), the formation of COOH*, and the FE of CO reached 95.6%, higher than that of Ni-N_4 without carbon defects.

The controllable uniform reaction site represents high reaction selectivity. The precise control of the types of coordination nitrogen atoms (pyridine nitrogen, pyrrole nitrogen, graphite nitrogen, *etc.*) can further improve the unity of the coordination structure of metal atoms. By self-assembly, Zheng *et al.* used melamine and cyanuric acid as raw materials to obtain metallic SAs coordinated with four pyrrole nitrogen.[80] In the electrocatalytic CO_2RR process, the FE (98.5%) of CO on pyrrole-type Ni-N_4 was higher than the corresponding Fe, Cu, and Co. Pyridine-type Fe-N_4 on C_3N_4 also displayed high CO selectivity at −0.6 V.[204] Instead of pyridine nitrogen, high-valent Fe(III) is more easily stabilized by pyrrole nitrogen, exhibiting faster CO_2 adsorption and weaker CO adsorption.[205] During the electrocatalytic process, Fe could remain in its high valence and not be reduced due to the strong coupling effect. When the voltage was greater than −0.5 V, Fe lost a pyrrole N ligand and was reduced. The low-valence single Ni(I) atom, with 9 d electrons, exhibited high inherent CO_2 reduction activity, with FE_{CO} of 97% and stability of up to 100 h at an overpotential of 0.61 V.[206] During the CO_2RR process, the transfer of electrons from the Ni(I) orbital to the 2p orbital of carbon formed $CO_2^{\delta-}$ species, causing the activation of CO_2 and lowering the barrier for CO_2 reduction. Using the template method, Li *et al.* synthesized a high-metal-content single-atom catalyst Co-N_5/HNPCSs, in which Co was coordinated with five nitrogen and uniformly dispersed on the hollow carbon sphere (Fig. 17g–j).[131] Over a wide voltage range, the catalyst produced CO with a selectivity of more than 90%, and the selectivity reached a maximum of 99.4% at −0.79 V. The improved CO selectivity was attributed to the strong adsorption of COOH* and the suitable adsorption of CO* at Co-N_5 sites (Fig. 17k). As the most used MOF precursor, ZIF-8 can effectively isolate the agglomeration of single atoms during calcination.[207] The Zn-N_4 site reduced the reaction barrier of *COOH generation and converted CO_2 to CO with an FE of 95%.[208] Single Mn, Zn, Fe, or Cr atoms are all potential catalysts that can reduce CO_2 to CO.

Due to the participation of multiple electrons in adsorption and desorption reactions, rare-earth-based materials will produce strong adsorption with CO_2RR intermediates, showing a poor electrocatalytic activity. However, owing to the strong metal-carrier interaction, rare earth metals can be easily fixed on the carrier, facilitating the synthesis of single atoms, which gives them CO_2RR activity. Due to large atomic radii and abundant electron orbitals, isolated Sc and Y tend to adsorb at large defect sites and form five- or six-coordinated configurations. Liu *et al.* synthesized Sc- and Y-SACs (Y_1/NC and Sc_1/NC), where each metal atom was simultaneously bonded to three nitrogen atoms and three carbon atoms.[209] In the process of CO_2RR, Y_1/NC and Sc_1/NC reached the highest FE_{CO} of 88.3% and 81.3% at −0.58 V and −0.68 V, respectively.

4.1.2. DACs for ECO$_2$RR to generate CO. Diatomic catalysts (DACs) and multi-atom catalysts are the extension of SACs, which provide more possibilities for the adsorption of reaction intermediates. Unlike SACs, the introduction of the second and the third metal atoms can not only further regulate the electronic structure but also add new adsorption active sites, breaking the limit of linear relationship. According to the types of metals, DACs are mainly divided into homologous binuclear and heterologous binuclear metals.[210–212]

The dispersion of Pd atoms with strong CO adsorption on the Au surface in the form of diatomic Pd–Pd would adjust the CO adsorption strength to moderate and further enhance the CO selectivity (Fig. 18a).[213] Pb_2 DACs could be prepared by anion replacement deposition, and the distance between Pd and Pd was 1.96 Å, indicating the formation of a dual-nuclear site.[214] At an applied voltage of −0.85 V, Pb_2 DACs presented high selectivity for CO with an FE of 98.2%, which was much higher than that of the corresponding single atom catalyst (65%) and nanostructured catalyst (80%). The CO poisoning reaction of Pd nanoparticles was not conducive to CO_2RR, resulting in a large reaction barrier. However, for Pd-based atomically-dispersed catalysts, the activation of CO_2 to COOH* was the RDS, and both isolated Pd_1 and Pd'_1 exhibited greater free energy of RDS than Pd_2. The enhanced electrocatalytic activity was attributed to the electron transfer between Pd–Pd.

Table 3 Comparison of ECO_2RR performance on advanced catalysts combined with optimization strategies

Catalyst	Optimization strategy	FE (%)	Current density (mA cm^{-2})	Applied potential (V *vs.* RHE)	Electrolyte	Device	Ref.
B-CuO	Modulating the electronic structure of the active center	C_{2+} (62.1)	−139	−0.62	1 M KOH	Flow cell	146
Cu(B)		C_2H_4 (52)	−70	−1.1	0.1 M KOH	H-cell	147
PDI@Cu(Cu-C)		CH_4 (38.9)	−145	−1.0	0.1 M $KHCO_3$	Flow cell	148
$Cu_{1.5}$/GDY		CH_4 (57.3)	−312	−1.7	1 M KOH	Flow cell	149
Cu-N-C-900		CH_4 (38.6)	−38.3	−1.6	0.1 M $KHCO_3$	H-cell	150
PSB-CuN_3		$HCOO^-$ (97.9)	−127.7	−1.1	0.5 M $KHCO_3$	Flow cell	151
Cu-on-Cu_3N		C_2H_4 (39) C_3H_7OH (6)	−23	−0.95	0.1 M $KHCO_3$	H-cell	152
Cu_3N_x		C_2H_4 (56)	−307	−1.15	1 M KOH	Flow cell	153
Cu_3P		$HCOO^-$ (8)	−0.5	−0.2	0.5 M $KHCO_3$	H-cell	154
$P_{0.075}$-Cu		C_2H_4 (30.7)	−17.57	−1.6	0.1 M $KHCO_3$	H-cell	155
P-doped Cu		C_2H_4 (40)	−210	—	1 M KOH	Flow cell	156
Oxide-derived Cu		C_{2+} (60.1)	−11	−1.0	0.1 M $KHCO_3$	H-cell	157
CuO-derived Cu		C_{2+} (7)	−400	—	1 M KOH	Flow cell	158
CuS_x-DSV		C_3H_7OH (15.4)	−20	−1.05	0.1 M $KHCO_3$	H-cell	159
Cu_2S-Cu-V		C_{2+} alcohol (32)	−400	—	1 M KOH	Flow cell	160
SNC@$Cu_{1.96}S$		CO (85.2)	−21	−0.84	0.5 M $KHCO_3$	H-cell	161
Sm_x-CuS_y		HCOOH (92.1)	−300	—	1 M KOH	Flow cell	162
Cu_2-CuN_3		C_2H_5OH (51)	−28.2	−1.1	0.1 M $KHCO_3$	H-cell	163
Cu-N-C		C_2H_5OH (55)	−16.2	−1.2	0.1 M $CsHCO_3$	Flow cell	164
$Cu_2P_2O_7$	Constructing vacancy defects, including anionic and cationic vacancies, altering the lattice ordering and electronic structure to optimize electron transport pathways and energy barriers for critical species	C_2H_4 (41.8)	−200	—	0.1 M KOH	MEA-based	
V_{Se}-$Cu_{2-x}Se$		C_2H_5OH (68.1)	−10.96	−0.8	0.5 M $KHCO_3$	H-cell	165
$Cu_{1.63}Se$(1/3)		CH_3OH (77.6)	−41.5	−2.1	[Bmim]PF_6 (30 wt.)/CH_3CN/H_2O (5 wt.)	H-cell	166
BiCuSeO		HCOOH (93.4)	−267	−1.1	1 M KOH	Flow cell	167
Cu_2Se		CH_3CH_2OH (84)	−50	−0.6	0.3 M $NaHCO_3$	H-cell	168
Cu_2Te		CH_4 (63)	−300	—	1 M $KHCO_3$	Flow cell	169
CuO_x-V_o		C_2H_4 (63)	−30	−1.4	0.1 M $KHCO_3$	H-cell	170
$O_{2,\ 10\ min}$-plasma Cu		C_{2+} (60)	—	—	0.1 M $CsHCO_3$	H-cell	171
e-CuOHFCl		C_2H_4 (36.3)	−18.5	−1.0	0.1 M $KHCO_3$	H-cell	172
Cu_2O_{Cl}		C_3–C_4 (10)	−7	−1.6	0.1 M KCl	H-cell	173
Cu_KI		C_2H_4 (44.5)	−40	−1.15	0.1 M $KHCO_3$	H-cell	174
O_2 plasma-activated Cu foil		C_2H_4 (60)	−2	−0.9	0.1 M $KHCO_3$	H-cell	175
Vo-rich ZnO nanosheets		CO (83)	−16.1	−1.1	0.1 M $KHCO_3$	H-cell	105
Nb_4N_5-NO/NC		CO (91)	−2.8	−0.8	0.1 M $KHCO_3$	H-cell	176
Ni-N_3-V		CO (90)	−65	−0.9	0.5 M $KHCO_3$	H-cell	177
Bi_2S_3–Bi_2O_3@rGO		HCOOH (90.1)	—	−0.9	0.1 M $KHCO_3$	H-cell	178
V_O-SnO_x/CF		HCOOH (86)	−30	−1	0.1 M $KHCO_3$	H-cell	179
H-InO_x NRs		HCOOH (91.7)	—	−0.7	0.5 M $KHCO_3$	H-cell	180
SnO_x		HCOOH (88.6)	−15	−0.98	0.5 M $KHCO_3$	H-cell	181

Table 3 (*Contd.*)

Catalyst	Optimization strategy	FE (%)	Current density (mA cm^{-2})	Applied potential (V *vs.* RHE)	Electrolyte	Device	Ref.
CdS		CO (100 ± 0.5)	−20.5	−1.1	0.5 M $KHCO_3$	H-cell	182
Cu/CeO_{2-x} HDs		CH_4 (54)	—	−1.2	0.1 M $KHCO_3$	H-cell	183
CdS-CNTs		CO (92)	−11.4	−1.2	0.1 M $KHCO_3$	H-cell	106
De-Au_3Cu		CO (94.3)	—	−0.43	0.5 M $KHCO_3$	H-cell	184
Cuv-Cu_2O		C_2H_4 (51)	−15.7	−0.76	0.1 M $KHCO_3$	H-cell	185
Bi/Bi_2O_3-CP		HCOOH (90.4)	—	−0.87	0.5 M $KHCO_3$	H-cell	186
Vo-rich SnO_2		CO (92.5)	−44.2	−1.1	0.5 M $KHCO_3$	H-cell	187
Iodide-mediated Cu	Strain engineering can break the queue of the original equilibrium	C_2H_4 and oxygenates (25)	—	—	0.1 M $KHCO_3$	H-cell	188
Cu–CuI	between atoms to optimize the	C_{2+} (71)	−832.4	−1.0	1 M KOH	Flow cell	189
Cu/Cu_xOF	energy barrier of key reactive	CH_3COOH (27)	−15	−0.3	1 M KOH	Flow cell	190
Ag,S-Cu_2O/Cu	species	CH_3OH (67.4)	−122.7	−1.18	$BMImBF_4/H_2O$ (molar ratio 1 : 3)	H-cell	191
Cu_2O@Cu-MOF		CH_4 (63.2)	−14	−1.71	0.1 M $KHCO_3$	H-cell	192
$Cu(OH)_2$/CuO		C_{2+} (64.5)	−26.2	−0.9	0.1 M $KHCO_3$	H-cell	173
3D dendritic Cu-Cu_2O/Cu		C_2 (80.7)	−11.5	−0.4	0.1 M KCl	H-cell	193
Ag-Cu_2O_{PB}		C_2H_5OH (34.15)	−4	−1.2	0.2 M KCl	H-cell	194
Tin-based oxides SnO_x/Sn GDE		$HCOO^-$ (64)	−3	−1.399	0.1 M $KHCO_3$	H-cell	195
Pd/SnO_2 NSs		CH_3OH (55)	−1.45	−0.24	0.1 M $NaHCO_3$	H-cell	196
SnO_2-0.8/C-Cu		CO (93)	−4.6	−0.7	0.5 M $KHCO_3$	H-cell	122
Cu/SnO_x-CNT (6.2 SnO_x)		CO (89)	−11.3	−0.99	0.1 M $KHCO_3$	H-cell	197
Cu/SnO_x-CNT (30.2 SnO_x)		HCOOH (77)	−4	−0.99	0.1 M $KHCO_3$	H-cell	197
Zn_2SnO_4/SnO_2		HCOOH (77)	−5.77	−1.08	0.1 M $KHCO_3$	H-cell	198

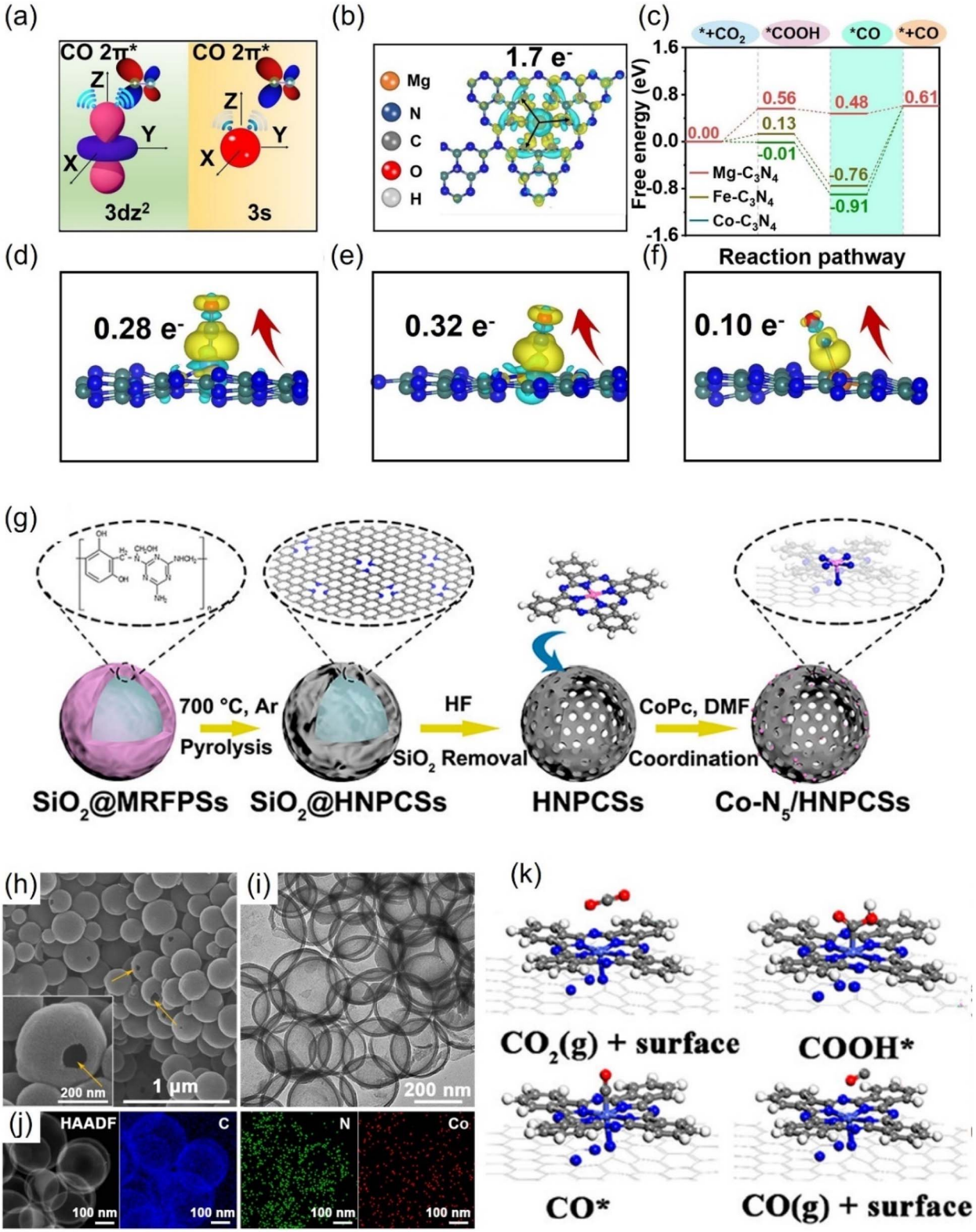

Fig. 17 (a) Comparison of the schematic diagram for CO adsorbed on $3d_{z^2}$ and 3s orbitals. (b) The charge density differences and Bader charge transfer for Mg-C_3N_4. (c) Free energy diagram and (d–f) charge density differences and Bader charge transfer for CO adsorbed on Co-C_3N_4, Fe-C_3N_4 and Mg-C_3N_4. (g) Schematic illustration, (h) SEM, (i) TEM, (j) HAADF-STEM and EDS images and (k) optimized structures for the intermediates. (a–f) Reproduced with permission.[201] Copyright 2021, Wiley-VCH GmbH. (g–k) Reproduced with permission.[131] Copyright 2018, American Chemical Society.

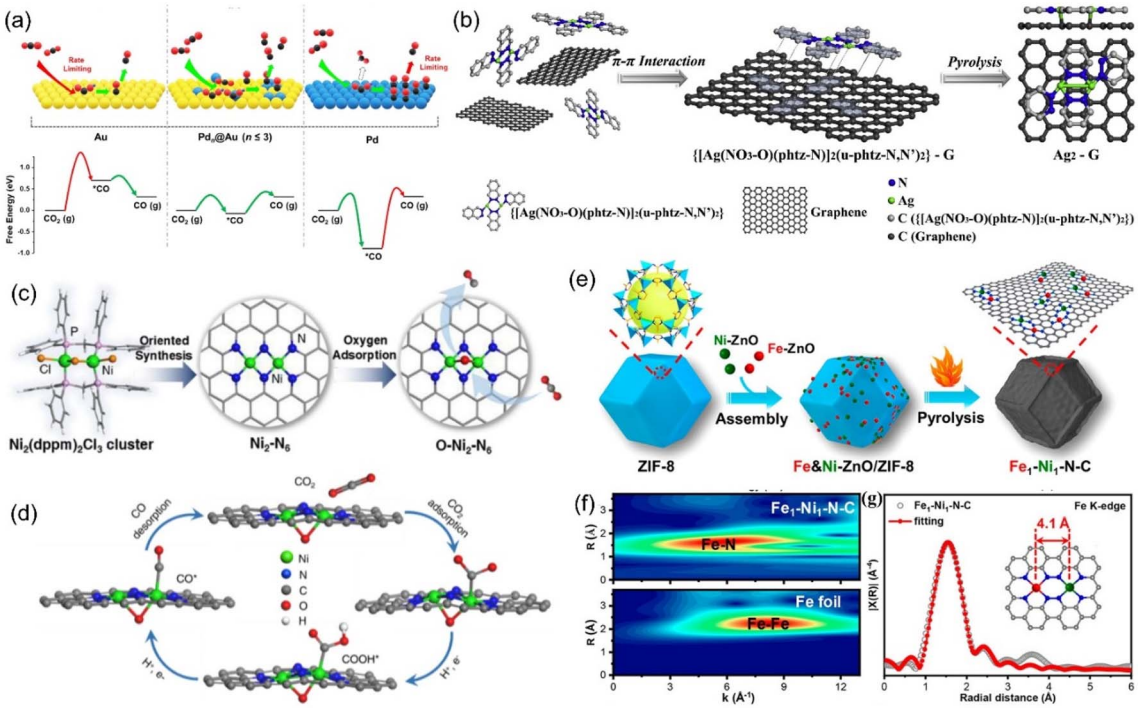

Fig. 18 (a) Illustration of the concept using atomically-dispersed Pd sites on Au surface to enhance CO_2 reduction. (b) Synthetic illustration of the Ag_2-G catalyst. (c) The synthesis process of the Ni_2-N_6 catalyst and (d) proposed reaction pathways on O-Ni_2-N_6. (e) Synthetic illustration of Fe_1-Ni_1-N-C; (f) WT plots for Fe element. (g) Fe K-edge EXAFS spectrum. (a) Reproduced with permission.[213] Copyright 2019, American Chemical Society. (b) Reproduced with permission.[215] Copyright 2020, Elsevier B.V. All rights reserved. (c and d) Reproduced with permission.[218] Copyright 2021, American Chemical Society. (e–g) Reproduced with permission.[221] Copyright 2021, American Chemical Society.

The AgN_3–AgN_3 sites can be obtained by fixing a binuclear Ag precursor to graphene through the π–π interaction (Fig. 18b).[215] Two Ag atoms interact with C and O at the same time, stabilizing the CO* intermediate and reducing the reaction barrier for the formation of *COOH. At −0.7 V, the current density of 11.87 mA cm^{-2} could be achieved, and the FE of CO reached 93.4%. When metal oxides or sulfides and alloys are used as the support, dispersed atom-based catalysts are more likely to achieve high loading capacity. Jiao *et al.* synthesized Cu-APC, with atomic copper pair (Cu_1^0–Cu_1^{x+}) sites by adding Cu onto Te defects of the $Pd_{10}Te_3$ alloy nanowires.[216] In the copper pair, Cu_1^{x+} adsorbed water molecules in the electrolyte and promoted the adsorption and activation of CO_2 at the adjacent Cu_1^0 sites. In 0.2 M $NaHCO_3$, the FE_{CO} of 0.10%-Cu-APC was 92%, while the original APC mainly showed HER, implying that the Cu_1^0–Cu_1^{x+} was the active site of CO_2RR.

The synergistic effect of heteronuclear metal atoms on the electronic structure is obvious. Without direct bonding, M1 and M2 are merely adjacent and are connected by bridging bonds (M1-X-M2), exhibiting enhanced CO_2RR activity than the individual M1 or M2. The active sites of catalysts can change from a single atom to an atomic pair by changing the synthetic conditions. For example, when Fe-ZIF-8 was calcined in pure argon, the product was SAC Fe_1-N_4-C, and the iron content was 0.155 wt%.[217] However, when hydrogen was introduced into argon, Fe atoms underwent a transition from single-core to dual-core. When the hydrogen content was 5%, 80% of the iron in the product was in the form of atomic pair (Fe_2-N_6), and the iron content was 0.313 wt%. The orbital coupling between the two Fe sites reduced the energy gap between the antibonding state and the bonding state in *CO adsorption, improving the selectivity of electrocatalytic products. Similarly, Ni_2-N_6 was successful synthesized using Ni_2 organic molecules as the precursor, where two of the Ni atoms share two nitrogen atoms (Fig. 18c).[218] In the process of CO_2 adsorption, the two complex-unsaturated Ni atoms tended to adsorb oxygen in the solution to form an oxygen bridge bond (Ni–O–Ni), generating more active O–Ni_2–N_6 (Fig. 18d).

Due to the strong Fe–CO interaction, the desorption of CO* on Fe-SACs was the RDS for CO_2RR, and the selectivity of Fe-N-C for CO was only 80%.[219] With the assistance of Zn, the Ni–Fe atomic pair was successfully synthesized with ZIF-8, where the distance between Fe and Ni was 4.1 Å (Fig. 18e–g). After the introduction of Ni, the charge transfer of Fe to CO in the Fe-Ni-N_6 catalyst was less than that in the corresponding catalyst without Ni. In Fe_1-Ni_1-N-C, the adsorption of CO_2 occurred at the Fe site, while the adjacent Ni atom promoted the formation of COOH* on the iron atom through a remote electron interaction *via* the N atom. At a low voltage of −0.5 V, Fe_1-Ni_1-N-C still has 96.2% FE against CO. When the atomic pair was composed of Ni and Zn atoms, Ni was the main adsorption site. The addition of Zn at the Ni site reduced the gap between the d band center of Ni and the Fermi level, enhanced the bonding between the metal and C, and presented an obvious

acceleration effect in both kinetic and thermodynamic aspects.[220] The FE for CO was more than 90% in the wide voltage range (−0.5 to −1.0 V), and the maximum reached 99%.

From the view of theoretical calculations, the in-depth analysis of the nature of ECO_2RR activity gain in polymetallic systems can be performed. Atomic-level control of the coordination environment and electron distribution of electrocatalysts is an effective strategy to improve the electrocatalytic performance, but there are still significant challenges.[222] Previous work has shown that synergistic interactions between atoms in a catalyst can locally tune the electronic structure, weakening the adsorption energy of the reaction intermediates and effectively lowering the energy barrier of the catalytic reaction.[223] Theoretical calculations showed that the co-catalytic strategy affects the adsorption or desorption of adsorbates on the catalyst surface, influencing the d-band centers of the metal atoms and thus changing the free energy barriers.[220] Lu *et al.* used nickel–zinc diatomic coordination to change the d-state of the metal atoms, resulting in significantly enhanced synergistic effect compared to monoatomic catalysts. DFT calculations showed that this synergistic effect enhances the catalytic performance due to the reduction of the distance between the center of the d-band of Ni–Zn orbitals and Fermi energy level and the enhancement of the intermediate's electronic interactions with the active center (Fig. 19a). This lowers the free energy barrier in the thermodynamic pathway, reduces the activation energy, and strengthens the metal–carbon bond in the kinetic pathway. Ni–Zn diatomic catalyst can achieve 99% Faraday efficiency at −0.8 V.[220] Wang *et al.* designed an efficient catalyst with CoPc traced on Fe-N-C. After the positioning of CoPc molecules, the synergistic interaction resulted in the movement of the d-band of the Fe center toward the Fermi energy level, which enhanced the reactivity of the Fe center, and this electronic interaction was reflected in the adsorption of reactive intermediate species (Fig. 19b and c). As a result, CO desorption on the catalyst's surface was promoted, and the

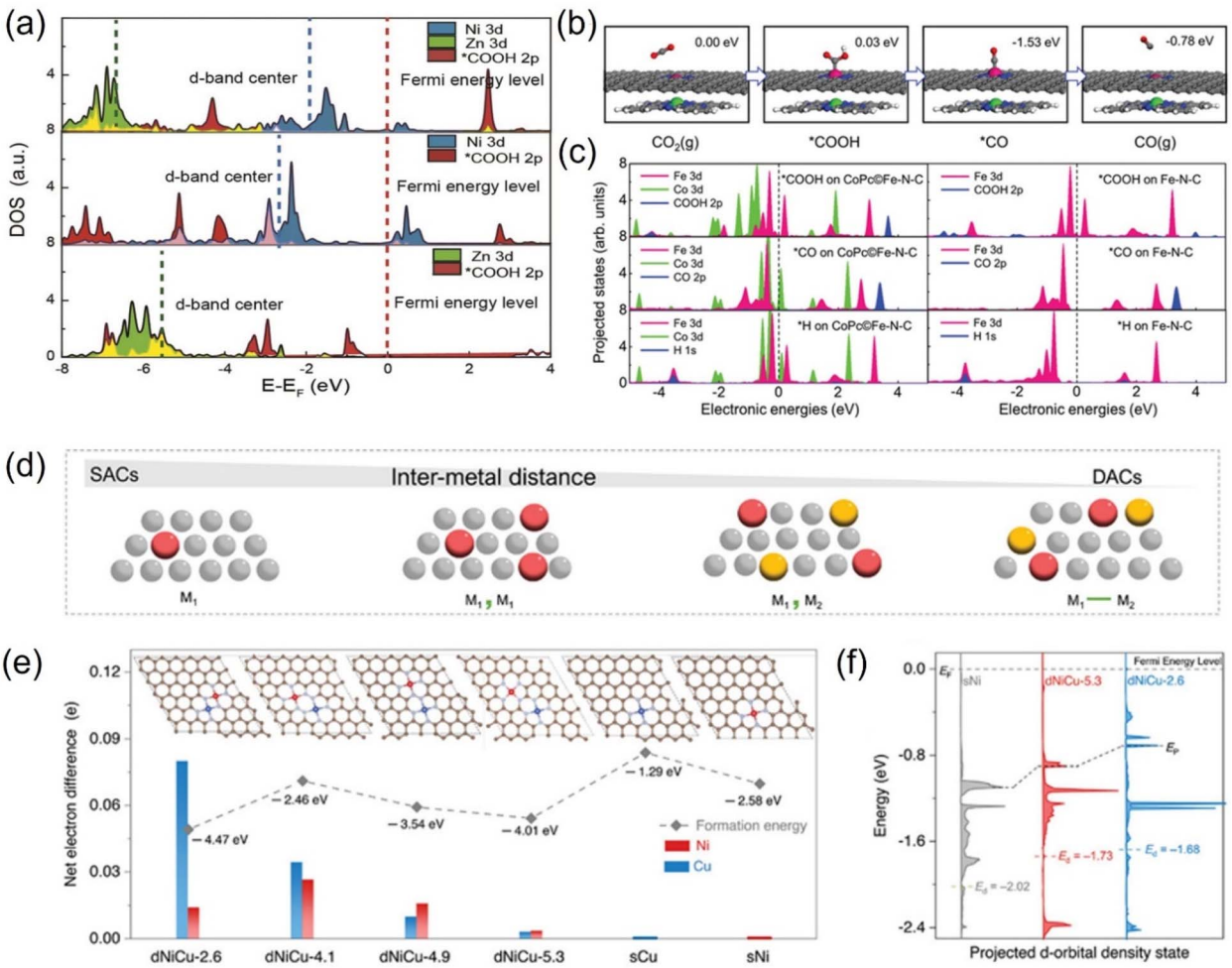

Fig. 19 (a) Projected DOS (PDOS) for Zn/Ni 3d orbitals and oxide 2p orbitals in COOH. (b) Schematic atomic structure of the CO_2RR process on the Fe site in CoPc©Fe-N-C (C: gray; N: blue; O: red; H: white; Fe: pink; Co: green). (c) PDOS of adsorption structures of $^*COOH$, $^*CO$, and $^*H$ on CoPc©Fe-N-C and Fe-N-C. (d) Schematic of SACs and DACs showing the change in the site proximity with different models. (e) Net electron difference of Ni and Cu sites in different dNiCu models. (f) Calculated DOS diagram of the Ni d-orbital for dNiCu-5.3, dNiCu-2.6, and sNi models. (a) Reproduced with permission.[220] Copyright 2021, Wiley-Blackwell. (b and c) Reproduced with permission.[224] Copyright 2019, Wiley-Blackwell. (d–f) Reproduced with permission.[225] Copyright 2023, Wiley-Blackwell.

competing HER on the Fe-N site was suppressed, realizing a high CO Faraday efficiency.[224] Qiao *et al.* investigated the relationship between synergistic and intermetallic interactions using a combination of theoretical simulations and experiments. In the case of NiCu DACs, the electronic contribution from the Cu center is transferred through the NC substrate to the Ni center and finally reaches the *COOH intermediate. This electron transfer through the structure is likely to be the result of non-bonding synergies between neighboring DACs (Fig. 19d–f). Moreover, the synergistic effect modulates the electronic structure and promotes intermediate layer adsorption, thus improving the electroreduction activity and selectivity.[225]

4.1.3. ADMCs for ECO_2RR to generate other products. In addition to CO, atomically-dispersed catalysts can catalyze CO_2 reduction to produce higher value products such as formic acid, methane, and ethanol. The p-block metal, Sb, Sn, Bi, and In can be used for the formation of formic acid.[84,226] By freeze-drying, Zu *et al.* synthesized a kilogram-scale Sn-SAC, in which positively charged Sn atoms were uniformly dispersed onto N-doped graphene (Fig. 20a–c).[227] At a small overpotential of 60 mV, the Sn-SAC reduced CO_2 to formate on account of both enhanced CO_2 adsorption and diminished HCOO* adsorption. Mo-based SACs have the potential to produce high-value formate.[228] For multiple electron transfer products and C_{2+} products, dispersed

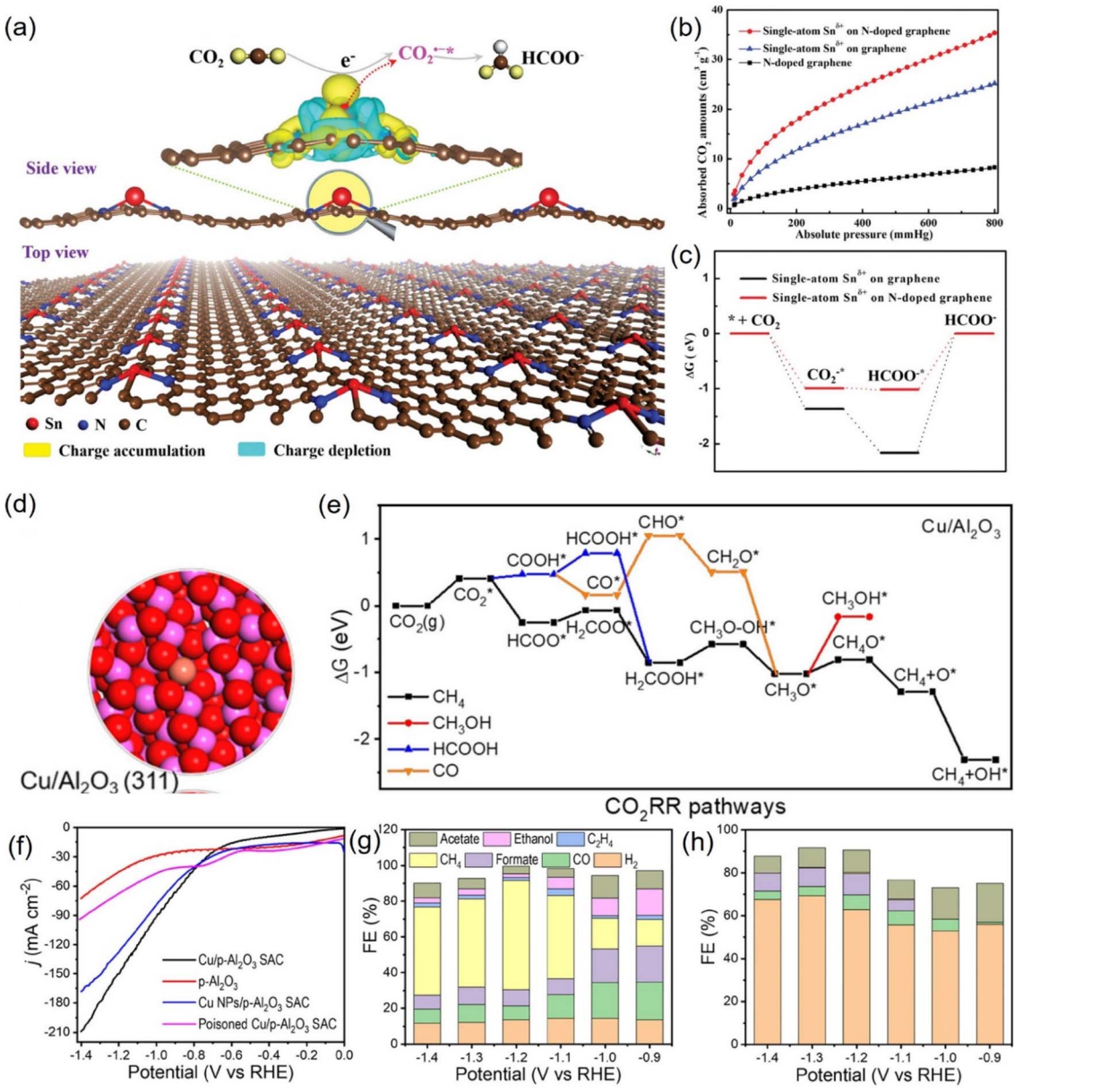

Fig. 20 (a) 3D differential charge densities of single-atom $Sn^{\delta+}$ on N-doped graphene for CO_2R into formate. (b) CO_2 adsorption isotherms and (c) calculated free energy diagrams. (d) Electronic structure of Cu/Al_2O_3 SAC. (e) Calculated free-energy diagrams for the CO_2RR over Cu/Al_2O_3 SAC. (f) LSV curves and FEs of various products for (g) $Cu/p\text{-}Al_2O_3$ SAC and (h) $p\text{-}Al_2O_3$. (a–c) Reproduced with permission.[227] Copyright 2019, Wiley-Blackwell. (d–h) Reproduced with permission.[229] Copyright 2021, American Chemical Society.

Cu atoms display incomparable advantages.[31] Chen *et al.* calculated that unsaturated Cu sites on massive Al_2O_3 were conducive to the formation of HCOO* and had a positive effect on the production of CH_4 (Fig. 20d and e).[229] Further, monatomic Cu was loaded onto ultra-thin porous Al_2O_3, which achieved a current density of 153.0 mA cm^{-2} and an FE_{CH_4} of 62% at −1.2 V (Fig. 20f–h). Under the coordination of oxygen vacancies, single atom Cu on CeO_2 could reduce CO_2 to CH_4 and C_2H_4 with a total Faraday efficiency of more than 70%.[230] The precise and controllable synthesis of dispersed atomic sites is the key and challenge of catalyst development. For ADMCs, theoretical calculations and machine learning show unique advantages, which are helpful for guiding the experimental design and synthesis of CO_2RR catalysts.

4.2. Alloys

Alloys have become one of the alternative catalysts for CO_2RR due to the advantages that the constituent elements can form a mutual stabilizing mechanism, thus improving the conductivity and providing more active sites. According to the type and content of metal, alloy electrocatalysts can be classified into single-atom alloys, bimetallic/trimetallic alloys and high-entropy alloys.

4.2.1. Single-atom alloys. Single-atom alloys (SAAs) can maximize the use of metal atoms, have uniform active sites, and unique geometrical and electronic structure, which render excellent catalytic performance in electrocatalytic CO_2RR.[231] For example, Zheng *et al.* designed a single-atom Pd-alloyed Cu catalyst (Pd_1Cu) to convert CO_2 to formic *via* single-atom

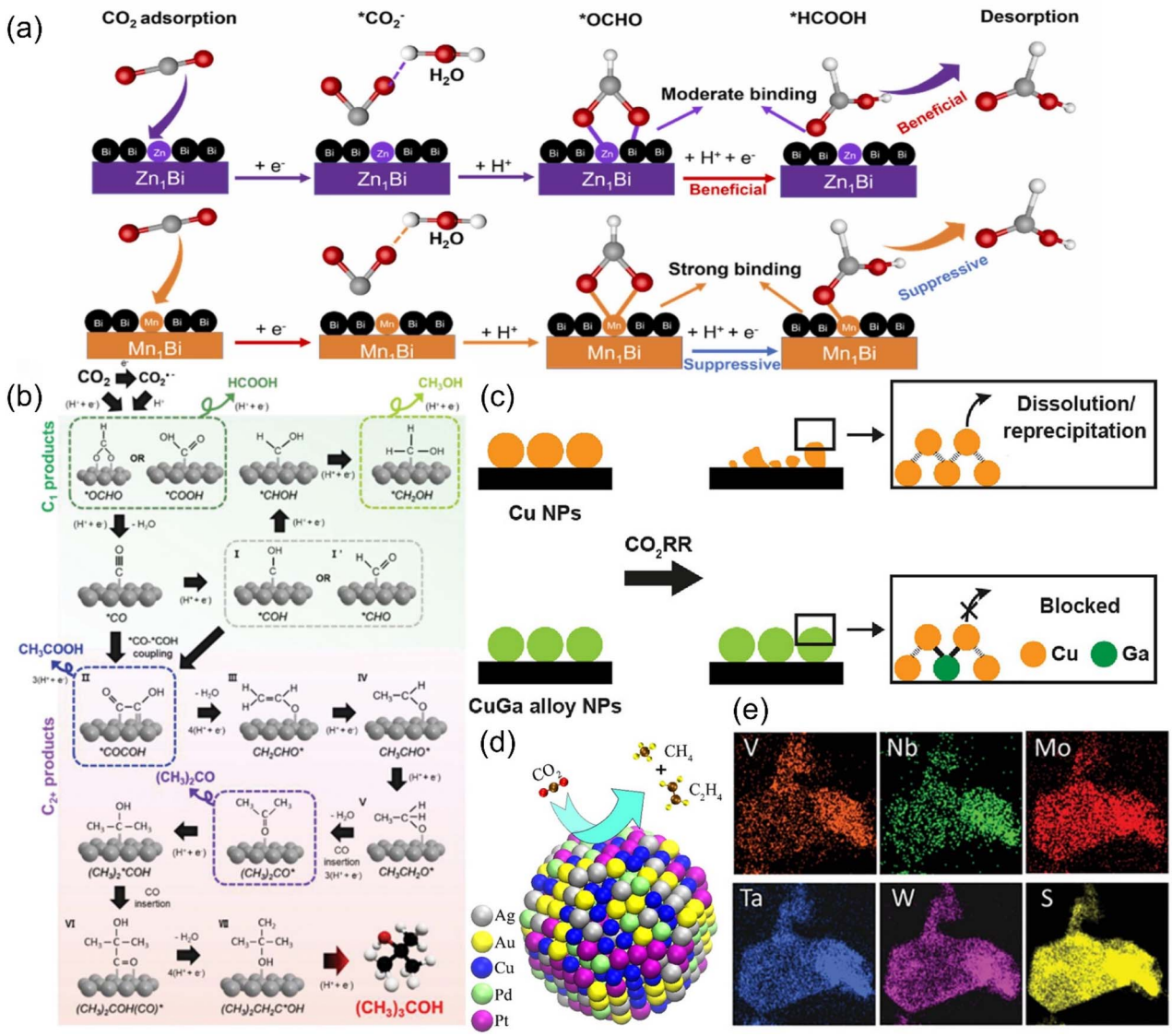

Fig. 21 (a) A proposed reaction mechanism for CO_2R to formate on SAA-Zn_1Bi and SAA-Mn_1Bi. (b) A probable mechanism for CO_2R to $(CH_3)_3COH$. (c) Illustration of the CO_2RR stabilization mechanism on CuGa alloy NPs. (d) Schematic of the catalysis reaction on AuAgPtPdCu. (e) EDS maps of $(MoWVNbTa)S_2$. (a) Reproduced with permission.[233] Copyright 2023, Elsevier Ltd. (b) Reproduced with permission.[236] Copyright 2023, Wiley-VCH GmbH. (c) Reproduced with permission.[237] Copyright 2023, American Chemical Society. (d) Reproduced with permission.[240] Copyright 2020, American Chemical Society. (e) Reproduced with permission.[241] Copyright 2021, Wiley-VCH GmbH.

alloying with a high faradaic efficiency of ~96% at 1 A cm^{-2}.[232] What counts is that isolated Pd atoms were not active sites but rather acted more as modulators to adjust the local geometric and electronic structure of the neighboring Cu sites, making them highly selective and active for formate evolution. Shen *et al.* synthesized Zn single-atom alloyed metallic Bi (SAA-Zn_1Bi), an ideal CO_2RR catalyst screened under the guidance of DFT calculations for the production of formate, by a two-step *in situ* electrochemical reduction strategy (Fig. 21a).[233] Wang *et al.* accelerated the prediction of Cu-based single-atom alloy catalysts for CO_2RR by machine learning.[234] Several SAAs, including PCu, AgCu, GaCu, ZnCu, SnCu, GeCu, InCu and SiCu, were identified as promising CO_2RR catalysts through the high-throughput calculations of 2669 CO adsorption configurations on 43 types of Cu-based SAAs with various surfaces.

4.2.2. Bimetallic/trimetallic alloys. The effective electronic interactions between two/three metals and the special interfacial structure in bimetallic/trimetallic catalysts often make them exhibit better performance.[235] Inspired by the motivation, the increasing attention has been concentrated on the development of bimetallic/trimetallic alloys, showing promising catalytic activity for CO_2RR. For example, Kim *et al.* fabricated Cu_xIr_{1-x} alloy NPs with oxophilic Ir-rich surfaces to convert CO_2 into high value C_4 product *t*-BuOH [$(CH_3)_3COH$] with an FE of 14.8% at a $j_{partial}$ of 0.207 mA cm^{-2}, which showed the best performance toward C_4 production so far.[236] Furthermore, they proposed a probable mechanism of *t*-BuOH formation (Fig. 21b). The strong electronic interactions between Cu and Ir as well as the high pro-oxidative nature of Ir-rich surfaces promoted the generation of C_4, which enhanced the binding strength of the oxygen-bound intermediates. Okatenko *et al.* reported that CuGa alloy NPs containing 17 at% Ga preserved most of their CO_2RR activity for at least 20 h, which was attributed to the higher oxophilicity and lower electronegativity of Ga, reducing the propensity of Cu to oxidize at open-circuit potential (ocp) and enhancing the bond strength in the alloyed nanocatalysts (Fig. 21c).[237] In addition, Chen *et al.* synthesized several $Cu_xZn_yMn_z$ ternary alloy electrocatalysts and tuned the surface coverage of *CO and *H, including Cu_8-ZnMn, Cu_8Zn_6Mn and Cu_8ZnMn_2, by varying the doping amounts of Zn and Mn.[238] In which, the Cu_8ZnMn catalyst presented a high CO_2-to-CH_4 partial current density, while the Cu_8Zn_6Mn catalyst exhibited a high CO_2-to-C_2H_4 partial current density. Meanwhile, they found that the increase in the *H coverage allowed promotion of CH_4 and H_2 formation, while the increase in the *CO coverage facilitated the production of C_2H_4 and CO.

4.2.3. High-entropy alloys. High-entropy alloys (HEAs) have emerged as a novel material in the field of electrocatalysis, showing excellent performance for CO_2RR, which is related to the intrinsic properties such as high entropy effect, lattice distortion, sluggish diffusion and cocktail effect.[239] Nellaiappan *et al.* synthesized AuAgPtPdCu for the conversion of CO_2 into gaseous hydrocarbons (CO, CH_4, C_2H_4, and H_2) with an FE of about 100% (Fig. 21d).[240] Although many elements were present in the catalyst, the electrocatalytic activity was predominantly described by the presence of redox-active Cu metal (Cu^{2+}/Cu^0), and other metals only provided a synergistic effect. Cavin *et al.* predicted four HEAs, $(MoWNbV)S_2$, $(MoWNbTa)S_2$, $(MoWVNbTa)S_2$ and $(MoVNbTa)S_2$, subsequently synthesized the first three of these alloys with approximately equimolar stoichiometries and found that $(MoWVNbTa)S_2$ HEA showed an exceptionally high electrocatalytic performance for CO_2 conversion to CO (Fig. 21e).[241] Besides, Roy *et al.* used screening criteria considering pure Cu (111) surface as a reference catalyst and found 34 active and selective HEA catalysts for CH_3OH formation from the entire CuCoNiZnSn-based data set with the help of contour plots for the adsorption energies of *CO, $*H_2CO$, *H, and *O.[242]

4.3. Metal–organic frameworks

It is well known that porous carbon-based materials with good chemical and thermal stability are favorable catalysts or supports for CO_2 capture.[243,244] Among porous carbon-based materials, MOFs are porous materials with well-defined crystallinity constructed from a diversity of organic linkers and feasible synthesis methods.[245,246] MOFs are superb catalyst templates due to their outstanding physiochemical stability, structure diversity, highly ordered porous structure, uniform pore sizes and environments, high internal surface areas, and functional organic linkers.[247,248] Benefiting from these unique physical and chemical properties, MOF derivatives exhibit the superiorities of higher stability, conductivity, and catalytic activity, which have been widely applied in CO_2RR.

4.3.1. Zinc-based MOFs. Zinc-based MOFs were historically reported to catalyze CO_2-to-CO conversion, and Zn is a promising metal to replace precious metals in CO_2RR. The tuning of peripheral components, such as ligands and heteroatom doping, has been studied in the context of CO_2RR.[202] Al-Attas and colleagues synthesized Zn-based MOFs containing different azolate functional ligands (1,2,4-triazole (Calgary Framework 20, CALF20)) and 2-methylimidazole (zeolitic imidazolate framework-8, ZIF-8) and found that CALF20 showed the highest CO partial current density of 53.2 mA cm^{-2}, with faradaic efficiency of ~94% at −0.97 V (*versus* RHE) and a turnover frequency (TOF) of 1360.8 h^{-1} due to faster charge transfer (Fig. 22a–c).[249] Zinc imidazolate framework-8 (ZIF-8) is a subclass of zinc-based MOF based on zeolite topologies and containing Zn^{2+} and imidazolate ligands as the building units. The CO_2 reduction performance of ZIF-8 can be tuned *via* heteroatom doping, such as N-,[250] Fe-,[251] Co-,[134] and Ni-doping.[202] Qiu and co-workers adopted Fe, N co-doping to enhance the CO_2RR reactivity of ZIF-8.[252] An increase in the FE and current density for CO production from *ca.* 75.0 to 98.8% in a concentrated $KHCO_3$ solution (1 mol L^{-1}) was observed, and the total current densities are more than 3 times higher than those of the less porous ones for electrochemical CO_2 reduction (Fig. 22d and e).

4.3.2. Copper-based MOFs. Cu-based nanomaterials are the most effective electrocatalysts due to their possible production of various hydrocarbon fuels including HCOOH, CO, CH_4, C_2H_4, C_2H_5OH, and even C_3H_7OH.[253] Cu-BTC is a class of Cu-MOF formed by the self-assembly of Cu precursor dissolved in *N*,*N*-

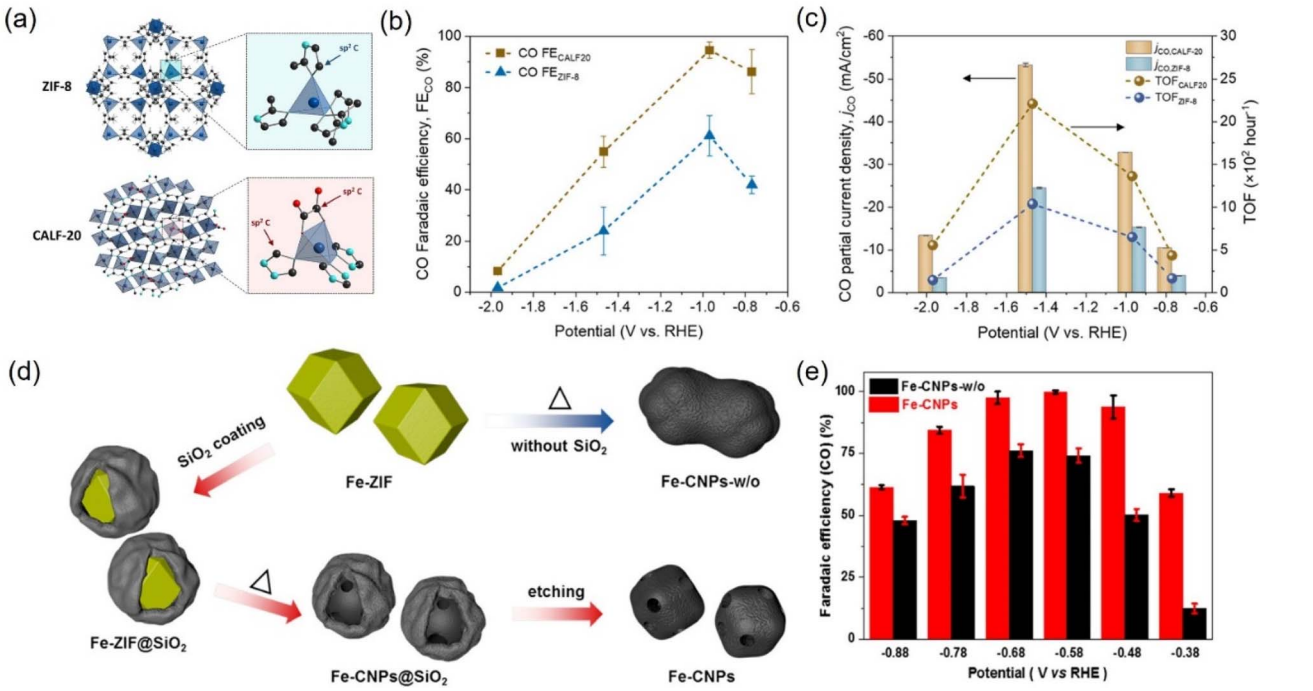

Fig. 22 (a) Schematic illustration of the crystal structure of ZIF-8 and CALF20. (b) FE_{CO} and (c) CO partial current densities and TOF at different applied potentials for CALF20 and ZIF-8 in 1.0 M KOH. (d) Synthetic illustration of Fe-CNPs and Fe-CNPs-w/o. (e) FE_{CO} at different potentials. (a–c) Reproduced with permission.[249] Copyright 2021, American Chemical Society. (d and e) Reproduced with permission.[252] Copyright 2019, American Chemical Society.

dimethylformamide (DMF) with benzene-1,3,5-tricarboxylic acid (H_3BTC). Fang and co-workers used Cu-BTC as a sacrificial template to synthesize a series of Cu-carbon-based catalysts (Cu-pC, Cu_2O-pC, and Cu_2O/Cu-pC) with various valence states and mesoporous structures and found that Cu_2O/CuO-pC with higher oxidation state can effectively enhance the CO_2RR activity.[254] In addition, multi-site tandem electrocatalytic CO_2 reduction can be realized by tuning the geometry of Cu-BTC. Cao *et al.* prepared a series of Cu-based nanoreactors by adjusting the geometrical morphology of MOF precursors. Among them, the cuboctahedron nanoreactor containing Cu-N_4/Cu_2O/Cu multiple active sites exhibited excellent CO_2RR selectivity towards the deep reduction product (80%) at a high current density (Fig. 23a and b).[255] Because Cu edge atoms prefer to adsorb protons in water, single metal Cu tends to show intense activity for the paradoxical reaction (HER) rather than for the CO_2RR.[256] Cu–In bimetallic catalysts were prepared by pyrolyzing Cu–In MOF (Cu–In BTC) for the CO_2RR (Fig. 23c). $Cu_{90}In_{10}$/C exhibits up to 85% selectivity of CO at −0.75 V *versus* RHE, higher than that of 3.1% and 10.8% for Cu/C and In/C, respectively.[257] The alkaline microenvironment during the CO_2RR process rapidly destroys the Cu–O coordination bond of MOF, leading to the rapid aggregation of *in situ*-generated Cu-based nanoclusters and thus leading to the gradual loss of the CO_2RR activity.[258] Meanwhile, Cu–N coordination is more stable than Cu–O coordination in MOFs, which is attributed to the matching between Cu^{2+} as a borderline acid and N-heterocycle as borderline bases.[258] Gu *et al.* prepared highly active Cu/Cu_2O nanoclusters *via in situ* electrochemical reconstruction using Cu–N coordinated MOF $CuPZ_2$ as precursors for the highly selective C_2H_4 synthesis, showing a faradaic efficiency of 70.2 ± 1.7% toward C_2H_4 with a partial current density of 12.38 mA cm^{-2} at −1.03 V *vs.* RHE in the CO_2RR. *In situ* infrared spectroscopy with the observation of *CO*CO and *CO*COH intermediates confirmed the C_2H_4 formation pathway, while *in situ* Raman spectroscopy and HRTEM evidenced that the coexisting Cu_2O and Cu nanoclusters were the active sites (Fig. 23d and e).[258] Besides, Cu-based MOF (MOF-74) was used as the precursor of highly isolated Cu NPs to achieve enhanced CH_4 production in the CO_2RR.[245] Furthermore, Irabien *et al.* tested the ECO_2RR catalytic activity of various Cu-based organic porous materials, including HKUST-1 MOF, CuAdeAce MOF, CuDTA mesoporous metal–organic aerogel (MOA) and CuZnDTA MOA, verifying their ECO_2RR application potential in gas diffusion electrodes (GDEs).[13] Among them, the GDEs constructed by HKUST-1 and CuZnDTA can utilize and convert CO_2 more efficiently into liquid methanol/ethanol products, and the Faraday efficiency of ethanol with high economic value can be as high as 15.9% and 9.9%, respectively, which can be attributed to the unsaturated coordination environment of the porous metal–organic frameworks. Notably, when the conversion rate was normalized to the active metal surface available for each material, the ECO_2RR activity of CuAdeAce was second to none. The donor ligand-constructed paddle-wheel motifs play an important role in stabilizing the square plane coordination geometry around the Cu^{2+} atom, which allows for the generation of open metal sites throughout the porous network that is prone to strong interaction with guest molecules. Since the local structure of the metal–organic porous material is hard to be destroyed, even though the crystallinity of

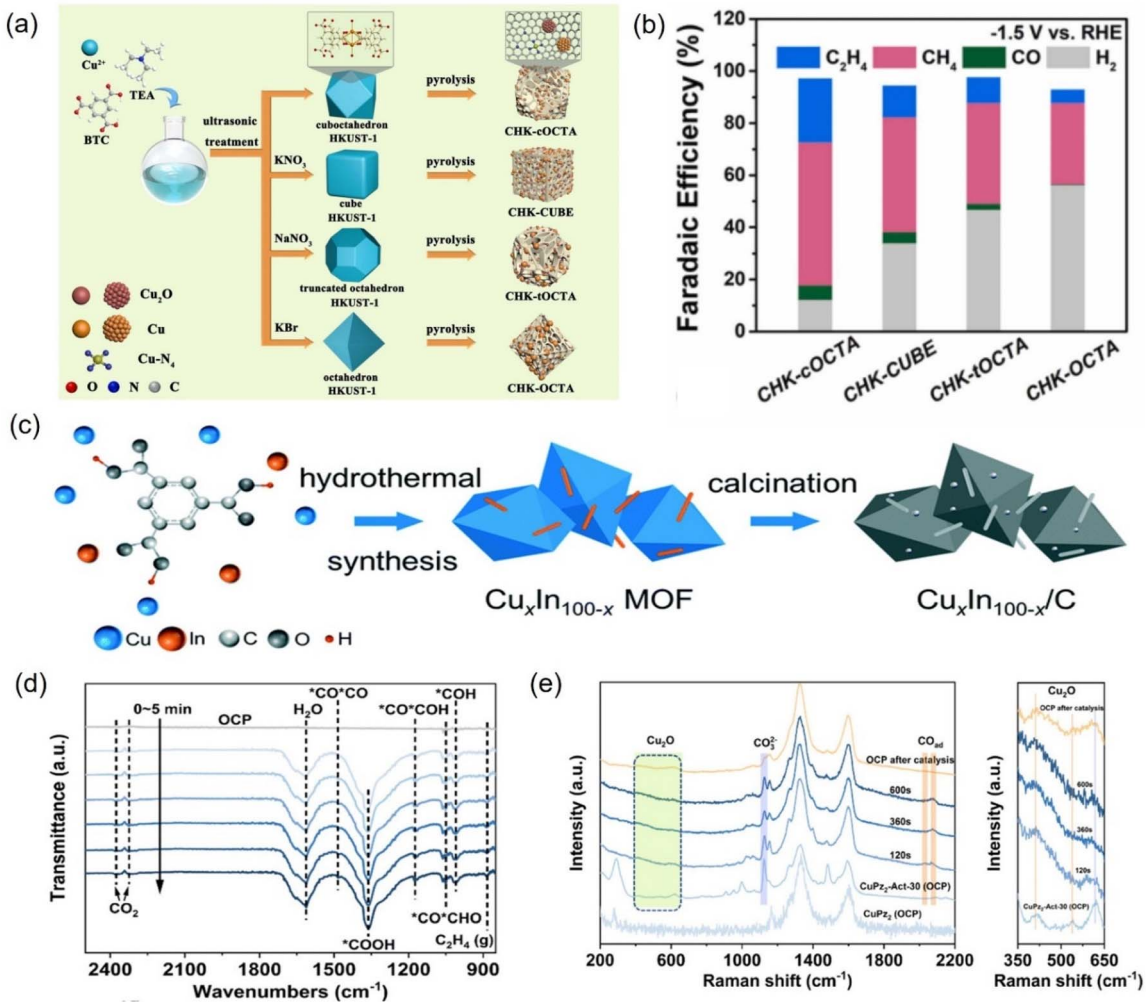

Fig. 23 (a) Illustration of the fabrication of different Cu-based nanoreactors and (b) faradaic efficiency at −1.5 V *vs.* RHE. (c) Synthetic diagram of Cu–In bimetallic catalysts. (d) *In situ* ATR-FTIR spectra of $CuPz_2$-Act-30 collected at −1.03 V *vs.* RHE and (e) *in situ* Raman spectra of $CuPz_2$ (OCP), $CuPz_2$-Act-30 (OCP), and $CuPz_2$-Act-30. (a and b) Reproduced with permission.[255] Copyright 2022, Elsevier. (c) Reproduced with permission.[257] Copyright 2021, the Royal Society of Chemistry. (d and e) Reproduced with permission.[258] Copyright 2022, American Chemical Society.

the material is significantly reduced, HKUST-1 GDE exhibited excellent stability for continuous operation for 17 hours. On this basis, they introduced another metal Bi to synthesize bimetallic MOF materials and tested their ability to convert CO_2 into alcoholic products.[9] Compared with single Cu/Bi-based MOFs, the synergistic effect between Cu and Bi optimizes the electronic structure of the active center and the energy barriers of the key reaction intermediates and promotes the formation of methanol and the C–C coupling step of ethanol. After a series of comparisons, it was found that the ratio of Cu and Bi loadings in the MOFs and the current density of the system significantly control the selectivity of the generated alcoholic products, which, above or below the optimal values of both, will weaken the catalytic performance of ECO_2RR.

4.3.3. Other metal-based MOFs. There are some reports on cobalt-, iron-, zirconium-, bismuth- and nickel-based MOFs-derived catalysts. A series of MOFs with different morphologies (abbreviated as Ni-MOF-525) with zirconia clusters as nodes and nickel porphyrin complexes as bridging ligands were synthesized by Zheng *et al.*[259] Ni SACs in an H-cell possessed an urchin-like hierarchical structure with internal voids, with rapid and highly selective electroreduction of CO_2 to CO ($FE_{CO} = 98\%$) even at a current density as high as 200 mA cm^{-2}. Fe-N-C catalyst derived from Fe-MOF was found to exhibit high Faraday efficiency (86.8%) for CO products at an overpotential of 496 mV and excellent long-term stability due to the good inheritance of the Fe-MOF precursor.[260] Recently, MOF thin films as electrocatalytically active units have been shown to be functional for electrochemical CO_2 reduction.[261] Hupp *et al.* embedded copper nanoparticles into a zirconium-MOF film (NU-1000). The catalyst was obtained by installing Cu(II) clusters in NU-1000 films by a solvothermal deposition method, followed by the electrochemical reduction of Cu(II) to metallic copper, which exhibited good electrocatalytic activity.[262] Li *et al.* reported the synthesis of Bi SAs/NC catalysts using Bi-MOFs as the precursors, which exhibited high intrinsic CO_2 reduction

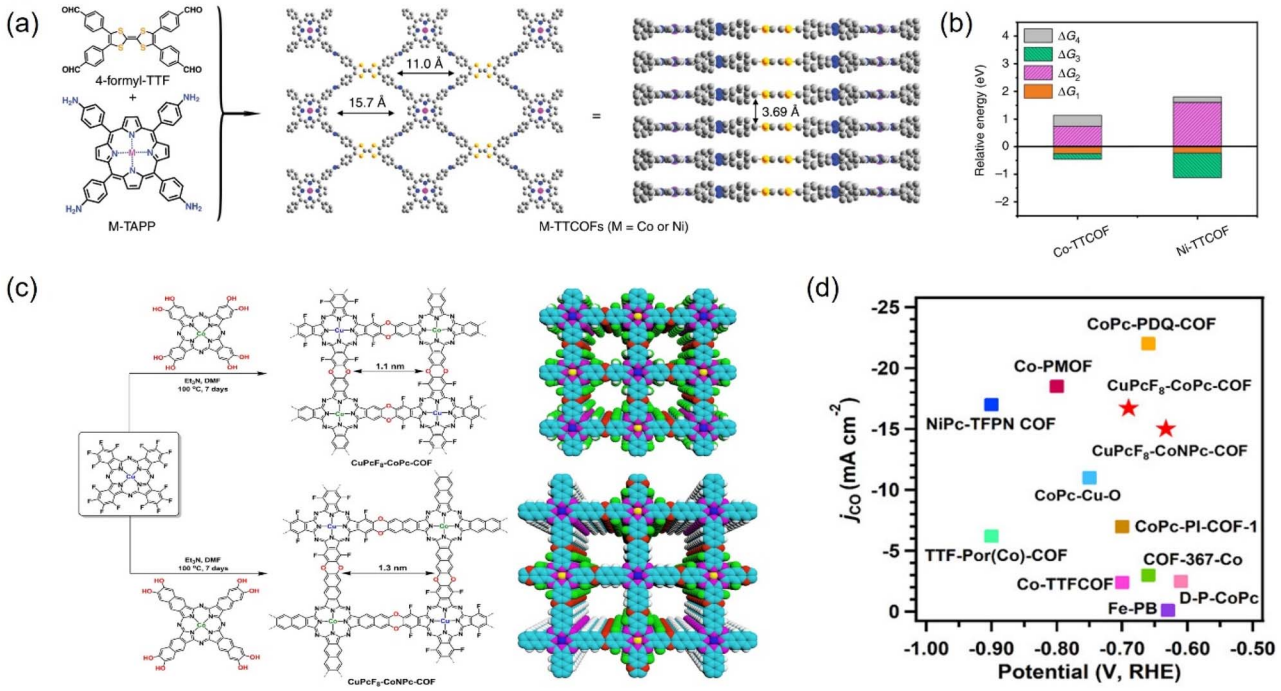

Fig. 24 (a) The structure of M-TTCOFs obtained through the condensation of 4-formyl-TTF and M-TAPP. (b) Comparison of the relative energy of each elementary reaction (ΔG_1, ΔG_2, and ΔG_3 represent the free energy of *CO_2, *COOH, and *CO formation, respectively, and ΔG_4 stands for the free energy of CO desorption process) in the electrocatalytic CO_2RR for M-TTCOFs (M = Co or Ni). (c) Schematic representation for the synthesis of $CuPcF_8$-CoPc-COF and $CuPcF_8$-CoNPc-CO. (d) Comparison of j_{CO}. (a and b) Reproduced with permission.[265] Copyright 2020, Springer Nature. (c and d) Reproduced with permission.[266] Copyright 2021, American Chemical Society.

activity for CO conversion, with a high FE_{CO} of 97% and high turnover frequency of 5535 h^{-1} at a low overpotential of 0.39 V.[82]

4.4. Covalent organic frameworks

COFs are reticulated crystalline solids with a periodic structure consisting of molecular units connected by functional organic ligands.[202,263,264] COFs, as promising alternative materials for electrocatalytic CO_2RR, are mainly attributed to more exposed surface area and active sites, tunable structure, and the possibility of modifying a wide range of metal types (*e.g.*, Co, Cu, and Ni) into their structure to confer the COFs with tunable catalytic centers.[265] These materials allow the integration of various organic building blocks into two-dimensional (2D) or three-dimensional (3D) mesh networks. Over the past decade, hundreds of COFs have been developed and used in a variety of applications, including gas adsorption, multiphase catalysis, photonics, photoemission, and wastewater treatment.[266]

4.4.1. Two-dimensional COFs. Two-dimensional (2D) COFs exhibit polymeric sheet-like structures composed of well-ordered polygons, endowing them with impressive stability for device application.[267] In CO_2RR electrocatalysis, optimized 2D frameworks electrocatalysts would be an ideal choice to control the catalytic activity, selectivity and efficiency in a single catalytic system with high performance toward the target products.[268] Lan *et al.* prepared a series of stable and highly crystalline metalloporphyrin tetrathiafulvalene-based COFs (M-TTCOFs), in which Co-TTCOF was able to selectively convert CO_2 to CO, with an FE_{CO} of 91.3% at −0.7 V. Moreover, DFT calculations showed that Co-TTCOF displayed the lowest activation energy (Fig. 24a and b).[265] However, the poor electrical conductivity of monometallic COFs limits their electrocatalytic performance.[269] Huang *et al.* synthesized two novel ultra-stable bimetallic polyphthalocyanine-based 2D COFs, $CuPcF_8$-CoPc-COF and $CuPcF_8$-CoNPc-COF by rational design using dioxin as the bond.[266] The structure of the metal phthalocyanine units in overlapping stacking mode provides a high-speed pathway for electron transfer. Notably, the $CuPcF_8$-CoNPc-COF possessed a Faraday efficiency of 97%, which is superior to most COF-based electrocatalysts (Fig. 24c and d). In addition, constructing interlayer hydrogen bonds in 2D COFs can enhance the interlayer interactions of COFs, thereby improving the electrical conductivity, thermal stability, and chemical stability.[270] Three new 2D polyimide-conjugated phthalocyanine COFs, namely, NiPc-OH-COF, NiPc-OMe-COF, and NiPc-H-COF, were synthesized by Jiang *et al.* Owing to the introduction of additional interlayer hydrogen-bonding interactions between the O–H of the 4-phenylene diols and the hydroxyl "O" atoms of the neighboring layers, the NiPc-OH-COFs showed enhanced chemical stability, which could be stabilized for 2 weeks even under a 1 M aqueous sodium hydroxide solution.[271]

4.4.2. Three-dimensional COFs. The active sites are usually hidden in the layers of 2D COF materials due to the face-to-face lamellar stacking that limits their proximity to the electrolyte and CO_2, thus reducing the concentration of surface active sites in the electrocatalytic process.[272] 3D COFs could maximize active electrocatalytic sites by spatially separating molecular

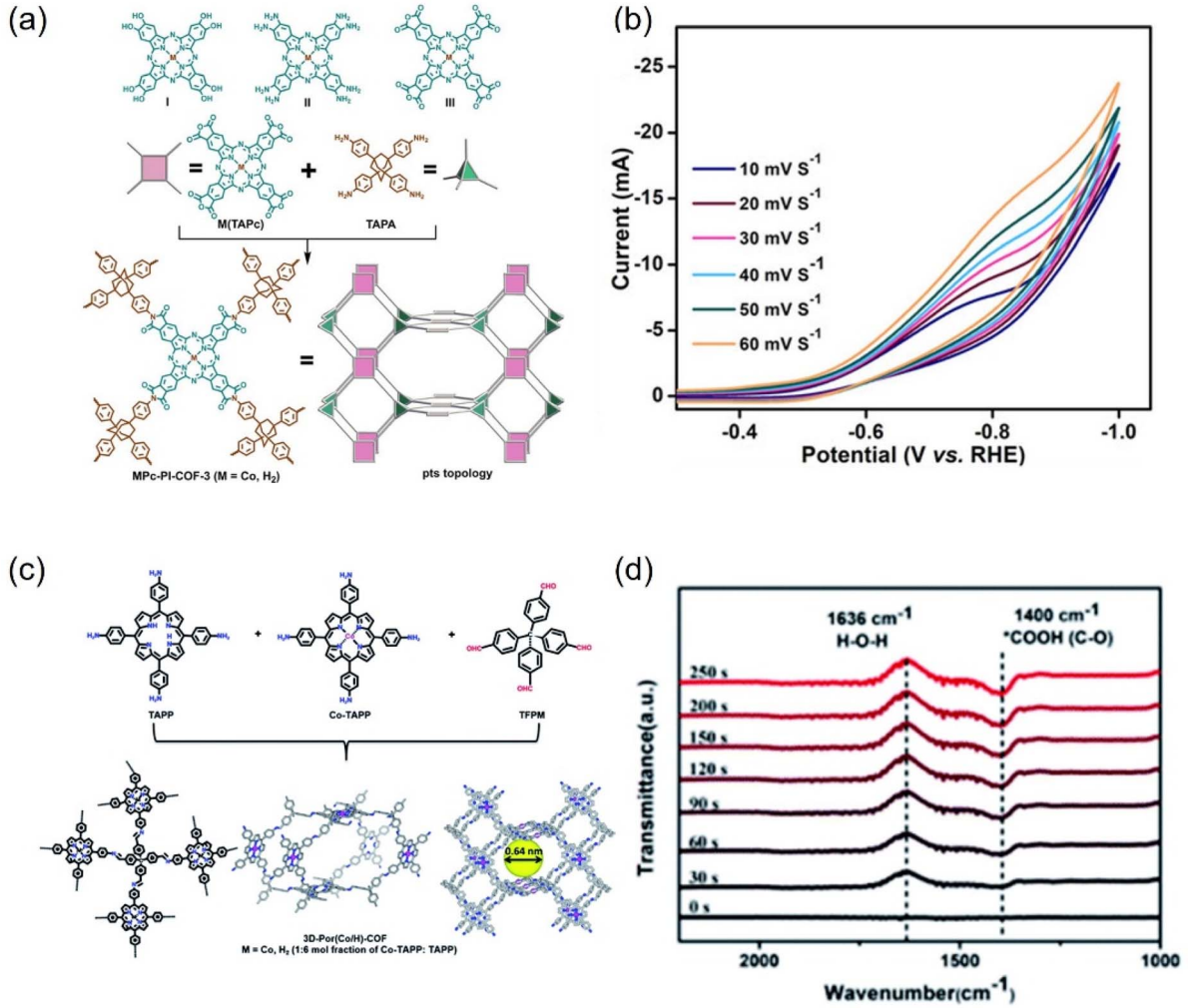

Fig. 25 (a) Synthesis of MPc-PI-COF-3 (M = Co^{II} or H_2) and (b) scan rate dependence of cyclic voltammetry response of CoPc-PI-COF-3. (c) Schematic representation of the synthesis of 3D-Por(Co/H)-COF and the simulated network. (d) *In situ* ATR-IR of 3D-Por(Co/H)-COF at −0.9 V. (a and b) Reproduced with permission.[274] Copyright 2022, John Wiley and Sons Ltd. (c and d) Reproduced with permission.[275] Copyright 2022, Royal Society of Chemistry.

building blocks.[273] Jiang *et al.* constructed 3D phthalocyanine (Pc) polyimide (PI) COFs (M-Pc-PI-COFs-3 (M = Co^{II}, H_2)), in which the unique 3D porous structure of CoPc-PI-COF-3 ensured an electrochemical surface concentration of up to 183 nmol cm^{-2} at the electrode, *i.e.*, 32.7% of the metal phthalocyanine substituent as the active center (Fig. 25a and b).[274] Besides, a porous 3D cobalt porphyrinic COF, denoted as 3D-Por(Co/H)-COF, was synthesized by Cao and coworkers, which exhibited high activity for CO_2RR with a CO faradaic efficiency of 92.4% at −0.6 V *versus* RHE.[275] ATR-IR spectra showed that the formation of the *COOH intermediate was the rate-determining step for the CO_2RR (Fig. 25c and d).

5. Challenges and perspectives

Metal-based electrocatalysts have been widely studied for the CO_2RR due to their controllable composition and structure, excellent chemical stability and clear catalytically active sites. In this review, we summarize the basic research and current research progress of catalyst structure regulation and carrier selection involved in CO_2RR. Although significant progress has been made in electrocatalytic CO_2RR, the actual related research is still in its infancy. As a promising way to close the carbon cycle and generate value-added products, CO_2RR is attracting more and more attention. However, CO_2RR is extremely sensitive to the reaction environment, which makes it difficult to accurately grasp the reaction process. Physical and chemical changes may occur during the catalytic process as well as morphological evolution such as surface recombination and roughening on the catalyst surface. In order to obtain efficient target products, there are still several crucial challenges to be overcome.

(1) Compared with the easily available C_1 product, the reduction reactions of C_2 and C_3 products remain to be further studied. For two-electron products, high Faraday efficiency can be achieved at a given potential, but the overpotential is still

unsatisfactory compared with the theoretical value. Hence, improving the Faraday efficiency of multi-carbon products is the main direction of future research. Commercially, the reduction products are required to have high Faraday efficiency (>90%) and current density (>200 mA cm^{-2}). Increasing the selectivity for high-value products remains a major challenge and there is still a huge room for progress.

It is necessary, on the one hand, to develop the catalytic activity and product possibilities of more metal elements, and, on the other hand, to improve the specific Faraday efficiency of metals known to produce multi-carbon products. Besides, most of the reported electrocatalysts are usually designed as powders, which may lead to the serious agglomeration of the material, thereby reducing the utilization of active sites. Furthermore, excessive pursuit of performance improvement while ignoring the cost considerations is also not conducive to practical application. Therefore, people are eager to minimize the use of expensive precursors and surfactants and simplify the synthesis processes to obtain catalytic systems with both low cost and high efficiency. On the basis of clarifying the active sites by experiments and theoretical calculations, the core of the solution needs to be considered from the perspective of the catalyst itself. Optimization strategies including heteroatom doping, defect engineering, and morphology design are useful for assisting electrocatalysts in achieving economical products with higher purity. Conceptualizing ingenious strategies is the golden key to meet the selectivity requirements in practical application. For example, as the material size is optimized for further reduction, the density of the active site along with the specific surface area will continue to expand, which can promote mass transport and improve the kinetic activity. Furthermore, the selective introduction of defects such as vacancies and grain boundaries can effectively contribute to the desired outcome. In addition, the hydrophilicity and hydrophobicity of the catalyst can be adjusted to optimize the binding energy of the intermediate, thus affecting the competitive relationship between CO_2RR and HER.

(2) Compared with the success achieved in the catalytic activity of ECO_2RR, the breakthrough in the stability has been more dismal. To date, almost all the reported materials have a lifetime of less than 1000 hours.[14] The peak achievement is that the operating time for CO and formic acid can reach 3800 and 2400 hours, respectively.[276,277] However, these existing catalysts are far from meeting the commercial threshold of more than 50 000 hours for the low-temperature operation of ECO_2RR.[278] Therefore, on the road to the commercialization of ECO_2RR, meeting the most troublesome difficulties of long-term stable operation is the core technical problem to be solved urgently. There are many factors that lead to the instability of electrocatalysis. For example, small perturbations in the electrochemical microenvironment may increase the difficulty of species mass transfer, thereby limiting the diffusion and adsorption of CO_2 molecules. In this regard, it is necessary to optimize the entire electrolysis system and alleviate flooding and carbonate problems. In addition, the active sites will undergo isomeric collapse as the ECO_2RR continues, resulting in the inability of electrons to be quickly transferred, and the key intermediate species cannot be effectively adsorbed, which has a devastating effect on both the stability and activity. The key to solving this thorny problem is to create more thermodynamic and kinetic barriers to atomic migration. Enhancing the bond strength of lattice atomic bonds to chemically improve the degree of bonding and wrapping canning materials to physically prevent atomic diffusion are effective strategies to avoid surface reconstruction, which can be achieved by ligand protection, doping/alloying, interface construction and protective layer encapsulation. Notably, the reasonable manipulation of operating conditions such as pulse electrolysis can also uniquely extend the durability of the material by repairing the active center and adjusting the interfacial chemistry. Specifically, pulse operation prolongs the ECO_2RR process by inhibiting carbonate deposition, removing surface toxins/bubbles, and recovering active phases.

(3) In addition to the optimization of the catalyst itself, it is particularly critical to design a more suitable CO_2RR electrolytic cell.[279] The setting of electrolytic cells will have a profound impact on the overall performance of ECO_2RR.[280] With the improvement of this technical field, it is particularly critical to significantly reduce the overpotential of CO_2RR in the electrolytic cell. Through the analysis and comparison of various types of electrolytic cells, in most of the current studies, the three reactors of H-type electrolytic cell,[281] flow type electrolytic cell[282] and membrane electrode electrolytic cell[283] are widely used. The H-type electrolytic cell is separated from the left and right chambers by an ion-exchange membrane.[284] The separation of electrolyte and cathode reaction gas can be achieved by exchange. However, the solubility of CO_2 in the environment containing water electrolyte is relatively low. Therefore, in the H-type reactor, the mass transfer process is greatly restricted. Due to the large interfacial tension between water and air, the gas cannot enter the cathode chamber through this area, thus affecting the electrolysis reaction. In addition, continuous carbon dioxide blowing may lead to an increase in the pH value of the electrolyte, which is more detrimental to the performance of the H-type battery. In order to solve the problems existing in the H-type electrolytic cell, researchers have designed a flow electrolytic cell for CO_2RR. Compared with the H-type electrolytic cell, the flow cell adds a gas chamber, and the gas diffusion layer (GDL) is used to separate the cathode electrolyte and the CO_2 gas. The CO_2 gas can directly pass through the GDL and react on the surface of the catalyst. The flow cell also has the ability to utilize alkaline electrolytes, which is beneficial because it can inhibit HER in a high pH environment, thereby improving the performance of CO_2RR. From the perspective of commercialization, membrane electrode electrolyzers are considered to be the most suitable equipment for commercial applications. However, some organic products may cause damage to solid electrolytes and ion-exchange membranes during long-term use, thereby reducing their durability. Therefore, for a variety of different products, we need to optimize and adjust the system of solid electrolyte electrolyzers in a timely manner. The careful design of electrodes and electrolytic reactors plays a vital role in achieving catalytic activity with industrial application value.

(4) DFT calculations can explore the electronic structure and directly identify the active sites at the atomic level. It is a favorable weapon for reasonably analyzing the reaction

mechanism and predicting the catalytic steps and has an indispensable inspiration and guidance for experimental preparation.[285] For ECO_2RR, the intrinsic properties of CO_2 molecules are variable, the types of intermediates of CO_2RR are multifarious, and the effects of solvation and ion on CO_2RR at the solid–liquid interface are relatively complex. Theoretical calculations are increasingly being relied upon to reveal the mechanism of the tedious reaction steps and to screen for more optimized material compositions and structures. Due to the escalating difficulty, the theoretical insights of CO_2RR are far less comprehensive and profound than other electrocatalytic reactions such as OER, HER, and ORR, and there is still a huge unknown space to be exploited. Typically, the calculation of the hydrogen electrode (CHE) is modeled under the assumption that the catalyst is charge-neutral to calculate the energy barrier of each intermediate step. However, ECO_2RR usually occurs at the gas–liquid–solid interface with a constant electrode potential. The surface of the catalyst is charged and is balanced by electron exchange with the electrode, rather than without the electrode potential, which is a non-negligible influence factor in ECO_2RR. For example, the basic step energy barrier of the proton–electron transfer of ECO_2RR to CO on Cu (100) is profoundly affected by the electrode potential, and their change trend is opposite. In this regard, Wang *et al.* regulated the electrode potential of the system by introducing anions (Cl^-) and cations (Na^+) and detect their effects using constrained molecular dynamic (MD) sampling and thermodynamic integration.[286] They also elucidated the mechanism of electron transfer-proton transfer (ET-PT) decoupling and hydrogen bond-assisted CO_2 activation, indicating that the efficient adsorption and activation of CO_2 are closely related to the electron transfer of active sites, demonstrating that the electrode potential is the key to achieving efficient capture of CO_2. In addition, the hydrogen bond network between the water solvent molecules interacts strongly with the key species adsorbed on the catalyst surface, and this solvent effect almost determines the stability of ECO_2RR intermediates. In summary, it is of great significance to construct a clear model of aqueous solution system and introduce the consideration of electrode potential into the calculation simultaneously. In the future, the influencing factors included in the theoretical research on ECO_2RR need to be more comprehensive to fit the actual reaction in the experiment as much as possible.

Looking ahead, ECO_2RR research will mainly focus on the system design of the electrolyzer and the optimization and evaluation of electrochemical performance, especially in the design of the reactor, the nature of the electrode, electrolyte, ion exchange membrane, voltage, current density, energy efficiency and the service life of the electrolyzer. These research results will provide a strong impetus and guidance for the commercial application of ECO_2RR.

Author contributions

All of the authors contributed to the literature search, writing and editing of this review.

Conflicts of interest

There are no conflicts to declare.

Acknowledgements

This work was supported by the National Natural Science Foundation of China (No. 22075099), and the Natural Science Foundation of Jilin Province (No. 20220101051JC).

Notes and references

1 S. Gao, Y. Zhu, M. Umar, B. Kchouri and A. Safi, *Technol. Forecast. Soc.*, 2024, **201**, 123177.
2 R. Huang, *Sci. Total Environ.*, 2024, **913**, 169775.
3 J. Rogelj and R. D. Lamboll, *Commun. Earth Environ.*, 2024, **5**, 35.
4 Z.-C. Zeng, T. Pongetti, S. Newman, T. Oda, K. Gurney, P. I. Palmer, Y. L. Yung and S. P. Sander, *Nat. Commun.*, 2023, **14**, 5353.
5 M. Umar, S. Farid and M. A. Naeem, *Energy*, 2022, **240**, 122702.
6 Y. Y. Birdja, E. Pérez-Gallent, M. C. Figueiredo, A. J. Göttle, F. Calle-Vallejo and M. T. M. Koper, *Nat. Energy*, 2019, **4**, 732–745.
7 A. D. Handoko, F. Wei, Jenndy, B. S. Yeo and Z. W. Seh, *Nat. Catal.*, 2018, **1**, 922–934.
8 D. Gao, R. M. Arán-Ais, H. S. Jeon and B. Roldan Cuenya, *Nat. Catal.*, 2019, **2**, 198–210.
9 J. Albo, M. Perfecto-Irigaray, G. Beobide and A. Irabien, *J. CO_2 Util.*, 2019, **33**, 157–165.
10 Z. Wang, Y. Zhou, P. Qiu, C. Xia, W. Fang, J. Jin, L. Huang, P. Deng, Y. Su, R. Crespo-Otero, X. Tian, B. You, W. Guo, D. Di Tommaso, Y. Pang, S. Ding and B. Y. Xia, *Adv. Mater.*, 2023, **35**, 2303052.
11 Y. Zou and S. Wang, *Adv. Sci.*, 2021, **8**, 2003579.
12 X. Zhang, Z. Zhang, H. Li, R. Gao, M. Xiao, J. Zhu, M. Feng and Z. Chen, *Adv. Energy Mater.*, 2022, **12**, 2201461.
13 J. Albo, D. Vallejo, G. Beobide, O. Castillo, P. Castaño and A. Irabien, *ChemSusChem*, 2016, **10**, 1100–1109.
14 W. Lai, Y. Qiao, Y. Wang and H. Huang, *Adv. Mater.*, 2023, **35**, 2306288.
15 H. Wu, A. Singh-Morgan, K. Qi, Z. Zeng, V. Mougel and D. Voiry, *ACS Catal.*, 2023, **13**, 5375–5396.
16 S. Kumar De, D.-I. Won, J. Kim and D. H. Kim, *Chem. Soc. Rev.*, 2023, **52**, 5744–5802.
17 I. Merino-Garcia, J. Albo, J. Solla-Gullón, V. Montiel and A. Irabien, *J. CO_2 Util.*, 2019, **31**, 135–142.
18 B. Kumar, M. Llorente, J. Froehlich, T. Dang, A. Sathrum and C. P. Kubiak, *Annu. Rev. Phys. Chem.*, 2012, **63**, 541–569.
19 X. Chang, T. Wang and J. Gong, *Energy Environ. Sci.*, 2016, **9**, 2177–2196.
20 I. Merino-Garcia, J. Albo and A. Irabien, *Nanotechnology*, 2018, **29**, 014001.
21 L. Zhang, Z. J. Zhao and J. Gong, *Angew. Chem., Int. Ed.*, 2017, **56**, 11326–11353.

22 L. R. L. Ting and B. S. Yeo, *Curr. Opin. Electrochem.*, 2018, **8**, 126–134.
23 C. Shi, K. Chan, J. S. Yoo and J. K. Nørskov, *Org. Process Res. Dev.*, 2016, **20**, 1424–1430.
24 S. Back, M. S. Yeom and Y. Jung, *ACS Catal.*, 2015, **5**, 5089–5096.
25 A. Dutta, A. Kuzume, M. Rahaman, S. Vesztergom and P. Broekmann, *ACS Catal.*, 2015, **5**, 7498–7502.
26 W. Zhang, Y. Hu, L. Ma, G. Zhu, Y. Wang, X. Xue, R. Chen, S. Yang and Z. Jin, *Adv. Sci.*, 2017, **5**, 1700275.
27 G. Marcandalli, M. C. O. Monteiro, A. Goyal and M. T. M. Koper, *Acc. Chem. Res.*, 2022, **55**, 1900–1911.
28 J. Y. Yang, T. A. Kerr, X. S. Wang and J. M. Barlow, *J. Am. Chem. Soc.*, 2020, **142**, 19438–19445.
29 X. Zhou, J. Shan, L. Chen, B. Y. Xia, T. Ling, J. Duan, Y. Jiao, Y. Zheng and S.-Z. Qiao, *J. Am. Chem. Soc.*, 2022, **144**, 2079–2084.
30 L. Deng, Z. Wang, X. Jiang, J. Xu, Z. Zhou, X. Li, Z. You, M. Ding, T. Shishido, X. Liu and M. Xu, *Appl. Catal., B*, 2023, **322**, 122124.
31 H. Yang, Y. Wu, G. Li, Q. Lin, Q. Hu, Q. Zhang, J. Liu and C. He, *J. Am. Chem. Soc.*, 2019, **141**, 12717–12723.
32 R. Kortlever, J. Shen, K. J. P. Schouten, F. Calle-Vallejo and M. T. M. Koper, *J. Phys. Chem. Lett.*, 2015, **6**, 4073–4082.
33 M. F. Baruch, J. E. Pander, J. L. White and A. B. Bocarsly, *ACS Catal.*, 2015, **5**, 3148–3156.
34 X. Min and M. W. Kanan, *J. Am. Chem. Soc.*, 2015, **137**, 4701–4708.
35 H. A. Hansen, J. B. Varley, A. A. Peterson and J. K. Nørskov, *J. Phys. Chem. Lett.*, 2013, **4**, 388–392.
36 C. Chen, J. F. Khosrowabadi Kotyk and S. W. Sheehan, *Chem*, 2018, **4**, 2571–2586.
37 L. Wang, W. Chen, D. Zhang, Y. Du, R. Amal, S. Qiao, J. Wu and Z. Yin, *Chem. Soc. Rev.*, 2019, **48**, 5310–5349.
38 A. A. Peterson, F. Abild-Pedersen, F. Studt, J. Rossmeisl and J. K. Nørskov, *Energy Environ. Sci.*, 2010, **3**, 1311–1315.
39 Y. Lin, T. Wang, L. Zhang, G. Zhang, L. Li, Q. Chang, Z. Pang, H. Gao, K. Huang, P. Zhang, Z.-J. Zhao, C. Pei and J. Gong, *Nat. Commun.*, 2023, **14**, 3575.
40 C.-T. Dinh, T. Burdyny, Md G. Kibria, S. Ali, C. M. Gabardo, F. Pelayo García de Arquer, A. Kiani, J. P. Edwards, P. De Luna, O. S. Bushuyev, C. Zou, R. Quintero-Bermudez, Y. Pang, D. Sinton and E. H. Sargent, *Science*, 2018, **360**, 783–787.
41 X. Nie, M. R. Esopi, M. J. Janik and A. Asthagiri, *Angew. Chem., Int. Ed.*, 2013, **52**, 2459–2462.
42 K. D. Yang, C. W. Lee, K. Jin, S. W. Im and K. T. Nam, *J. Phys. Chem. Lett.*, 2017, **8**, 538–545.
43 E. Pérez-Gallent, M. C. Figueiredo, F. Calle-Vallejo and M. T. M. Koper, *Angew. Chem., Int. Ed.*, 2017, **56**, 3621–3624.
44 Y. Hori, R. Takahashi, Y. Yoshinami and A. Murata, *J. Phys. Chem. B*, 1997, **101**, 7075–7081.
45 Z. Sun, T. Ma, H. Tao, Q. Fan and B. Han, *Chem*, 2017, **3**, 560–587.
46 X. Li, M. Qin, X. Wu, X. Lv, J. Wang, Y. Wang and H. B. Wu, *Small*, 2023, **19**, 2302530.
47 J. Zhang, Y. Wang, Z. Li, S. Xia, R. Cai, L. Ma, T. Zhang, J. Ackley, S. Yang, Y. Wu and J. Wu, *Adv. Sci.*, 2022, **9**, 2200454.
48 T. T. H. Hoang, S. Verma, S. Ma, T. T. Fister, J. Timoshenko, A. I. Frenkel, P. J. A. Kenis and A. A. Gewirth, *J. Am. Chem. Soc.*, 2018, **140**, 5791–5797.
49 P. Wang, H. Yang, C. Tang, Y. Wu, Y. Zheng, T. Cheng, K. Davey, X. Huang and S.-Z. Qiao, *Nat. Commun.*, 2022, **13**, 3754.
50 C. Peng, X. Zhu, Z. Xu, S. Yan, L. Y. Chang, Z. Wang, J. Zhang, M. Chen, T. K. Sham, Y. Li and G. Zheng, *Small*, 2021, **18**, 2106433.
51 C. Peng, G. Luo, Z. Xu, S. Yan, J. Zhang, M. Chen, L. Qian, W. Wei, Q. Han and G. Zheng, *Adv. Mater.*, 2021, **33**, 2103150.
52 D. Zhong, Z. J. Zhao, Q. Zhao, D. Cheng, B. Liu, G. Zhang, W. Deng, H. Dong, L. Zhang, J. Li, J. Li and J. Gong, *Angew. Chem., Int. Ed.*, 2021, **60**, 4879–4885.
53 H. Li, T. Liu, P. Wei, L. Lin, D. Gao, G. Wang and X. Bao, *Angew. Chem., Int. Ed.*, 2021, **60**, 14329–14333.
54 J. J. Lv, M. Jouny, W. Luc, W. Zhu, J. J. Zhu and F. Jiao, *Adv. Mater.*, 2018, **30**, 1803111.
55 P. Wang, H. Yang, Y. Xu, X. Huang, J. Wang, M. Zhong, T. Cheng and Q. Shao, *ACS Nano*, 2020, **15**, 1039–1047.
56 X. Wang, K. Klingan, M. Klingenhof, T. Möller, J. Ferreira de Araújo, I. Martens, A. Bagger, S. Jiang, J. Rossmeisl, H. Dau and P. Strasser, *Nat. Commun.*, 2021, **12**, 794.
57 Q. Zhu, Y. Hu, H. Chen, C. Meng, Y. Shang, C. Hao, S. Wei, Z. Wang, X. Lu and S. Liu, *Nanoscale*, 2023, **15**, 2106–2113.
58 J. Wu, S. Ma, J. Sun, J. I. Gold, C. Tiwary, B. Kim, L. Zhu, N. Chopra, I. N. Odeh, R. Vajtai, A. Z. Yu, R. Luo, J. Lou, G. Ding, P. J. A. Kenis and P. M. Ajayan, *Nat. Commun.*, 2016, **7**, 13869.
59 J. Yuan, W.-Y. Zhi, L. Liu, M.-P. Yang, H. Wang and J.-X. Lu, *Electrochim. Acta*, 2018, **282**, 694–701.
60 X. Zou, M. Liu, J. Wu, P. M. Ajayan, J. Li, B. Liu and B. I. Yakobson, *ACS Catal.*, 2017, **7**, 6245–6250.
61 C. Liang, B. Kim, S. Yang, Y. L. Yang Liu, C. Francisco Woellner, Z. Li, R. Vajtai, W. Yang, J. Wu, P. J. A. Kenis and P. M. Ajayan, *J. Mater. Chem. A*, 2018, **6**, 10313–10319.
62 M. Yu, P. F. Sui, X. Z. Fu, J. L. Luo and S. Liu, *Adv. Energy Mater.*, 2022, **13**, 2203191.
63 L. Xiao, X. Bai, J. Han, T. Tang, S. Chen, H. Qi, C. Hou, F. Bai, Z. Wang and J. Guan, *Nano Res.*, 2023, **17**, 2429–2437.
64 L. Xiao, L. Qi, J. Sun, A. Husile, S. Zhang, Z. Wang and J. Guan, *Nano Energy*, 2024, **120**, 109155.
65 S. Chen, T. Zhang, J. Han, H. Qi, S. Jiao, C. Hou and J. Guan, *Nano Res. Energy*, 2024, **3**, e9120106.
66 Y. Huang, F. Rehman, M. Tamtaji, X. Li, Y. Huang, T. Zhang and Z. Luo, *J. Mater. Chem. A*, 2022, **10**, 5813–5834.
67 T. Tang, Z. Wang and J. Guan, *Acta Phys.–Chim. Sin.*, 2022, 2208033.
68 T. Tang, Z. Wang and J. Guan, *Adv. Funct. Mater.*, 2022, **32**, 2111504.
69 X. Bai, Y. Wang, J. Han, X. Niu and J. Guan, *Appl. Catal., B*, 2023, **337**, 122966.

70 T. Tang, Z. Wang and J. Guan, *Coord. Chem. Rev.*, 2023, **492**, 215288.
71 J. Han and J. Guan, *Nano Res.*, 2023, **16**, 1913–1966.
72 T. Zhang, J. Sun and J. Guan, *Nano Res.*, 2023, **16**, 8684–8711.
73 L. Li, X. Li, Y. Sun and Y. Xie, *Chem. Soc. Rev.*, 2022, **51**, 1234–1252.
74 D. Gao, W. Li, H. Wang, G. Wang and R. Cai, *Trans. Tianjin Univ.*, 2022, **28**, 245–264.
75 H. Yao, M.-Y. Wang, C. Yue, B. Feng, W. Ji, C. Qian, S. Wang, S. Zhang and X. Ma, *Trans. Tianjin Univ.*, 2023, **29**, 254–274.
76 T. Tang, J. Han, Z. Wang, X. Niu and J. Guan, *Nano Res.*, 2023, **17**, 3794–3800.
77 J. Zhang, W. Cai, F. X. Hu, H. Yang and B. Liu, *Chem. Sci.*, 2021, **12**, 6800–6819.
78 J. Ma, C. Liu, M. Bai, Z. Fu, P. Zhao, Y. Gao, M. Zhao, Y. He, H. Xiao and J. Jia, *Mol. Catal.*, 2023, **551**, 113632.
79 M. Li, H. Wang, W. Luo, P. C. Sherrell, J. Chen and J. Yang, *Adv. Mater.*, 2020, **32**, 2001848.
80 W. Zheng, F. Chen, Q. Zeng, Z. Li, B. Yang, L. Lei, Q. Zhang, F. He, X. Wu and Y. Hou, *Nano-Micro Lett.*, 2020, **12**, 108.
81 G. Qu, K. Wei, K. Pan, J. Qin, J. Lv, J. Li and P. Ning, *Nanoscale*, 2023, **15**, 3666–3692.
82 E. Zhang, T. Wang, K. Yu, J. Liu, W. Chen, A. Li, H. Rong, R. Lin, S. Ji, X. Zheng, Y. Wang, L. Zheng, C. Chen, D. Wang, J. Zhang and Y. Li, *J. Am. Chem. Soc.*, 2019, **141**, 16569–16573.
83 W. Guo, X. Tan, J. Bi, L. Xu, D. Yang, C. Chen, Q. Zhu, J. Ma, A. Tayal, J. Ma, Y. Huang, X. Sun, S. Liu and B. Han, *J. Am. Chem. Soc.*, 2021, **143**, 6877–6885.
84 Z. Jiang, T. Wang, J. Pei, H. Shang, D. Zhou, H. Li, J. Dong, Y. Wang, R. Cao, Z. Zhuang, W. Chen, D. Wang, J. Zhang and Y. Li, *Energy Environ. Sci.*, 2020, **13**, 2856–2863.
85 H. Xie, T. Wang, J. Liang, Q. Li and S. Sun, *Nano Today*, 2018, **21**, 41–54.
86 D. Gao, T. Liu, G. Wang and X. Bao, *ACS Energy Lett.*, 2021, **6**, 713–727.
87 Y. Jiang, Y. Wang, R. Chen, Y. Li and C. Li, *Energy Fuels*, 2023, **37**, 17951–17965.
88 A. Vasileff, C. Xu, Y. Jiao, Y. Zheng and S.-Z. Qiao, *Chem*, 2018, **4**, 1809–1831.
89 W. Ren, X. Tan, W. Yang, C. Jia, S. Xu, K. Wang, S. C. Smith and C. Zhao, *Angew. Chem., Int. Ed.*, 2019, **58**, 6972–6976.
90 W. Zhu, L. Zhang, S. Liu, A. Li, X. Yuan, C. Hu, G. Zhang, W. Deng, K. Zang, J. Luo, Y. Zhu, M. Gu, Z. J. Zhao and J. Gong, *Angew. Chem., Int. Ed.*, 2020, **59**, 12664–12668.
91 C. Jia, K. Dastafkan and C. Zhao, *Curr. Opin. Electrochem.*, 2022, **31**, 100854.
92 Z. Wu, Y. Zhao, W. Jin, B. Jia, J. Wang and T. Ma, *Adv. Funct. Mater.*, 2020, **31**, 2009070.
93 Y. Li, M. Wen, Y. Wang, G. Tian, C. Wang and J. Zhao, *Angew. Chem., Int. Ed.*, 2020, **60**, 910–916.
94 Z. Niu, X. Gao, S. Lou, N. Wen, J. Zhao, Z. Zhang, Z. Ding, R. Yuan, W. Dai and J. Long, *ACS Catal.*, 2023, **13**, 2998–3006.
95 Z. Li, A. Cao, Q. Zheng, Y. Fu, T. Wang, K. T. Arul, J. L. Chen, B. Yang, N. M. Adli, L. Lei, C. L. Dong, J. Xiao, G. Wu and Y. Hou, *Adv. Mater.*, 2020, **33**, 2005113.
96 H. Wang, N. Wen, Y. Wang, X. Jiao, Y. Xia and D. Chen, *Adv. Funct. Mater.*, 2023, **33**, 2303473.
97 B. Jia, L. Li, C. Xue, J. Kang, L. M. Liu, T. Guo, Z. Wang, Q. Huang and S. Guo, *Adv. Mater.*, 2023, **35**, 2305587.
98 Y. He, H. Rao, K. Song, J. Li, Y. Yu, Y. Lou, C. Li, Y. Han, Z. Shi and S. Feng, *Adv. Funct. Mater.*, 2019, **29**, 1905153.
99 X. Rong, H. J. Wang, X. L. Lu, R. Si and T. B. Lu, *Angew. Chem., Int. Ed.*, 2019, **59**, 1961–1965.
100 R. Chen, X. Zu, J. Zhu, Y. Zhao, Y. Li, Z. Hu, S. Wang, M. Fan, S. Zhu, H. Zhang, B. Ye, Y. Sun and Y. Xie, *Adv. Mater.*, 2024, 2314209, DOI: **10.1002/adma.202314209**.
101 W. Ding, S. Yuan, Y. Yang, X. Li and M. Luo, *J. Mater. Chem. A*, 2023, **11**, 23653–23682.
102 H. Yu, F. Chen, X. Li, H. Huang, Q. Zhang, S. Su, K. Wang, E. Mao, B. Mei, G. Mul, T. Ma and Y. Zhang, *Nat. Commun.*, 2021, **12**, 4594.
103 Y. Liang, C. Wu, S. Meng, Z. Lu, R. Zhao, H. Wang, Z. Liu and J. Wang, *ACS Appl. Mater. Interfaces*, 2023, **15**, 30262–30271.
104 S. Gao, Z. Sun, W. Liu, X. Jiao, X. Zu, Q. Hu, Y. Sun, T. Yao, W. Zhang, S. Wei and Y. Xie, *Nat. Commun.*, 2017, **8**, 14503.
105 Z. Geng, X. Kong, W. Chen, H. Su, Y. Liu, F. Cai, G. Wang and J. Zeng, *Angew. Chem., Int. Ed.*, 2018, **57**, 6054–6059.
106 B. Qin, Y. Li, H. Wang, G. Yang, Y. Cao, H. Yu, Q. Zhang, H. Liang and F. Peng, *Nano Energy*, 2019, **60**, 43–51.
107 L. Cheng, Y. Li, A. Chen, Y. Zhu and C. Li, *Chem. Commun.*, 2020, **56**, 563–566.
108 D. Yan, C. Xia, W. Zhang, Q. Hu, C. He, B. Y. Xia and S. Wang, *Adv. Energy Mater.*, 2022, **12**, 2202317.
109 D. Qu, X. Peng, Y. Mi, H. Bao, S. Zhao, X. Liu and J. Luo, *Nanoscale*, 2020, **12**, 17191–17195.
110 H. Liang, A. N. Gandi, D. H. Anjum, X. Wang, U. Schwingenschlögl and H. N. Alshareef, *Nano Lett.*, 2016, **16**, 7718–7725.
111 S. Dou, L. Tao, R. Wang, S. El Hankari, R. Chen and S. Wang, *Adv. Mater.*, 2018, **30**, 1705850.
112 S. Dou, L. Tao, J. Huo, S. Wang and L. Dai, *Energy Environ. Sci.*, 2016, **9**, 1320–1326.
113 C. Kong, F. Zhang, Y. Wang and J. Huang, *J. Alloys Compd.*, 2021, **876**, 160165.
114 H. Bi, S. Zhu, Y. Liang, H. Jiang, Z. Li, S. Wu, H. Wei, C. Chang and Z. Cui, *Chem. Eng. J.*, 2022, **442**, 136146.
115 J. Zhang, Y. Zhao, X. Guo, C. Chen, C.-L. Dong, R.-S. Liu, C.-P. Han, Y. Li, Y. Gogotsi and G. Wang, *Nat. Catal.*, 2018, **1**, 985–992.
116 F. Wang, W. Zhang, H. Wan, C. Li, W. An, X. Sheng, X. Liang, X. Wang, Y. Ren, X. Zheng, D. Lv and Y. Qin, *Chin. Chem. Lett.*, 2022, **33**, 2259–2269.
117 S. S. A. Shah, M. Sufyan Javed, T. Najam, C. Molochas, N. A. Khan, M. A. Nazir, M. Xu, P. Tsiakaras and S.-J. Bao, *Coord. Chem. Rev.*, 2022, **471**, 214716.
118 Y.-H. Luo, L.-Z. Dong, J. Liu, S.-L. Li and Y.-Q. Lan, *Coord. Chem. Rev.*, 2019, **390**, 86–126.

119 R. Reske, M. Duca, M. Oezaslan, K. J. P. Schouten, M. T. M. Koper and P. Strasser, *J. Phys. Chem. Lett.*, 2013, **4**, 2410–2413.
120 Z. Chang, S. Huo, W. Zhang, J. Fang and H. Wang, *J. Phys. Chem. C*, 2017, **121**, 11368–11379.
121 H. Xie, S. Chen, F. Ma, J. Liang, Z. Miao, T. Wang, H.-L. Wang, Y. Huang and Q. Li, *ACS Appl. Mater. Interfaces*, 2018, **10**, 36996–37004.
122 Q. Li, J. Fu, W. Zhu, Z. Chen, B. Shen, L. Wu, Z. Xi, T. Wang, G. Lu, J.-j. Zhu and S. Sun, *J. Am. Chem. Soc.*, 2017, **139**, 4290–4293.
123 J. Hao, S. Xie, Q. Huang, Z. Ding, H. Sheng, C. Zhang and J. Yao, *CCS Chem.*, 2023, **5**, 2046–2058.
124 M. He, W. An, Y. Wang, Y. Men and S. Liu, *Small*, 2021, **17**, 2104445.
125 Y. Xie, N. Liu, X. Li, X. Qin, X. Luo, Y. Wang and X. Chen, *J. Phys. Chem. C*, 2021, **125**, 21460–21470.
126 Z. Wang, R. Shi, S. Lu, K. Zhang and T. Zhang, *Rep. Prog. Phys.*, 2022, **85**, 026501.
127 Z. L. Wang, J. Choi, M. Xu, X. Hao, H. Zhang, Z. Jiang, M. Zuo, J. Kim, W. Zhou, X. Meng, Q. Yu, Z. Sun, S. Wei, J. Ye, G. G. Wallace, D. L. Officer and Y. Yamauchi, *ChemSusChem*, 2020, **13**, 929–937.
128 X. Zhao and Y. Liu, *J. Am. Chem. Soc.*, 2020, **142**, 5773–5777.
129 Q. Qu, S. Ji, Y. Chen, D. Wang and Y. Li, *Chem. Sci.*, 2021, **12**, 4201–4215.
130 Md Delowar Hossain, Y. Huang, T. H. Yu, W. A. Goddard and Z. Luo, *Nat. Commun.*, 2020, **11**, 2256.
131 Y. Pan, R. Lin, Y. Chen, S. Liu, W. Zhu, X. Cao, W. Chen, K. Wu, W.-C. Cheong, Y. Wang, L. Zheng, J. Luo, Y. Lin, Y. Liu, C. Liu, J. Li, Q. Lu, X. Chen, D. Wang, Q. Peng, C. Chen and Y. Li, *J. Am. Chem. Soc.*, 2018, **140**, 4218–4221.
132 H. Zhang, J. Li, S. Xi, Y. Du, X. Hai, J. Wang, H. Xu, G. Wu, J. Zhang, J. Lu and J. Wang, *Angew. Chem., Int. Ed.*, 2019, **58**, 14871–14876.
133 C. Yan, H. Li, Y. Ye, H. Wu, F. Cai, R. Si, J. Xiao, S. Miao, S. Xie, F. Yang, Y. Li, G. Wang and X. Bao, *Energy Environ. Sci.*, 2018, **11**, 1204–1210.
134 X. Wang, Z. Chen, X. Zhao, T. Yao, W. Chen, R. You, C. Zhao, G. Wu, J. Wang, W. Huang, J. Yang, X. Hong, S. Wei, Y. Wu and Y. Li, *Angew. Chem., Int. Ed.*, 2018, **57**, 1944–1948.
135 W. Zheng, J. Yang, H. Chen, Y. Hou, Q. Wang, M. Gu, F. He, Y. Xia, Z. Xia, Z. Li, B. Yang, L. Lei, C. Yuan, Q. He, M. Qiu and X. Feng, *Adv. Funct. Mater.*, 2019, **30**, 1907658.
136 J. Yang, Z. Qiu, C. Zhao, W. Wei, W. Chen, Z. Li, Y. Qu, J. Dong, J. Luo, Z. Li and Y. Wu, *Angew. Chem., Int. Ed.*, 2018, **57**, 14095–14100.
137 J. Feng, H. Gao, L. Zheng, Z. Chen, S. Zeng, C. Jiang, H. Dong, L. Liu, S. Zhang and X. Zhang, *Nat. Commun.*, 2020, **11**, 4341.
138 E. Jung, H. Shin, B.-H. Lee, V. Efremov, S. Lee, H. S. Lee, J. Kim, W. Hooch Antink, S. Park, K.-S. Lee, S.-P. Cho, J. S. Yoo, Y.-E. Sung and T. Hyeon, *Nat. Mater.*, 2020, **19**, 436–442.
139 Y. Cai, J. Fu, Y. Zhou, Y.-C. Chang, Q. Min, J.-J. Zhu, Y. Lin and W. Zhu, *Nat. Commun.*, 2021, **12**, 586.
140 H. Kim, D. Shin, W. Yang, D. H. Won, H.-S. Oh, M. W. Chung, D. Jeong, S. H. Kim, K. H. Chae, J. Y. Ryu, J. Lee, S. J. Cho, J. Seo, H. Kim and C. H. Choi, *J. Am. Chem. Soc.*, 2021, **143**, 925–933.
141 S. Cao, S. Wei, X. Wei, S. Zhou, H. Chen, Y. Hu, Z. Wang, S. Liu, W. Guo and X. Lu, *Small*, 2021, **17**, 2100949.
142 Y. Chen, R. Gao, S. Ji, H. Li, K. Tang, P. Jiang, H. Hu, Z. Zhang, H. Hao, Q. Qu, X. Liang, W. Chen, J. Dong, D. Wang and Y. Li, *Angew. Chem., Int. Ed.*, 2020, **60**, 3212–3221.
143 Y. Wu, C. Chen, X. Yan, X. Sun, Q. Zhu, P. Li, Y. Li, S. Liu, J. Ma, Y. Huang and B. Han, *Angew. Chem., Int. Ed.*, 2021, **60**, 20803–20810.
144 J. Wang, X. Huang, S. Xi, H. Xu and X. Wang, *Angew. Chem., Int. Ed.*, 2020, **59**, 19162–19167.
145 X. Wang, Y. Pan, H. Ning, H. Wang, D. Guo, W. Wang, Z. Yang, Q. Zhao, B. Zhang, L. Zheng, J. Zhang and M. Wu, *Appl. Catal., B*, 2020, **266**, 118630.
146 K. K. Patra, S. Park, H. Song, B. Kim, W. Kim and J. Oh, *ACS Appl. Energy Mater.*, 2020, **3**, 11343–11349.
147 Y. Zhou, F. Che, M. Liu, C. Zou, Z. Liang, P. De Luna, H. Yuan, J. Li, Z. Wang, H. Xie, H. Li, P. Chen, E. Bladt, R. Quintero-Bermudez, T.-K. Sham, S. Bals, J. Hofkens, D. Sinton, G. Chen and E. H. Sargent, *Nat. Chem.*, 2018, **10**, 974–980.
148 J. Gui, L. Li, B. Yu, D. Wang, B. Yang, Q. Gu, Y. Zhao, Y. Zhu and Y. Zhang, *ACS Appl. Mater. Interfaces*, 2023, **15**, 25516–25523.
149 W. Rong, H. Zou, W. Zang, S. Xi, S. Wei, B. Long, J. Hu, Y. Ji and L. Duan, *Angew. Chem., Int. Ed.*, 2021, **60**, 466–472.
150 A. Guan, Z. Chen, Y. Quan, C. Peng, Z. Wang, T.-K. Sham, C. Yang, Y. Ji, L. Qian, X. Xu and G. Zheng, *ACS Energy Lett.*, 2020, **5**, 1044–1053.
151 J. Dong, Y. Liu, J. Pei, H. Li, S. Ji, L. Shi, Y. Zhang, C. Li, C. Tang, J. Liao, S. Xu, H. Zhang, Q. Li and S. Zhao, *Nat. Commun.*, 2023, **14**, 6849.
152 Z.-Q. Liang, T.-T. Zhuang, A. Seifitokaldani, J. Li, C.-W. Huang, C.-S. Tan, Y. Li, P. De Luna, C. T. Dinh, Y. Hu, Q. Xiao, P.-L. Hsieh, Y. Wang, F. Li, R. Quintero-Bermudez, Y. Zhou, P. Chen, Y. Pang, S.-C. Lo, L.-J. Chen, H. Tan, Z. Xu, S. Zhao, D. Sinton and E. H. Sargent, *Nat. Commun.*, 2018, **9**, 3828.
153 C. Peng, G. Luo, Z. Xu, S. Yan, J. Zhang, M. Chen, L. Qian, W. Wei, Q. Han and G. Zheng, *Adv. Mater.*, 2021, **33**, 2103150.
154 C. A. Downes, N. J. Libretto, A. E. Harman-Ware, R. M. Happs, D. A. Ruddy, F. G. Baddour, J. R. Ferrell III, S. E. Habas and J. A. Schaidle, *ACS Appl. Energy Mater.*, 2020, **3**, 10435–10446.
155 H. Chen, Z. Wang, X. Wei, S. Liu, P. Guo, P. Han, H. Wang, J. Zhang, X. Lu and B. Wei, *Appl. Surf. Sci.*, 2021, **544**, 148965.
156 X. Kong, C. Wang, H. Zheng, Z. Geng, J. Bao and J. Zeng, *Sci. China: Chem.*, 2021, **64**, 1096–1102.
157 Y. Lum and J. W. Ager, *Angew. Chem., Int. Ed.*, 2018, **57**, 551–554.

158 A. M. Asiri, J. Gao, S. B. Khan, K. A. Alamry, H. M. Marwani, M. S. J. Khan, W. A. Adeosun, S. M. Zakeeruddin, D. Ren and M. Grätzel, *J. Phys. Chem. Lett.*, 2022, **13**, 345–351.
159 C. Peng, G. Luo, J. Zhang, M. Chen, Z. Wang, T.-K. Sham, L. Zhang, Y. Li and G. Zheng, *Nat. Commun.*, 2021, **12**, 1580.
160 T.-T. Zhuang, Z.-Q. Liang, A. Seifitokaldani, Y. Li, P. De Luna, T. Burdyny, F. Che, F. Meng, Y. Min, R. Quintero-Bermudez, C. T. Dinh, Y. Pang, M. Zhong, B. Zhang, J. Li, P.-N. Chen, X.-L. Zheng, H. Liang, W.-N. Ge, B.-J. Ye, D. Sinton, S.-H. Yu and E. H. Sargent, *Nat. Catal.*, 2018, **1**, 421–428.
161 S. Li, H. Duan, J. Yu, C. Qiu, R. Yu, Y. Chen, Y. Fang, X. Cai and S. Yang, *ACS Catal.*, 2022, **12**, 9074–9082.
162 J. Liu, P. Li, J. Bi, Y. Wang, Q. Zhu, X. Sun, J. Zhang, Z. Liu and B. Han, *Chin. J. Chem.*, 2023, **41**, 1443–1449.
163 X. Su, Z. Jiang, J. Zhou, H. Liu, D. Zhou, H. Shang, X. Ni, Z. Peng, F. Yang, W. Chen, Z. Qi, D. Wang and Y. Wang, *Nat. Commun.*, 2022, **13**, 1322.
164 D. Karapinar, N. T. Huan, N. Ranjbar Sahraie, J. Li, D. Wakerley, N. Touati, S. Zanna, D. Taverna, L. H. Galvão Tizei, A. Zitolo, F. Jaouen, V. Mougel and M. Fontecave, *Angew. Chem., Int. Ed.*, 2019, **58**, 15098–15103.
165 H. Wang, X. Bi, Y. Yan, Y. Zhao, Z. Yang, H. Ning and M. Wu, *Adv. Funct. Mater.*, 2023, **33**, 2214946.
166 D. Yang, Q. Zhu, C. Chen, H. Liu, Z. Liu, Z. Zhao, X. Zhang, S. Liu and B. Han, *Nat. Commun.*, 2019, **10**, 677.
167 J. Duan, T. Liu, Y. Zhao, R. Yang, Y. Zhao, W. Wang, Y. Liu, H. Li, Y. Li and T. Zhai, *Nat. Commun.*, 2022, **13**, 2039.
168 A. Saxena, W. Liyanage, J. Masud, S. Kapila and M. Nath, *J. Mater. Chem. A*, 2021, **9**, 7150–7161.
169 S. Das, S. Senapati, G. K. Pradhan, S. Varadharajanperumal and R. Naik, *ACS Appl. Nano Mater.*, 2023, **6**, 5298–5312.
170 Z. Gu, N. Yang, P. Han, M. Kuang, B. Mei, Z. Jiang, J. Zhong, L. Li and G. Zheng, *Small Methods*, 2019, **3**, 1800449.
171 K. Jiang, Y. Huang, G. Zeng, F. M. Toma, W. A. Goddard III and A. T. Bell, *ACS Energy Lett.*, 2020, **5**, 1206–1214.
172 M. Li, Y. Ma, J. Chen, R. Lawrence, W. Luo, M. Sacchi, W. Jiang and J. Yang, *Angew. Chem., Int. Ed.*, 2021, **60**, 11487–11493.
173 S. Lee, D. Kim and J. Lee, *Angew. Chem., Int. Ed.*, 2015, **54**, 14701–14705.
174 T. Kim and G. T. R. Palmore, *Nat. Commun.*, 2020, **11**, 3622.
175 H. Mistry, A. S. Varela, C. S. Bonifacio, I. Zegkinoglou, I. Sinev, Y.-W. Choi, K. Kisslinger, E. A. Stach, J. C. Yang, P. Strasser and B. R. Cuenya, *Nat. Commun.*, 2016, **7**, 12123.
176 J. Fu, H. Bao, Y. Liu, Y. Mi, Y. Qiu, L. Zhuo, X. Liu and J. Luo, *Small*, 2020, **16**, 1905825.
177 X. Rong, H.-J. Wang, X.-L. Lu, R. Si and T.-B. Lu, *Angew. Chem., Int. Ed.*, 2020, **59**, 1961–1965.
178 X. Yang, P. Deng, D. Liu, S. Zhao, D. Li, H. Wu, Y. Ma, B. Y. Xia, M. Li, C. Xiao and S. Ding, *J. Mater. Chem. A*, 2020, **8**, 2472–2480.
179 Y. Ma, M. Chen, H. Geng, H. Dong, P. Wu, X. Li, G. Guan and T. Wang, *Adv. Funct. Mater.*, 2020, **30**, 2000561.
180 J. Zhang, R. Yin, Q. Shao, T. Zhu and X. Huang, *Angew. Chem., Int. Ed.*, 2019, **58**, 5609–5613.
181 T. Gao, A. Kumar, Z. Shang, X. Duan, H. Wang, S. Wang, S. Ji, D. Yan, L. Luo, W. Liu and X. Sun, *Chin. Chem. Lett.*, 2019, **30**, 2274–2278.
182 L. Cheng, Y. Li, A. Chen, Y. Zhu and C. Li, *Chem. Commun.*, 2020, **56**, 563–566.
183 S. B. Varandili, J. Huang, E. Oveisi, G. L. De Gregorio, M. Mensi, M. Strach, J. Vavra, C. Gadiyar, A. Bhowmik and R. Buonsanti, *ACS Catal.*, 2019, **9**, 5035–5046.
184 W. Zhu, L. Zhang, P. Yang, C. Hu, H. Dong, Z.-J. Zhao, R. Mu and J. Gong, *ACS Energy Lett.*, 2018, **3**, 2144–2149.
185 X. Ren, X. Zhang, X. Cao and Q. Wang, *J. CO_2 Util.*, 2020, **38**, 125–131.
186 D. Wu, G. Huo, W. Chen, X.-Z. Fu and J.-L. Luo, *Appl. Catal., B*, 2020, **271**, 118957.
187 H. He, K. Liu, K. Liang, A. Mustapha, Z. Wang, L. Wu, C. Yang, L. Deng, S. Guo and Y.-N. Liu, *J. Catal.*, 2020, **385**, 246–254.
188 A. Yoon, J. Poon, P. Grosse, S. W. Chee and B. R. Cuenya, *J. Mater. Chem. A*, 2022, **10**, 14041–14050.
189 H. Li, T. Liu, P. Wei, L. Lin, D. Gao, G. Wang and X. Bao, *Angew. Chem., Int. Ed.*, 2021, **60**, 14329–14333.
190 R. Cai, M. Sun, J. Ren, M. Ju, X. Long, B. Huang and S. Yang, *Chem. Sci.*, 2021, **12**, 15382–15388.
191 P. Li, J. Bi, J. Liu, Q. Zhu, C. Chen, X. Sun, J. Zhang and B. Han, *Nat. Commun.*, 2022, **13**, 1965.
192 X. Tan, C. Yu, C. Zhao, H. Huang, X. Yao, X. Han, W. Guo, S. Cui, H. Huang and J. Qiu, *ACS Appl. Mater. Interfaces*, 2019, **11**, 9904–9910.
193 Q. Zhu, X. Sun, D. Yang, J. Ma, X. Kang, L. Zheng, J. Zhang, Z. Wu and B. Han, *Nat. Commun.*, 2019, **10**, 3851.
194 S. Lee, G. Park and J. Lee, *ACS Catal.*, 2017, **7**, 8594–8604.
195 J. Wu, F. G. Risalvato, S. Ma and X.-D. Zhou, *J. Mater. Chem. A*, 2014, **2**, 1647–1651.
196 W. Zhang, Q. Qin, L. Dai, R. Qin, X. Zhao, X. Chen, D. Ou, J. Chen, T. T. Chuong, B. Wu and N. Zheng, *Angew. Chem., Int. Ed.*, 2018, **57**, 9475–9479.
197 S. Huo, Z. Weng, Z. Wu, Y. Zhong, Y. Wu, J. Fang and H. Wang, *ACS Appl. Mater. Interfaces*, 2017, **9**, 28519–28526.
198 K. Wang, D. Liu, P. Deng, L. Liu, S. Lu, Z. Sun, Y. Ma, Y. Wang, M. Li, B. Y. Xia, C. Xiao and S. Ding, *Nano Energy*, 2019, **64**, 103954.
199 X. Bai, J. Han, S. Chen, X. Niu and J. Guan, *Chin. J. Catal.*, 2023, **54**, 212–219.
200 X. Bai, J. Han, X. Niu and J. Guan, *Nano Res.*, 2023, **16**, 10796–10802.
201 Q. Wang, K. Liu, J. Fu, C. Cai, H. Li, Y. Long, S. Chen, B. Liu, H. Li, W. Li, X. Qiu, N. Zhang, J. Hu, H. Pan and M. Liu, *Angew. Chem., Int. Ed.*, 2021, **60**, 25241–25245.
202 C. Zhao, X. Dai, T. Yao, W. Chen, X. Wang, J. Wang, J. Yang, S. Wei, Y. Wu and Y. Li, *J. Am. Chem. Soc.*, 2017, **139**, 8078–8081.
203 Y. Zhang, L. Jiao, W. Yang, C. Xie and H.-L. Jiang, *Angew. Chem., Int. Ed.*, 2021, **60**, 7607–7611.
204 X. Li, S. Xi, L. Sun, S. Dou, Z. Huang, T. Su and X. Wang, *Adv. Sci.*, 2020, **7**, 2001545.
205 J. Gu, C.-S. Hsu, L. Bai, H. M. Chen and X. Hu, *Science*, 2019, **364**, 1091–1094.

206 H. B. Yang, S.-F. Hung, S. Liu, K. Yuan, S. Miao, L. Zhang, X. Huang, H.-Y. Wang, W. Cai, R. Chen, J. Gao, X. Yang, W. Chen, Y. Huang, H. M. Chen, C. M. Li, T. Zhang and B. Liu, *Nat. Energy*, 2018, **3**, 140–147.
207 X. Chen, D.-D. Ma, B. Chen, K. Zhang, R. Zou, X.-T. Wu and Q.-L. Zhu, *Appl. Catal., B*, 2020, **267**, 118720.
208 F. Yang, P. Song, X. Liu, B. Mei, W. Xing, Z. Jiang, L. Gu and W. Xu, *Angew. Chem., Int. Ed.*, 2018, **57**, 12303–12307.
209 J. Liu, X. Kong, L. Zheng, X. Guo, X. Liu and J. Shui, *ACS Nano*, 2020, **14**, 1093–1101.
210 T. Tang, Y. Wang, J. Han, Q. Zhang, X. Bai, X. Niu, Z. Wang and J. Guan, *Chin. J. Catal.*, 2023, **46**, 48–55.
211 J. Han and J. Guan, *Chin. J. Catal.*, 2023, **47**, 1–31.
212 T. Tang, Z. Duan, D. Baimanov, X. Bai, X. Liu, L. Wang, Z. Wang and J. Guan, *Nano Res.*, 2023, **16**, 2218–2223.
213 Y. Wang, L. Cao, N. J. Libretto, X. Li, C. Li, Y. Wan, C. He, J. Lee, J. Gregg, H. Zong, D. Su, J. T. Miller, T. Mueller and C. Wang, *J. Am. Chem. Soc.*, 2019, **141**, 16635–16642.
214 N. Zhang, X. Zhang, Y. Kang, C. Ye, R. Jin, H. Yan, R. Lin, J. Yang, Q. Xu, Y. Wang, Q. Zhang, L. Gu, L. Liu, W. Song, J. Liu, D. Wang and Y. Li, *Angew. Chem., Int. Ed.*, 2021, **60**, 13388–13393.
215 Y. Li, C. Chen, R. Cao, Z. Pan, H. He and K. Zhou, *Appl. Catal., B*, 2020, **268**, 118747.
216 J. Jiao, R. Lin, S. Liu, W.-C. Cheong, C. Zhang, Z. Chen, Y. Pan, J. Tang, K. Wu, S.-F. Hung, H. M. Chen, L. Zheng, Q. Lu, X. Yang, B. Xu, H. Xiao, J. Li, D. Wang, Q. Peng, C. Chen and Y. Li, *Nat. Chem.*, 2019, **11**, 222–228.
217 Y. Wang, B. J. Park, V. K. Paidi, R. Huang, Y. Lee, K.-J. Noh, K.-S. Lee and J. W. Han, *ACS Energy Lett.*, 2022, **7**, 640–649.
218 T. Ding, X. Liu, Z. Tao, T. Liu, T. Chen, W. Zhang, X. Shen, D. Liu, S. Wang, B. Pang, D. Wu, L. Cao, L. Wang, T. Liu, Y. Li, H. Sheng, M. Zhu and T. Yao, *J. Am. Chem. Soc.*, 2021, **143**, 11317–11324.
219 A. S. Varela, N. Ranjbar Sahraie, J. Steinberg, W. Ju, H.-S. Oh and P. Strasser, *Angew. Chem., Int. Ed.*, 2015, **54**, 10758–10762.
220 Y. Li, B. Wei, M. Zhu, J. Chen, Q. Jiang, B. Yang, Y. Hou, L. Lei, Z. Li, R. Zhang and Y. Lu, *Adv. Mater.*, 2021, **33**, 2102212.
221 L. Jiao, J. Zhu, Y. Zhang, W. Yang, S. Zhou, A. Li, C. Xie, X. Zheng, W. Zhou, S.-H. Yu and H.-L. Jiang, *J. Am. Chem. Soc.*, 2021, **143**, 19417–19424.
222 Z. Pei, H. Zhang, Z.-P. Wu, X. Feng Lu, D. Luan and X. W. D. Lou, *Sci. Adv.*, 2023, **9**, eadh1320.
223 T. Tang, Z. Wang and J. Guan, *Adv. Funct. Mater.*, 2022, **32**, 2111504.
224 L. Lin, H. Li, C. Yan, H. Li, R. Si, M. Li, J. Xiao, G. Wang and X. Bao, *Adv. Mater.*, 2019, **31**, 1903470.
225 D. Yao, C. Tang, X. Zhi, B. Johannessen, A. Slattery, S. Chern and S. Z. Qiao, *Adv. Mater.*, 2023, **35**, 2209386.
226 H. Shang, T. Wang, J. Pei, Z. Jiang, D. Zhou, Y. Wang, H. Li, J. Dong, Z. Zhuang, W. Chen, D. Wang, J. Zhang and Y. Li, *Angew. Chem., Int. Ed.*, 2020, **59**, 22465–22469.
227 X. Zu, X. Li, W. Liu, Y. Sun, J. Xu, T. Yao, W. Yan, S. Gao, C. Wang, S. Wei and Y. Xie, *Adv. Mater.*, 2019, **31**, 1808135.
228 P. Huang, M. Cheng, H. Zhang, M. Zuo, C. Xiao and Y. Xie, *Nano Energy*, 2019, **61**, 428–434.
229 S. Chen, B. Wang, J. Zhu, L. Wang, H. Ou, Z. Zhang, X. Liang, L. Zheng, L. Zhou, Y.-Q. Su, D. Wang and Y. Li, *Nano Lett.*, 2021, **21**, 7325–7331.
230 Y. Wang, Z. Chen, P. Han, Y. Du, Z. Gu, X. Xu and G. Zheng, *ACS Catal.*, 2018, **8**, 7113–7119.
231 J.-C. Jiang, J.-C. Chen, M.-D. Zhao, Q. Yu, Y.-G. Wang and J. Li, *Nano Res.*, 2022, **15**, 7116–7123.
232 T. Zheng, C. Liu, C. Guo, M. Zhang, X. Li, Q. Jiang, W. Xue, H. Li, A. Li, C.-W. Pao, J. Xiao, C. Xia and J. Zeng, *Nat. Nanotechnol.*, 2021, **16**, 1386–1393.
233 H. Shen, T. Wang, H. Jiang, P. Zhao, Z. Chen, Y. Feng, Y. Cao, Y. Guo, Q. Zhang and H. Zhang, *Appl. Catal., B*, 2023, **339**, 123140.
234 D. Wang, R. Cao, S. Hao, C. Liang, G. Chen, P. Chen, Y. Li and X. Zou, *Green Energy Environ.*, 2023, **8**, 820–830.
235 W. Wu, J. Zhu, Y. Tong, S. Xiang and P. Chen, *Nano Res.*, 2024, **17**, 3684–3692.
236 M. G. Kim, J. Park, Y. Choi, H. C. Song, S. H. Kim, K. M. Bang, H. C. Ham, N. K. Kim, D. H. Won, B. K. Min, S. J. Yoo and W. Kim, *Adv. Energy Mater.*, 2023, **13**, 2300749.
237 V. Okatenko, A. Loiudice, M. A. Newton, D. C. Stoian, A. Blokhina, A. N. Chen, K. Rossi and R. Buonsanti, *J. Am. Chem. Soc.*, 2023, **145**, 5370–5383.
238 Y. Chen, N. Lyu, J. Zhang, S. Yan, C. Peng, C. Yang, X. Lv, C. Hu, M. Kuang and G. Zheng, *Small*, 2023, 2308004, DOI: **10.1002/smll.202308004**.
239 L. Xiao, Z. Wang and J. Guan, *Chem. Sci.*, 2023, **14**, 12850–12868.
240 S. Nellaiappan, N. K. Katiyar, R. Kumar, A. Parui, K. D. Malviya, K. G. Pradeep, A. K. Singh, S. Sharma, C. S. Tiwary and K. Biswas, *ACS Catal.*, 2020, **10**, 3658–3663.
241 J. Cavin, A. Ahmadiparidari, L. Majidi, A. S. Thind, S. N. Misal, A. Prajapati, Z. Hemmat, S. Rastegar, A. Beukelman, M. R. Singh, K. A. Unocic, A. Salehi-Khojin and R. Mishra, *Adv. Mater.*, 2021, **33**, 2100347.
242 D. Roy, S. C. Mandal and B. Pathak, *J. Phys. Chem. Lett.*, 2022, **13**, 5991–6002.
243 H. Tian, T. Wang, F. Zhang, S. Zhao, S. Wan, F. He and G. Wang, *J. Mater. Chem. A*, 2018, **6**, 12816–12841.
244 Z. Zhang, Z. P. Cano, D. Luo, H. Dou, A. Yu and Z. Chen, *J. Mater. Chem. A*, 2019, **7**, 20985–21003.
245 M. K. Aslam, K. Yang, S. Chen, Q. Li and J. Duan, *EES Catal.*, 2023, **1**, 179–229.
246 D. Yang and B. C. Gates, *ACS Catal.*, 2019, **9**, 1779–1798.
247 J. Li, H. Luo, B. Li, J.-G. Ma and P. Cheng, *Mater. Chem. Front.*, 2023, **7**, 6107–6129.
248 Z. Li, M. Song, W. Zhu, W. Zhuang, X. Du and L. Tian, *Coord. Chem. Rev.*, 2021, **439**, 213946.
249 T. A. Al-Attas, N. N. Marei, X. Yong, N. G. Yasri, V. Thangadurai, G. Shimizu, S. Siahrostami and M. G. Kibria, *ACS Catal.*, 2021, **11**, 7350–7357.
250 Y. Guo, H. Yang, X. Zhou, K. Liu, C. Zhang, Z. Zhou, C. Wang and W. Lin, *J. Mater. Chem. A*, 2017, **5**, 24867–24873.

251 Y. Ye, F. Cai, H. Li, H. Wu, G. Wang, Y. Li, S. Miao, S. Xie, R. Si, J. Wang and X. Bao, *Nano Energy*, 2017, **38**, 281–289.
252 C. Hu, S. Bai, L. Gao, S. Liang, J. Yang, S.-D. Cheng, S.-B. Mi and J. Qiu, *ACS Catal.*, 2019, **9**, 11579–11588.
253 C. W. Lee, K. D. Yang, D. H. Nam, J. H. Jang, N. H. Cho, S. W. Im and K. T. Nam, *Adv. Mater.*, 2018, **30**, 1704717.
254 J. Wang, Y. Chen, S. Zhang, C. Yang, J. Y. Zhang, Y. Su, G. Zheng and X. Fang, *Small*, 2022, **18**, 2202238.
255 W. Xiong, D. Si, J. Yi, Y. Huang, H. Li and R. Cao, *Appl. Catal., B*, 2022, **314**, 121498.
256 Y. J. Jang, J. Lee, J. H. Kim, B. J. Lee and J. S. Lee, *J. Power Sources*, 2018, **378**, 412–417.
257 X. Ma, J. Tian, M. Wang, X. Jin, M. Shen and L. Zhang, *Catal. Sci. Technol.*, 2021, **11**, 6096–6102.
258 C. Liu, X.-D. Zhang, J.-M. Huang, M.-X. Guan, M. Xu and Z.-Y. Gu, *ACS Catal.*, 2022, **12**, 15230–15240.
259 L. Li, Z. Jiang, Y. Li, F. Li, Y. Pan, X. Zhang, Y. Liang and Z. Zheng, *Small Methods*, 2022, **7**, 2201213.
260 Q.-H. Zheng, C. Chen, S.-M. Cao, M.-T. Peng, B.-X. Dong and Y.-L. Teng, *Chin. Chem. Lett.*, 2023, **34**, 107273.
261 I. Hod, M. D. Sampson, P. Deria, C. P. Kubiak, O. K. Farha and J. T. Hupp, *ACS Catal.*, 2015, **5**, 6302–6309.
262 C.-W. Kung, C. O. Audu, A. W. Peters, H. Noh, O. K. Farha and J. T. Hupp, *ACS Energy Lett.*, 2017, **2**, 2394–2401.
263 P. C. Adrien, A. I. Benin, N. W. Ockwig, M. O'Keeffe, A. J. Matzger and O. M. Yaghi, *Science*, 2005, **310**, 1166–1170.
264 L. Xiao, Z. Wang and J. Guan, *Adv. Funct. Mater.*, 2024, **34**, 2310195.
265 H.-J. Zhu, M. Lu, Y.-R. Wang, S.-J. Yao, M. Zhang, Y.-H. Kan, J. Liu, Y. Chen, S.-L. Li and Y.-Q. Lan, *Nat. Commun.*, 2020, **11**, 497.
266 Y. Yue, P. Cai, K. Xu, H. Li, H. Chen, H.-C. Zhou and N. Huang, *J. Am. Chem. Soc.*, 2021, **143**, 18052–18060.
267 X.-F. Qiu, J.-R. Huang, C. Yu, Z.-H. Zhao, H.-L. Zhu, Z. Ke, P.-Q. Liao and X.-M. Chen, *Angew. Chem., Int. Ed.*, 2022, **61**, e202206470.
268 A. Schneemann, R. Dong, F. Schwotzer, H. Zhong, I. Senkovska, X. Feng and S. Kaskel, *Chem. Sci.*, 2021, **12**, 1600–1619.
269 M. Liu, S. Liu, Q. Xu, Q. Miao, S. Yang, S. Hanson, G. Z. Chen, J. He, Z. Jiang and G. Zeng, *Carbon Energy*, 2023, **5**, 1–12.
270 S. B. Alahakoon, K. Tan, H. Pandey, S. D. Diwakara, G. T. McCandless, D. I. Grinffiel, A. Durand-Silva, T. Thonhauser and R. A. Smaldone, *J. Am. Chem. Soc.*, 2020, **142**, 12987–12994.
271 M. Li, B. Han, S. Li, Q. Zhang, E. Zhang, L. Gong, D. Qi, K. Wang and J. Jiang, *Small*, 2024, 2310147, DOI: **10.1002/smll.202310147**.
272 Q. Wu, R.-K. Xie, M.-J. Mao, G.-L. Chai, J.-D. Yi, S.-S. Zhao, Y.-B. Huang and R. Cao, *ACS Energy Lett.*, 2020, **5**, 1005–1012.
273 R. Matheu, E. Gutierrez-Puebla, M. A. Monge, C. S. Diercks, J. Kang, M. S. Prévot, X. K. Pei, N. Hanikel, B. Zhang, P. D. Yang and O. M. Yaghi, *J. Am. Chem. Soc.*, 2019, **141**, 17081–17085.
274 B. Han, Y. Jin, B. Chen, W. Zhou, B. Yu, C. Wei, H. Wang, K. Wang, Y. Chen, B. Chen and J. Jiang, *Angew. Chem., Int. Ed.*, 2022, **61**, e202114244.
275 S.-Y. Chi, Q. Chen, S.-S. Zhao, D.-H. Si, Q.-J. Wu, Y.-B. Huang and R. Cao, *J. Mater. Chem. A*, 2022, **10**, 4653–4659.
276 H. Shin, K. U. Hansen and F. Jiao, *Nat. Sustain.*, 2021, **4**, 911–919.
277 W. Lai, Y. Qiao, J. Zhang, Z. Lin and H. Huang, *Energy Environ. Sci.*, 2022, **15**, 3603–3629.
278 I. E. L. Stephens, K. Chan, A. Bagger, S. W. Boettcher, J. Bonin, E. Boutin, A. K. Buckley, R. Buonsanti, E. R. Cave, X. Chang, S. W. Chee, A. H. M. da Silva, P. de Luna, O. Einsle, B. Endrődi, M. Escudero-Escribano, J. V. Ferreira de Araujo, M. C. Figueiredo, C. Hahn, K. U. Hansen, S. Haussener, S. Hunegnaw, Z. Huo, Y. J. Hwang, C. Janáky, B. S. Jayathilake, F. Jiao, Z. P. Jovanov, P. Karimi, M. T. M. Koper, K. P. Kuhl, W. H. Lee, Z. Liang, X. Liu, S. Ma, M. Ma, H.-S. Oh, M. Robert, B. R. Cuenya, J. Rossmeisl, C. Roy, M. P. Ryan, E. H. Sargent, P. Sebastián-Pascual, B. Seger, L. Steier, P. Strasser, A. S. Varela, R. E. Vos, X. Wang, B. Xu, H. Yadegari and Y. Zhou, *JPhys Energy*, 2022, **4**, 042003.
279 C. Ampelli, F. Tavella, D. Giusi, A. M. Ronsisvalle, S. Perathoner and G. Centi, *Catal. Today*, 2023, **421**, 114217.
280 N. Fujinuma, A. Ikoma and S. E. Lofland, *Adv. Energy Mater.*, 2020, **10**, 2001645.
281 S. Liang, N. Altaf, L. Huang, Y. Gao and Q. Wang, *J. CO_2 Util.*, 2020, **35**, 90–105.
282 Q. Chen, X. Wang, Y. Zhou, Y. Tan, H. Li, J. Fu and M. Liu, *Adv. Mater.*, 2023, **36**, 2303902.
283 D. A. Salvatore, C. M. Gabardo, A. Reyes, C. P. O'Brien, S. Holdcroft, P. Pintauro, B. Bahar, M. Hickner, C. Bae, D. Sinton, E. H. Sargent and C. P. Berlinguette, *Nat. Energy*, 2021, **6**, 339–348.
284 D. Gao, P. Wei, H. Li, L. Lin, G. Wang and X. Bao, *Acta Phys.–Chim. Sin.*, 2020, 2009021.
285 Y. Meng, H. Huang, Y. Zhang, Y. Cao, H. Lu and X. Li, *Front. Chem.*, 2023, **11**, 1172146.
286 H. Cao, Z. Zhang, J.-W. Chen and Y.-G. Wang, *ACS Catal.*, 2022, **12**, 6606–6617.